RADIATION-INDUCED EFFECTS IN CHALCOGENIDE-BASED MEMORY DEVICES AND FILMS

by

Kasandra Wolf

A thesis

submitted in partial fulfillment

of the requirements for the degree of

Master of Science in Electrical Engineering

Boise State University

December 2014

© 2014

Kasandra Wolf

ALL RIGHTS RESERVED

BOISE STATE UNIVERSITY GRADUATE COLLEGE

DEFENSE COMMITTEE AND FINAL READING APPROVALS

of the thesis submitted by

Kasandra Wolf

Thesis Title: Radiation-Induced Effects in Chalcogenide-Based Memory Devices and Films

Date of Final Oral Examination: 10 July 2014

The following individuals read and discussed the thesis submitted by student Kasandra Wolf, and they evaluated her presentation and response to questions during the final oral examination. They found that the student passed the final oral examination.

Maria I. Mitkova, Ph.D.	Chair, Supervisory Committee
William B. Knowlton, Ph.D.	Member, Supervisory Committee
Dmitri Tenne, Ph.D	Member, Supervisory Committee

The final reading approval of the thesis was granted by Maria I. Mitkova, Ph.D., Chair of the Supervisory Committee. The thesis was approved for the Graduate College by John R. Pelton, Ph.D., Dean of the Graduate College.

DEDICATION

To Kristina, Edward, Kathaleya, and Michael

ACKNOWLEDGEMENTS

I would like to express my sincere gratitude to my advisor Dr. Maria Mitkova for her continued encouragement, guidance, and enthusiasm throughout my collegiate career. I am grateful for the opportunities provided to me by her as well as the advice she imparted to me. Working for and learning from her was a true pleasure.

I would like to thank my committee members Dr. Bill Knowlton and Dr. Dmitri Tenne for advising and sharing their knowledge with me. I am thankful to Dr. Tenne in particular for his patience and helping me learn about Raman spectroscopy. Also, I would like to express my gratitude to Dr. Michael Kozicki and Dr. Hugh Barnaby who were co-Primary Investigators on the project for providing valuable discussions regarding the experimental procedures and assisting in the interpretation of results.

Additionally, I'm thankful to Pete Miranda, the Director of Idaho Microfabrication Laboratory, for training me on the equipment and his assistance in obtaining quality results. I would like to acknowledge Dr. Karthik Chinnathambi for assisting with measurements on the XRD.

I am thankful to the members of the Nano-Ionic Materials and Devices Research Group, Dr. Rizwan Latif, Dr. Mahesh Ailavajhala, Dr. Ping Chen, Dr. Diana Neshava, Dr. Yoshifumi Sakaguchi, Tyler Nichol, Brian Dambi, and Bhes Pun. I also thank the students of Dr. Tenne's Research group, Dan Hillsberry, Andy Farrar, and Jeff Romero, for assisting in troubleshooting of the Raman system. Thanks are also due to my

collaborators at Arizona State University, Dr. Yago Gonzalez-Velo, Jennifer Taggart, and Herbert Bowler.

A special thank you goes to the sources of financial support: the Department of Defense – Defense Threat Reduction Agency (DOD-DTRA) and the Department of Energy-Nuclear Engineering in University Program (DOE-NEUP). Thank you to the faculty and staff of the Boise State University Department of Electrical and Computer Engineering and Donna Welch for everything they have done to help me.

Finally, I am grateful to my family and friends for their love and continued support. Thank you to my mom and dad for providing unwavering support as I pursued my collegiate studies. Thank you to my sister and brother for their love and encouragement.

ABSTRACT

Continued scaling of memory devices has produced many issues for the current foremost non-volatile memory—the flash memory—leading to the emergence of a wide variety of alternative memory solutions. Redox Conductive Bridge Memory (RCBM) is one such solution that has shown great promise in recent years. However, the performance of these devices under radiation conditions has not been explored in detail. This work investigates the effects of x-rays and electron bombardment on chalcogenide glasses and RCBM devices based on these materials.

RCBM devices are a form of Resistance Change Memory, which rely on two distinct resistive states to represent the binary ‘0’ and ‘1’ memory conditions. The functionality of the RCBM devices is based on the growth and dissolution of a conductive filament through an insulating medium sandwiched between two metal electrodes. The presence of the filament represents the on state, while the absence represents the off state.

In this work, we studied RCBM devices fabricated utilizing amorphous Ge-Se films as the active medium. Various compositions of Ge-Se films were studied in order to fully understand the effect of radiation over their properties and determine the most stable system. Various compositions of Ge-Se films in contact with an Ag source were studied as well to simulate the exact processes occurring in the RCBM devices under radiation. Several different material characterization methods were utilized in order to perceive all

of the effects occurring in the systems comprising the RCBM devices. The major characterization methods include Energy Dispersive Spectroscopy to determine the exact compositions, Raman spectroscopy for analyzing the structural properties, and x-ray diffraction to identify the molecular compounds. Both electron beam radiation and x-ray radiation were found to affect the variety of chalcogenide glass compositions and structures containing Ag in different manners, with each radiation type having a specific impact signature. Correspondingly, radiation exposure also affected the performance parameters of the RCBM devices. The performances of these devices under the influence of both forms of radiation were strongly related to the composition of the film within the device.

TABLE OF CONTENTS

LIST OF TABLES

LIST OF FIGURES

LIST OF ABBREVIATIONS

ChG	Chalcogenide Glasses
RCM	Resistance Change Memory
RCBM	Redox Conductive Bridge Memory
MIM	Metal Insulator Metal
LRS	Low Resistive State/On-State Resistance
HRS	High Resistive State/Off-State Resistance
SEM	Scanning Electron Microscope
XRD	X-ray Diffraction
EDS	Energy Dispersive Spectroscopy
BOE	Buffered Oxide Etch
e-beam	electron beam

CHAPTER 1: IONIZING RADIATION

The increased need for scaling of memory devices has led to the emergence of alternative memory solutions. In many circumstances, these memory devices may be required to perform in extreme environmental conditions, for which performance data has not been disseminated. An example of such a circumstance is the application of these devices in space exploration. This work investigates the influence of radiation by x-rays and electron beam on the Redox Conductive Bridge Memory (RCBM) devices.

Forms of Ionizing Radiation

There are many types of radiation, of which there are two primary categories: ionizing and nonionizing radiation. Ionizing radiation is classified as any form of radiation energy composed of photons or particles with enough kinetic energy to remove an electron from the valence band of an atom. The energy typically required to remove an electron from an atom is 4-25 eV [1].

There are two different forms of ionizing radiation: directly ionizing radiation and indirectly ionizing radiation. Directly ionizing radiation is composed of charged particles that ionize the atoms by directly interacting with the atoms [1]. Forms of directly ionizing radiation include the following: electrons, positrons, ions, α-particles, and β-particles. In order to ionize the atom, each of these particles must have high enough kinetic energy (i.e., high velocity) to excite an electron in the valence band of the atom. Indirectly ionizing radiation, on the other hand, is composed of uncharged particles, like photons or

neutrons, which transfer their energy to charged particles in the material upon which it is incident. The photoelectric effect occurs when an incident photon interacts with an electron and transfers all of its energy to the electron. If the photon transfers sufficient energy to the electron to release the electron from the bonding site, then this interaction results in the ionization of the atom. Depending on the amount of energy transferred, the excited electron can interact with other atoms and excite another electron deeper within the material.

Certain types of electromagnetic radiation are classified as indirectly ionizing radiation, including γ-rays, x-rays, ultraviolet light, and visible light for some materials. An ionizing photon with energy of 4 eV would have a corresponding wavelength of 300 nm. Conversion between the photon frequency and the photon energy was theorized by Max Plank [2]. This relationship between the energy (E) of the particle and the wavelength (λ) is described by the following equations, in which *h* is Planck's constant (4.136×10^{15} eV·s), *c* is the speed of light (2.998×10^{8} m/s), and f is the frequency of the electromagnetic wave.

$$E = hf \tag{1}$$

$$\lambda = \frac{c}{f} \tag{2}$$

$$E = \frac{hc}{\lambda} \tag{3}$$

Generation of X-Rays

X-rays are a form of electromagnetic radiation with photon energies ranging from 100 eV to 100 keV with wavelengths ranging from 10 pm to 10 nm. X-rays can be

generated using three different methods: the Bremsstrahlung process, shell emission, or synchrotron radiation.

The Bremsstrahlung x-rays are generated when an electron passes through the electric field of a nucleus, causing the velocity of the electron to decrease. Due to the law of conservation of energy, the difference in energy from the electron entering and exiting the electric field is present in the form of a photon [3, 4]. This process is also known as the inverse photoelectric effect because kinetic energy from a moving electron is converted to an electromagnetic wave [3]. The wavelength of the resulting photon is described by the following equation, in which E_i is the energy of the electron as it is entering the electric field and E_f is the energy as it exits.

$$\lambda = \frac{hc}{E_i - E_f} \tag{4}$$

Bremsstrahlung x-rays are produced using an apparatus similar to the diagram shown in Figure 1. Current passes through the heated filament (cathode) and emits electrons through thermionic emission [3, 5]. The beam of electrons is accelerated using a strong electric field and then focused onto the cathode. The potential difference between the cathode and anode is typically on the order of 35 kV [3]. The positively charged anode attracts the generated electrons from the cathode and the electrons are directed towards a heavy metal target (typically made of tungsten) [3, 5]. The velocities of the electrons significantly decrease when they collide with the tungsten target and therefore they emit x-rays. The cathode and anode are contained inside an evacuated envelope or tube in order to avoid scattering of the electrons by air [3]. Additionally, the envelope must be transparent to x-rays in order to emit the x-rays towards the target situated outside of the envelope.

The Bremsstrahlung process produces x-rays in a wide spectrum of wavelengths; for this reason, Bremsstrahlung x-rays are also called an x-ray continuum, depicted in Figure 2. A single crystal target will produce a monochromatic and strongly collimated x-ray beam. However, by using a higher exciting potential, the relative range of wavelengths can be highly minimized at the expense of having a broad tail in the spectrum. The effect of the tail can be significantly diminished by placing filters on the outside of the envelope.

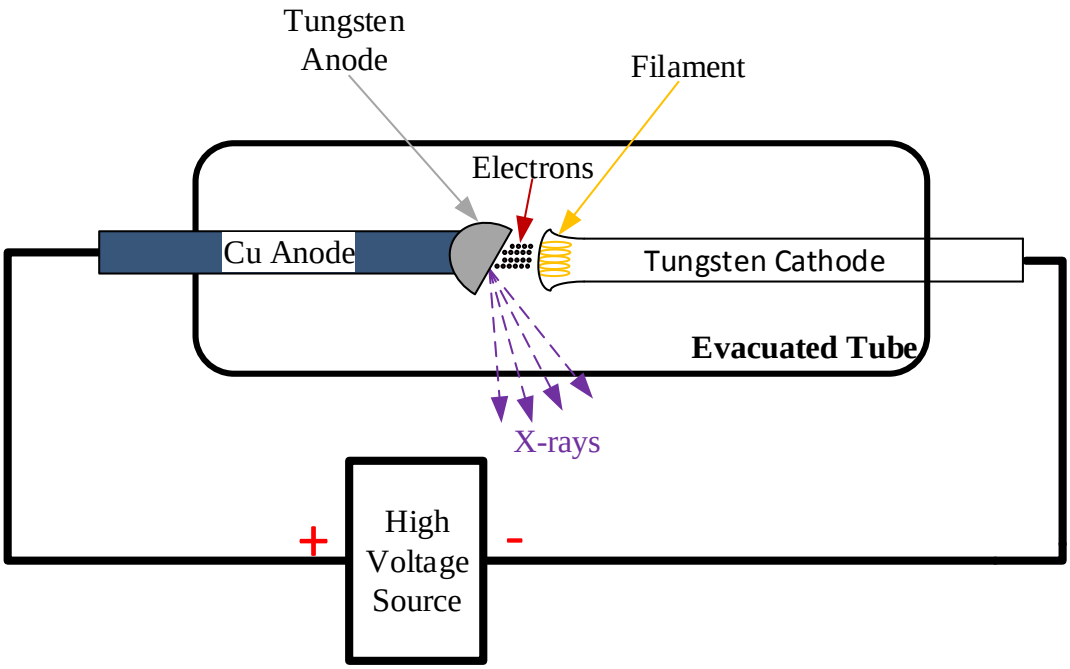

Figure 1. **Schematic diagram representing the x-ray tube where x-rays are produced by the Bremsstrahlung process**

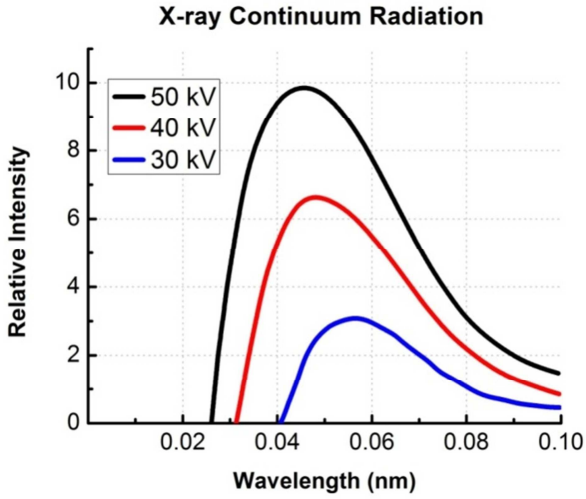

Figure 2. Spectra of Bremsstrahlung x-rays with various electron exciting potential gradients [3]

During the production of Bremsstrahlung x-rays, another event known as shell emission, which also produces x-rays, may occur. According to the Bohr model of an atom, electrons occupy orbits, or shells, at discrete distances from the nucleus. During shell emission, x-rays are generated when electrons in a higher energy shell transition to a lower energy shell [5]. The transition produces a photon with an energy equivalent to the difference in that of the shells [5]. The most common form of this event is K_α shell emission, in which electrons transition into the innermost and lowest energy K shell from the adjacent L shell. X-rays produced from shell emission are known as characteristic x-rays since they have energies characterized by the atomic energy levels. Characteristic x-rays are denominated by the shell in which the electrons land in and a Greek letter (α, β, γ, δ, etc.) that signifies the difference in the energy levels before and after the transition. For example, electrons that transition from the n=2 energy level to the n=1 energy level emit K_α x-rays, while electrons that transition from the n=3 energy level to the n=1 energy level emit K_β x-rays.

The apparatus for generating characteristic x-rays is similar to the apparatus for generating Bremsstrahlung x-rays. Electrons are ejected from the filament through thermionic emission and directed towards the anode, which holds the target. In this process, the incident electrons excite electrons from the K shell of the target atoms. Consequently, an electron from an outer shell of this atom transitions to a lower energy to fill the empty K shell; the difference in energy materializes in the form of a photon. The interaction between the incident electrons and the target atoms will produce both Bremsstrahlung x-rays and characteristic x-rays. However, the relative intensities between the K shell emission x-rays and the Bremsstrahlung x-rays will be very large, thus ensuring that the output x-rays are primarily K shell emission x-rays. X-rays produced from the K shell emissions have a much higher intensity, higher wavelength and narrower range of wavelengths than the Bremsstrahlung x-rays [3]. An example of the K shell emission x-ray spectrum produced using a molybdenum target is shown in Figure 3.

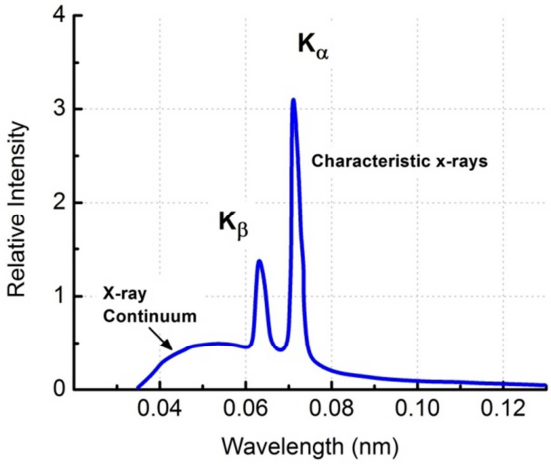

Figure 3. Characteristic x-rays K_α and K_β as produced by K shell emissions from a molybdenum target [3]

A synchrotron source is a more sophisticated and modern method than the Bremsstrahlung tube and K shell emission for producing x-rays. With the aid of a synchrotron source, the most intense x-rays can be manufactured. In this method for x-ray generation, electrons are constantly accelerated radially around a large storage ring, illustrated in Figure 4, maintaining a nearly constant energy. In a modern synchrotron source, electrons are generated with a thermionic gun, and then accelerated using a linear particle accelerator (linac). The energized electrons are injected from the linac into the smaller ring, called the booster ring, as illustrated in Figure 4.

The electrons from the booster ring supply the larger storage ring. Once the synchrotron is in full operation, electrons from the booster ring are periodically injected into the storage ring in order to maintain the specified electron current [6]. Injection of electrons with energies other than the target energy into the storage ring causes strong disturbances in the electrons' orbit and therefore interruptions of the experiments; consequently, the booster ring and storage rings are maintained at the same energies. Additionally, a constant electron current in the storage ring is maintained by frequently injecting electrons from the booster ring that 'top-up' the current when it drops below a small error window of approximately 1 mA [6].

The storage ring is actually a series of straightaways, containing insertion devices, and curves, which contain bending magnets to maintain a closed path. This ring supplies the electrons and/or radiation for any experiment and thus it is a crucial segment of the entire synchrotron operation. To ensure that the electron velocity is maintained throughout the storage ring, a radio frequency (RF) power supply restores energy to the electrons that are lost to synchrotron radiation emission [6]. The electrons lose energy as

they approach the bending magnets and emit synchrotron radiation. This radiation is primarily x-rays generated through the Bremsstrahlung x-ray generation process. The difference between these x-rays and the Bremsstrahlung x-rays is the intensity and the ability to selectively determine the wavelengths, which is a function of the electron velocity and the strength of the bending magnets.

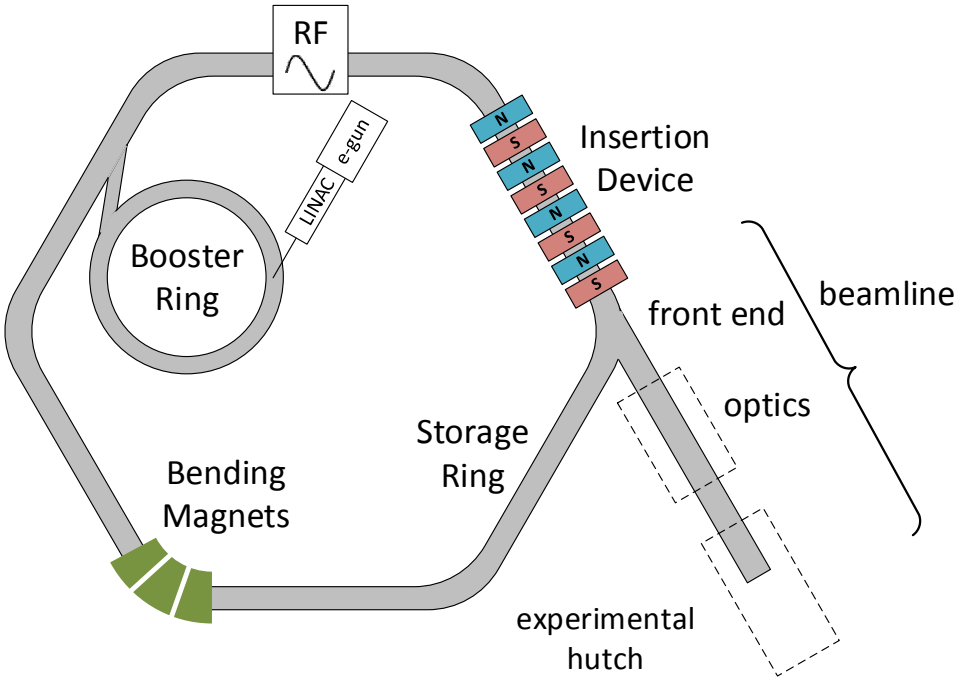

Figure 4. Schematic diagram outlining major components of a modern synchrotron source [6]

Connected to the storage ring are beamlines, which are tangentially connected to the storage ring, situated at each bend of the storage ring. The beamline is composed of three major components: front end, optics, and the experimental hutch. The front end of the beamline serves several functions. It isolates the beamline vacuum from the storage ring vacuum, blocks x-rays, and Bremsstrahlung radiation (when necessary), selects the acceptable angular range radiation, and filters out the synchrotron radiation that is too low in energy [6]. The optics portion of the beamline serves to select the desired energies,

focus the photons, and optimize the energy resolution of the beam [6]. Finally, the synchrotron x-rays reach the experimental hutch where the sample to be irradiated is located.

Formation of Electron Beams

Another type of radiation source is known as an electron beam. Electron beam (e-beam) technology is used in a wide variety of applications, including electron beam welding for industrial purposes, electron beam furnace for refining rare or refractory metals, electron beam lithography for producing semiconductor nanotechnology devices, and Scanning Electron Microscopy (SEM) and Transmission Electron Microscopy (TEM) for imaging microstructures.

The most crucial component for generating an electron beam is the electron gun. Two types of electron beam guns will be described here: thermionic emission and high field emission. The first form, the thermionic emission electron gun, is the most common form of electron gun used in SEM imaging. In the process of thermionic emission, electrons escape the surface of the heated material by acquiring thermal energy. The most deterministic factor in this process is the work function of the heated material, which is the minimum amount of kinetic energy required for electrons to escape from the material. For an electron gun, the ideal work function would be very small in order to minimize the amount of energy required to generate electrons and maximize efficiency of the equipment. Tungsten has a work function of 4.55 eV and is commonly used in electron guns. The maximum current density of the beam can be approximated using the Richardson-Dushman equation, in which T is the Temperature (K), Φ is the work

function (eV), *k* is Boltzmann's constant (8.617 x 10^{-5} eV/K), and A is a material constant with an ideal value of 120 A/cm^2 [6].

$$J = AT^2 e^{-\left(\frac{\phi}{kT}\right)} \tag{5}$$

High field emission is another method for generating electrons, most commonly used in the early forms of electron microscopy. Electrons are generated by the application of a strong electric field between two fine-point electrodes. Electrons escape the surface of the cathode through Fowler-Nordheim tunneling [7]. The current density at the point of the electrode is given by Equation (6), where E is the electric field intensity at the

$$J = 1.54 \times 10^{-6} \frac{E^2}{\phi} e^{-\left(6.83\times10^{7}\frac{\phi^{3/2}}{E}K\right)} \tag{6}$$

emitter, Φ is the work function of the emitting material, and K is a constant approximately equal to 1 [7]. The miniscule surface area of the emitter limits the amount of the electron current produced. The number of emitter sites can be increased and arranged into an array in order to increase the total amount of current produced. However, this type of arrangement may lead to a non-Gaussian distribution in the electron beam.

Interaction of Ionizing Radiation with Matter

Whether the form of ionizing radiation is directly or indirectly ionizing, it will react with solid materials in the same manner: displacement of an electron from the atom. The difference arises in the manner in which the radiation source interacts with the material to create an ionized atom. Directly ionizing radiation and indirectly ionizing radiation interaction with material are described separately due to their unique properties and effects.

Electromagnetic Radiation

As mentioned previously, electromagnetic forms of ionizing radiation are indirectly ionizing because photons are uncharged particles that transfer energy to charged particles in the material. In turn, these newly energized charged particles ionize atoms in the material through Coulombic interactions. Depending on the wavelength, and subsequently the energy, electromagnetic radiation can affect solid materials differently. Most solid materials are transparent to larger wavelength radiation like microwaves, which have wavelengths between 1 mm and 1 meter and corresponding photon energies between 1.24 meV and 1.24 μeV. Thus, radiation with long wavelength (i.e. $\lambda > 10^{-3}$ m) and concurrently low photon energy passes through most solid materials without losing energy or affecting the materials.

Electromagnetic radiation with shorter wavelengths (i.e., ultraviolet, x-ray, γ-ray) have higher energy. In fact, these forms of radiation have enough energy to eject an electron from the valence shell of an atom, ionizing the atom. Therefore, ultraviolet, x-ray, and γ-ray radiation are classified as ionizing radiation. For this reason, only the forms of radiation with high energies are explored in this study. Figure 5 illustrates the various categories of radiation that contribute to the electromagnetic spectrum with their corresponding wavelengths and photon frequencies.

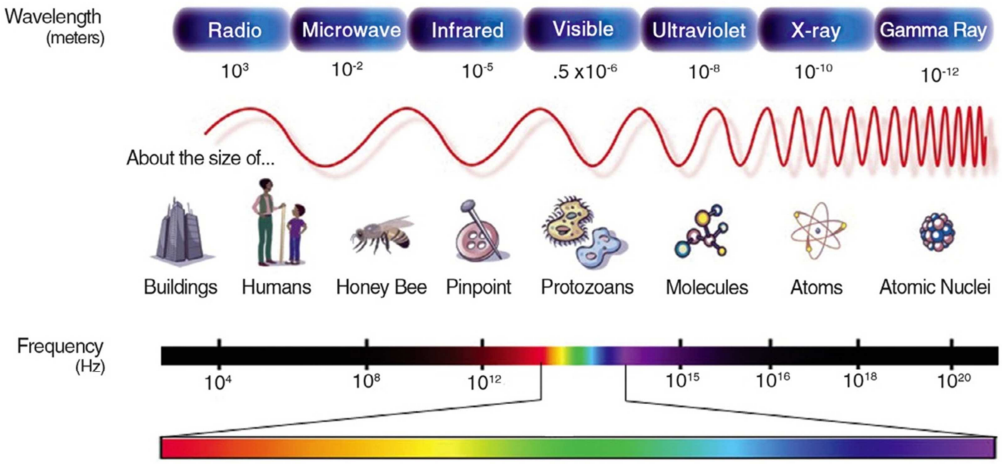

Figure 5. Electromagnetic spectrum describing the wavelengths and corresponding photon frequencies.
Reprinted with permission from [8] © 2012 Elsevier.

When a photon is incident upon an atom, an electron of that atom may absorb all of the photon's energy. If the amount of energy absorbed is greater than the binding energy of the electron, then the electron will have enough energy to escape the atom, effectively ionizing the atom. Most commonly this will occur with an electron from the valence shell. Since this electron was part of a bond with another atom, after excitation from this state, the bond is now broken. The photoelectric effect is the observation of an ejected electron after absorbing all of a photon's energy [3, 5]. The photoelectric effect is most commonly observed with visible light incident on metallic materials, which have low ionization energies [3]; however, it can also be observed in semiconductor materials when higher energy photons are used (e.g., x-rays).

The other type of interaction between photons and materials is known as the Compton Effect. The Compton Effect is prominent when the energy of the incident photon is much larger than the binding energy of the electron. The Compton Effect is an inelastic scattering of a photon incident upon a charged particle, most commonly an electron [3, 5]. In the Compton Effect, only a fraction of the photon's energy is

transferred to a stationary electron, which is then ejected from the location after the interaction with light [5]. The interaction of the photon with the electron results in the formation of an energetic electron and a remnant photon. Due to the law of conservation of energy, the resultant photon energy must equal the difference between the incident photon energy and the kinetic energy of the ejected electron. After the inelastic collision, the resulting photon will have less energy and a longer wavelength. If the resultant photon has enough energy, it may ionize a secondary atom through the photoelectric effect. Otherwise, the remnant photon is absorbed by another electron, exciting the electron to a higher energy level.

Electron Beam Radiation

Electron beam radiation is a form of directly ionizing radiation. Interaction between an electron beam and a solid material can cause a wide range of events, depicted in Figure 6, including the following: generation of backscattered electrons; generation of secondary electrons; electron hole pair recombination; electron transmission; and Bremsstrahlung and characteristic x-ray generation. The energy of the incident electrons will determine which events transpire. In most cases, multiple different forms of events will occur.

A backscattered electron is a consequence of an elastic interaction, meaning no energy is transferred, between a beam electron and the nucleus of the specimen. In this interaction, the electron is scattered back out of the surface of the specimen. The electron is attracted to the nucleus of the atom by the Coulomb force, as described by Equation (7), in which *e* is the elementary charge, Q_2 is the charge of the nucleus, and r is the distance between the two charges.

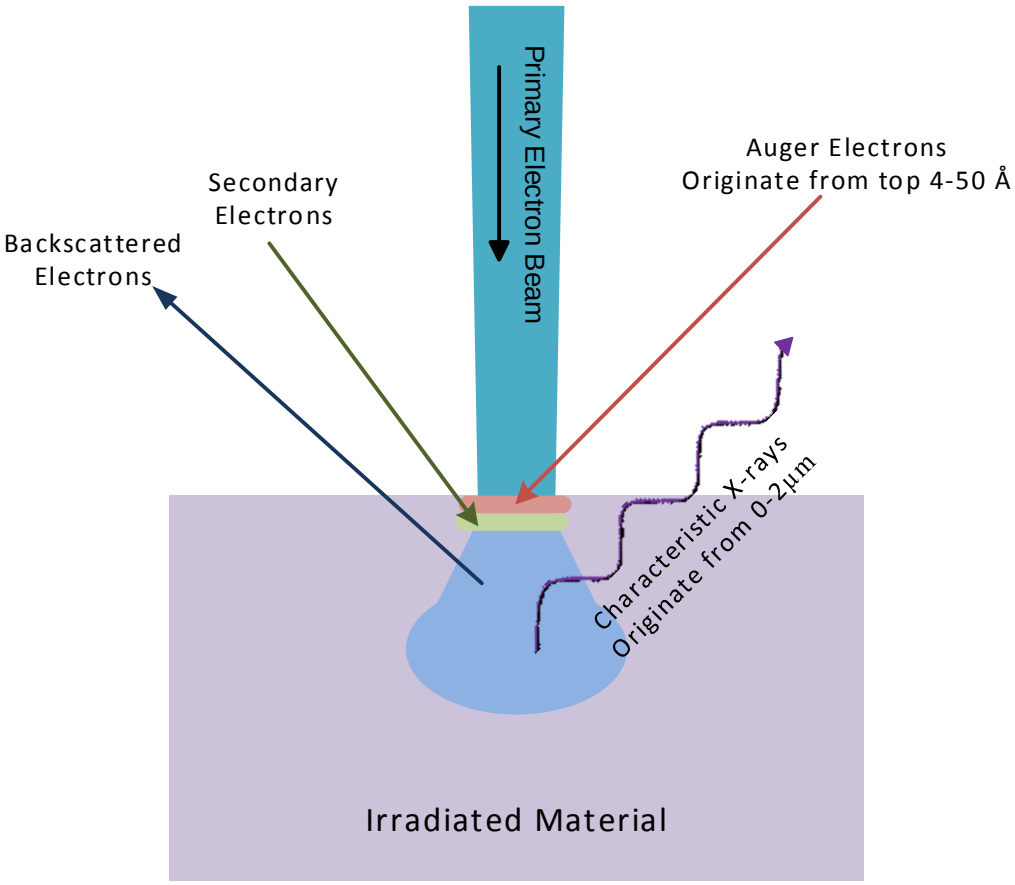

Figure 6. Generalized illustration representing products of electron bombardment; secondary electrons and Auger electrons remain near the surface while backscattered electrons and characteristic x-rays exit the sample

$$\mathbf{F} = \frac{-eQ_2}{4\pi r^2} \tag{7}$$

The equation for Coulomb force reveals that the force is stronger for atoms with higher atomic number Z. Therefore, atoms with higher Z will generate more backscattered electrons than atoms with lower Z, due to the relative number of protons in the nuclei. In scanning electron microscopes, backscattered electrons can be used to detect different compositions, grain boundaries, and phase boundaries.

An inelastic interaction of an electron bounded to an atom with a beam electron or a backscattered electron will result in the formation of a secondary electron [9]. The

incident electron will transfer kinetic energy to the bounded electron, providing enough energy for this electron to escape the valence shell of the atom.

Electron hole pair recombination within the material can result in numerous outcomes including characteristic x-rays, Auger electrons, and cathodoluminescence. Characteristic x-rays, as described previously, emerge when an electron from an outer shell falls into an empty shell closer to the nucleus. The difference in energy between the two shells manifests as an x-ray photon. Auger electrons are formed in a manner similar to characteristic x-rays with the exception that the energy from the electron is transferred to another electron in the outer shell [5, 9]. The excited electron is then ejected from the outer shell. The final product of electron hole pair recombination is cathodoluminescence and occurs in semiconductor materials. An interaction between a beam electron and an electron in the valence band of the semiconductor excite the electron into the conduction band, leaving behind a hole. This energetically unstable state leads to the electron hole pair recombination and the discharge of a photon with the difference in energy [9]. Cathodoluminescence only occurs in semiconductors because the energy bandgap is within the energy range of visible light.

Bremsstrahlung x-rays were previously described in detail. In this case, the Bremsstrahlung x-ray is the photon product of an inelastic interaction of a beam electron or backscattered electron with a nucleus within the specimen. It is also possible for an electron to transmit from the beam source completely through the specimen without interacting with any of the atoms. This is known as electron transmission and is most commonly utilized in Transmission Electron Microscopy (TEM).

This chapter detailed the methods for generating two different forms of ionizing radiation. As previously described, the distinguishing properties of electromagnetic radiation and electron beam radiation influence how each form of radiation will interact with matter. The following chapter will characterize the particular material of interest for this study.

CHAPTER 2: CHALCOGENIDE GLASSES

Chalcogen elements are those that compose Group VIA of the periodic table, most notably, sulfur (S), selenium (Se), and tellurium (Te). Materials that contain these elements are distinguished as chalcogenides. Chalcogenides have a wide range of uses, including applications in solar cells, memory storage, and inorganic photolithography. This chapter will detail chalcogenide glasses, a specific class of these materials, and their unique properties.

Material Classifications

Solid materials take one of three forms: crystalline, polycrystalline, or amorphous. Crystalline materials exhibit long range order where a unit cell is replicated and repeated periodically throughout the entire solid. In these types of materials, once the exact location of an atom and its nearest neighbors are known, the placement of any other atom throughout the crystal can be predicted. Polycrystalline materials are composed of multiple different crystallites or grains varying both in size and orientation. The third type of solid is amorphous material, e.g. fused silica (SiO_2), which exhibit the greatest amount of disorder. Because of the flexibility of their structure, these materials offer versatile applications, one example of which is as an active medium in resistive-change memory devices.

Glass Preparation

Glasses compose a large segment of amorphous materials. The traditional method of glass formation involves melting the materials from pebble or powder form, then cooling the material at a rapid quench rate [10]. The glass synthesis process is summarized in a graph in Figure 7, with further details to follow.

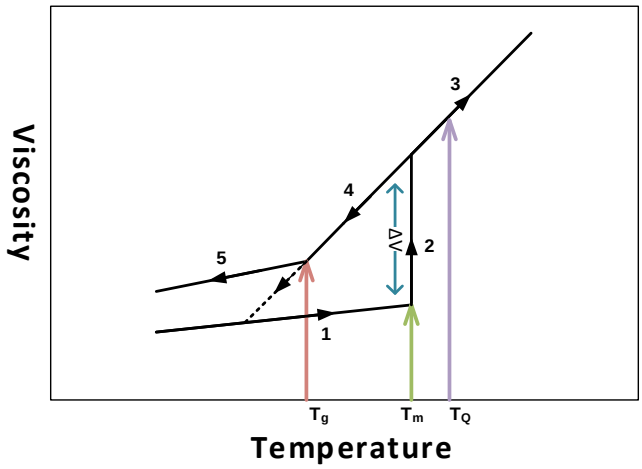

Figure 7. Evolution of material viscosity during glass preparation process Ge-Se Chalcogenide Glasses; the graph shows glass transition temperature (T_g), melting temperature (T_m), and quenching temperature (T_Q)

Initially, the raw materials in pebble form are precisely measured in order to achieve the exact ratio of elements. These materials are vacuum sealed into a fused silica ampoule to avoid oxygen and other contaminants. The sealed ampoule is placed into a specialized rocking furnace, which slowly increases the temperature to the melting temperature (T_m), described as Step 1 in Figure 7. Once the melt reaches T_m, it experiences a dramatic change in viscosity (Step 2). At this point of the synthesis, the furnace, with the ampoule, is rocked to ensure uniform mixture of all elements throughout the melt. Heating and mixing of the melt continues (Step 3) until it reaches a specified quenching temperature (T_Q), at which point it is cooled (Step 4). If the melt is

allowed to cool slowly, indicated by the dotted line in Figure 7, the material structure will transform towards the lowest entropy state, which is crystalline. The temperature at which the glass transitions from a solid to a supercooled liquid is known as the glass transition temperature (T_g). To maintain the amorphous nature of the melt in the solidified material, the ampoule is swiftly removed from the furnace and quenched in air, water, or an ice bath, which forces the material to quickly surpass T_g, preventing crystallization and maintaining a high viscosity (Step 5). Depending on the required quench rate, the quench time can range between milliseconds and hours [11]. Glasses can be created using any system of elements with variable stability, but in different systems there are only certain compositions, known as glass forming regions, in which stable glasses can be formed.

Chalcogenide Glasses

Chalcogenide glasses are covalently bonded glasses that contain at least one of the chalcogen elements. In chalcogenide glasses, the chalcogen elements can be combined with other elements for various applications. For instance, $GeSe_4$ has demonstrated applicability in NO_2 gas sensors [12, 13]; GeSbTe has been used widely in rewritable optical discs as a form of phase-change memory [14]. This study will focus on Ge-Se glasses due to properties that are favorable for resistive-memory devices in harsh radiation environments.

Germanium (Ge) containing chalcogenide glasses are chosen over Arsenic (As) containing chalcogenide glasses primarily for the higher coordination number, which leads to a higher glass transition temperature. Ge is four-fold coordinated while As is

only three-fold coordinated. For example, the transition temperature of $As_{30}S_{70}$ is 100 °C while that of $Ge_{30}S_{70}$ is 400 °C, as determined from the data in Figure 8a and b.

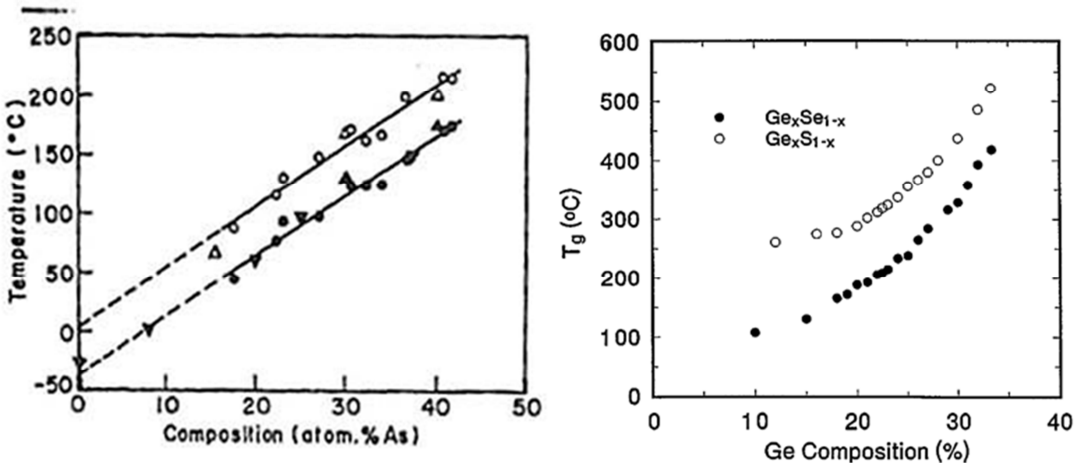

Figure 8. Glass transition temperature for (a) As_xS_{1-x} (b) Ge_xS_{1-x}, and Ge_xSe_{1-x}. (a) Reprinted with permission from [15] © 1966 the Japan Society of Applied Physics (b) Reprinted with permission from [16] © 1997 the American Physical Society

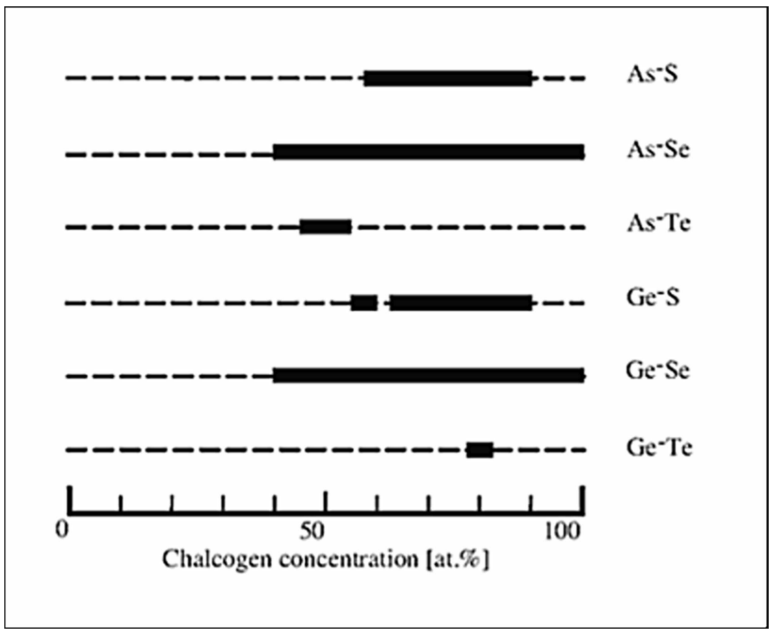

Figure 9. Glass forming regions of binary chalcogenides; Se glasses have the largest glass forming region. Reprinted with permission from [11] © 2011 Springer and Springer eBook

The pairing of the different chalcogen atoms (S, Se, or Te) with germanium, forming the binary Ge-chalcogen glass system, offers distinct properties. Sulfur and selenium containing glasses have similar properties that are ideal for certain types of resistive memory devices. However, selenium containing glasses have some advantages over sulfur containing glasses in radiation environments. Firstly, Ge-Se systems have a larger glass forming region than Ge-S systems, as displayed in Figure 9 [11]. The smaller glass forming region in Ge-S glasses is attributed to the phase separation of sulfur, which easily occurs in sulfur containing glasses. In the case of phase separation, rings of eight sulfur atoms with bond angles of 105° form, which become completely disconnected from the rest of the glass network [17]. Comparatively, selenium containing glasses form hexagonal chains, which run parallel to each other and have bond angles of 103.1° [18]. The bonding forces between the chains are van der Waals forces, which makes these glasses much more flexible; therefore, phase separation is less likely to occur [18]. Additionally, Ge-Se bonds have a longer bonding length (2.135 Å) and smaller bonding energy (485 kJ/mol) than those of Ge-S bonds (2.012 Å, 534 kJ/mol) [19].

The significantly weaker bonds and narrow bandgap common in telluride glasses cause dissimilar electrical and optical performances when compared to the other two chalcogen systems [20, 21]. Additionally, telluride glasses have a small glass forming region, shown in Figure 9, which limits the flexibility to study different compositions offering unique structures that are easily achievable in the other chalcogen systems. Elemental Te cannot form a glass, but Te containing glasses have the lowest T_g of the chalcogenide glasses. For example, in $Ge_{20}Se_{80}$ glass, the Tl_g is 160 °C [22] compared to

the T_g of $Ge_{20}Te_{80}$ at 147 °C [23, 24]. For applications in harsh radiation environments, glasses with higher T_g materials are desirable in order to avoid crystallization.

Structural Units of Ge-Se Glass

Since the structure of the disordered materials is of major importance for their performance and is studied in detail in this work, the fundamentals of the structure of the Ge-Se glasses are presented here. They consist of a basic unit cell: a $GeSe_4$ tetrahedron, shown in Figure 10. It contains a single Ge atom at the center surrounded by four covalently bonded Se atoms, each at a bond angle of 109.5°.

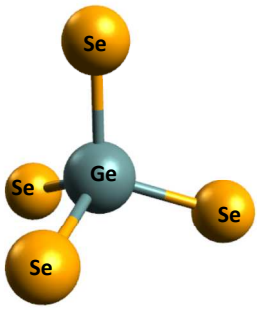

Figure 10. Basic $GeSe_4$ tetrahedron unit; Ge atom at the center of four equidistant Se atoms

The formation of the tetrahedron is due to the sp^3 hybridization of the Ge atom. According to the valence bond theory, the ground state electron configuration of Ge is [Ar] $3d^{10}4s^24p^2$ with the $4s^2$ orbital full and the two $4p^2$ electrons ready to react with their neighbors, as depicted in the left side of Figure 11. However, since the *4s* and *4p* energy levels are quite close, when Ge comes in contact with other atoms, interaction results in the four orbitals $\psi(3s)$, $\psi(3p_x)$, $\psi(3p_y)$, and $\psi(3p_z)$, mixing together to form four new hybrid orbitals. Because the same amount of energy is required to remove each electron from the valence shell of Ge, there cannot be two different energy levels. Thus, the hybrid orbital is formed at energy lower than the 4p orbital and higher than the *4s* orbital.

This orbital is called the sp^3 hybridized orbital because it is formed from one *s* orbital and three *p* orbitals. The sp^3 hybridized orbital is the reason that Ge is typically observed in a tetrahedral structure.

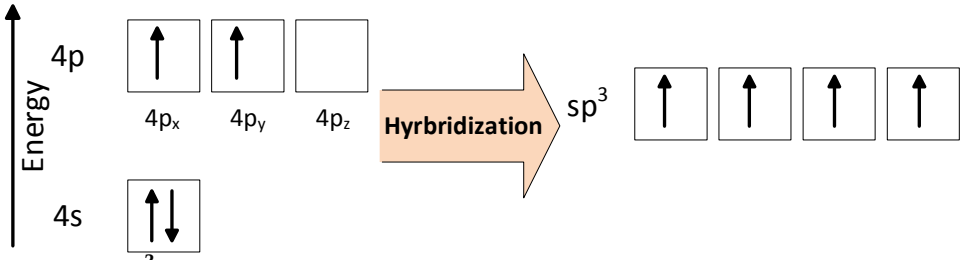

Figure 11. *sp*^{3} hybridization of Ge valence shell; all four electrons have the same energy

Amorphous Ge-chalcogenide materials are composed of several basic structural units: corner-sharing tetrahedral (CS) structures, edge-sharing tetrahedral (ES) structures, ethane-like structures of Ge-Ge bonds (ETH), chalcogen chains (Se-Se or S-S), and distorted rock salt structures [25].

There are two structural units that are each composed of two unit cell tetrahedra: corner-sharing and edge-sharing tetrahedral structures. The corner-sharing tetrahedral structure, shown in Figure 12, consists of two unit cell tetrahedra that share one chalcogen atom, which is situated at the corner of both unit cells. The bonds that the corner Se atom shares with two Ge atoms fill the valence shell of the Se atom and satisfy the 8-N rule [3]. This structure contains a 2:7 ratio of Ge:Se atoms. The edge-sharing tetrahedral structure, shown in Figure 13, consists of two unit cell tetrahedra that share two Se atoms to form an edge in the structure. In the edge-sharing, structure there is a 2:6 ratio of Ge:Se atoms.

The ethane-like bonding structure, shown in Figure 14, consists of two Ge atoms, each Ge atom bonded with three different Se atoms. In this structure, the two Ge atoms

are covalently bonded together, which fills the last sp^3 hybrid orbital to satisfy the 8-N rule. Glasses containing high Ge content (i.e., ≥ 40%) will sometimes contain another structure in which both Ge and Se atoms are three-fold coordinated. This structure only occurs when there are insufficient Se atoms present to satisfy the 8-N requirement of a Ge atom. This Ge atom will form a dative bond with the lone pair electrons of a Se atom, thereby satisfying its valence shell.

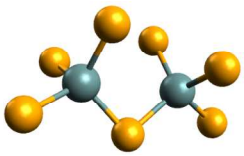

Figure 12. Corner-sharing bond tetrahedral structure

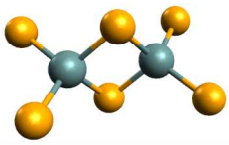

Figure 13. Edge-sharing bond tetrahedral structure

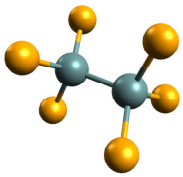

Figure 14. Ethane-like Ge-Ge bonding structure

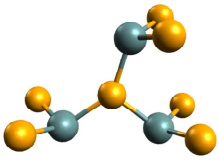

Figure 15. Distorted rock salt layered structure

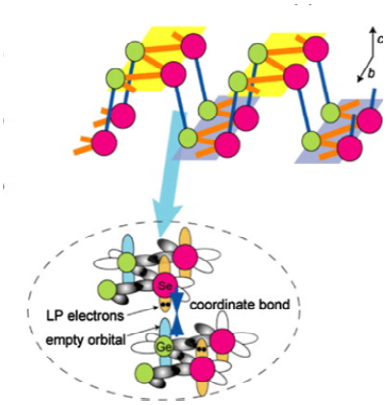

Figure 16. Layered Rock Salt structure [25]

CHAPTER 3: RADIATION-INDUCED EFFECTS IN CHALCOGENIDE GLASSES

The structural units of Ge-Se glasses were described in Chapter 2. The ways in which these structural units are connected together form the backbone of the glass and determine the flexibility of the glass network. This chapter will explore the effect of two different forms of radiation on Ge-Se glasses: electromagnetic and electron beam. As previously mentioned with respect to materials in general, these forms of radiation will interact with chalcogenide glasses in different manners due to the difference in nature of photons and charged particles. Electromagnetic radiation interaction with chalcogenide glasses will be divided into two different groups: (1) sub-bandgap photons and (2) high energy photons.

Electromagnetic Radiation

Absorption Edge

Most materials are transparent to radiation with longer wavelengths (i.e., radio waves and microwaves) and absorb radiation with shorter wavelengths (i.e., x-rays and γ-rays). However, the transparency of a material to radiation with intermediate wavelengths (i.e., visible light and ultraviolet light) is more ambiguous. A material-specific parameter known as the absorption edge identifies the wavelength at which the material becomes transparent to the incident radiation. The absorption spectra for amorphous As-Se and Ge-Se in Figure 17 indicate the absorption edges beginning at 395 nm and 490 nm, respectively. Based on this data, it is approximated that the absorption edge of amorphous

Ge-Se films ranges from 500 nm to 575 nm, which corresponds to photon energies ranging between 2.15 eV and 2.48 eV [26]. Chalcogenide glasses are highly transparent for wavelengths greater than 575 nm and highly applicable for fiber optic applications [27, 28]. Photons with energies greater than 2.48 eV are absorbed and affect the structural performance and properties of the Ge-Se glass, which makes these materials highly applicable for this research.

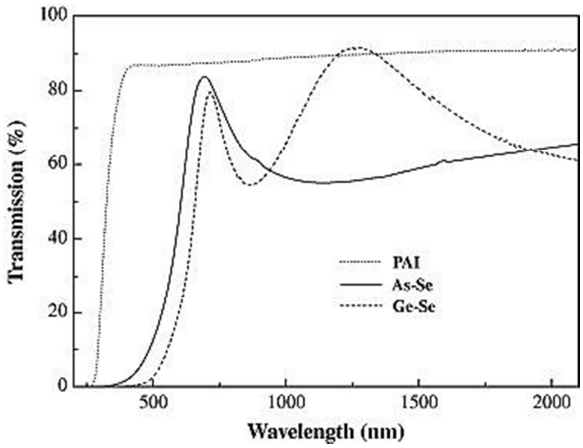

Figure 17. Absorption spectra of amorphous As-Se and Ge-Se; the glasses do not have a straight absorption edge which is centered around 550 nm. Reprinted from with permission from [26] © 2008 Elsevier.

Sub-Bandgap Photons

Two prominent effects have been discovered as resulting from the interaction of visible and ultraviolet light with Ge-Se glasses. These two effects are known as photobleaching, an increase in the transparency, and photodarkening, a decrease in the transparency of the material. Photobleaching of a material corresponds to the absorption edge shifting towards lower wavelengths (i.e., blue shift). Conversely, the absorption edge of a photodarkened material will shift towards higher wavelengths (i.e., red shift). Photobleaching and photodarkening effects in amorphous chalcogenide materials are utilized in a variety of applications, including memory storage, dense holographic

recordings, optomechanical transducers, etc. [29-33]. In some amorphous chalcogenide materials, such as a-GeSe materials, a dual role of both photobleaching and photodarkening was observed [34-36]. However, over longer time periods, photobleaching is more dominant [37].

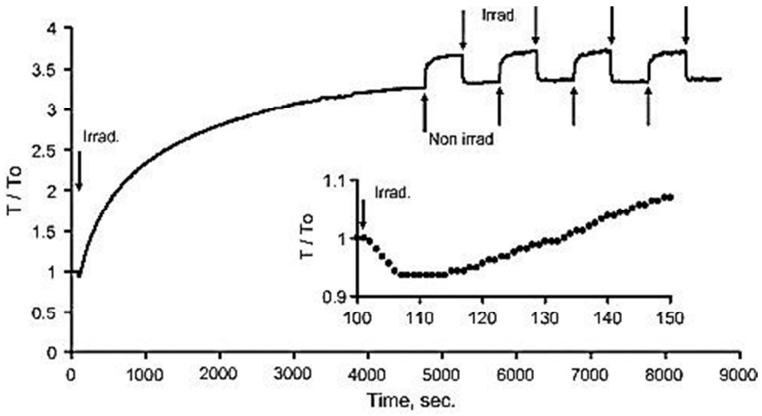

Figure 18. Time evolution of transparency in $GeSe_2$ film with switching light source; photodarkening (decreasing T/To) occurs in initial 110 secs; after 120 secs photobleaching (increasing T/To) starts
Reprinted with permission from [38] © 2011 Elsevier

Studies on Ge-As-chalcogenide glasses have demonstrated the coexistence of both photobleaching and photodarkening, where photodarkening will occur immediately with radiation exposure. After an initial period, photobleaching will become more dominant over photodarkening [35, 36]. The switching from photodarkening to photobleaching is evident in the inset graph of Figure 18. It is hypothesized that this transient photodarkening is due to the formation of intermediate states between the ground state and the photo-excited states energies of electrons [38]. This type of result is attributed to breaking bonds and subsequent molecular rearrangement. The destruction of bonds causes the rearrangement of traps within the bandgap of the material, thus effectively decreasing the bandgap of the material. There are two theories explaining

photodarkening, the first of which states that the broadening of the valence band changes the bandgap [39-45]. The other theory suggests that the extended intermediate states affect the change in the bandgap due to excited charge carriers [39-45]. These two theories are based on the formation of defects, which originate from the breakage of bonds. The specific defects that contribute to photodarkening are located within the bandgap of the material and act as localized states. Increasing the number of defects, the bandgap of the material reduces since there are an abundant number of defect sites in near proximity for an electron to hop from one defect to another.

The other dominating effect is photobleaching of the Ge-chalcogenide glasses, which is also attributed to two different mechanisms. The first mechanism is photo-oxidation of Ge near the surface of the film. Photobleaching due to photo-oxidation has been studied by comparing the transmission spectra of $GeSe_2$ and Ge_2Se_3 films in air and vacuum [37]. The results of this study suggest that in Ge-rich films, 40 at. % Ge, photobleaching is dominated by the photo-oxidation mechanism [37]. In lower Ge-content films, photobleaching is dominated by the second mechanism, changes in the structural ordering [37]. The structural reordering is generalized as a conversion of homopolar bonding structures to heteropolar bonding structures. More specifically, the ethane-like structures, which contain a Ge-Ge bond, and the Se-Se chains reorganize to form structures with Ge-Se bonds (i.e., $GeSe_4$ tetrahedra that can be connected by either a corner or an edge) [36]. The bond conversion is described by chemical reaction in Equation (8) [36].

$$Ge - Ge + Se - Se + h\upsilon \Longrightarrow 2Ge - Se \tag{8}$$

Photodarkening and photobleaching were observed under sub-bandgap light, but similar structural changes and defect formations have also been studied in chalcogenide glasses exposed to high energy photons.

High Energy Photons

Chalcogenide glasses exposed to high energy photons will experience the same effects as when exposed to sub-bandgap photons, in addition to changes associated solely to the high energy photons. The effects of high energy photons can be further categorized as dynamic and static changes in the structural network of the glass. Dynamic changes are those that will decay over a period of time after radiation exposure is stopped (e.g., electron-hole pair generation). In the case of dynamic changes, the structure may revert back to its original state (e.g., electron-hole pair recombination). On the other hand, static changes are those changes that remain after radiation exposure has ceased, such as bond breaking and molecular rearrangement.

Radiation-Induced Dynamic Effects

Electron-hole pair generation is a dynamic effect of photon radiation. In this event, an atom absorbs the energy of a photon. An electron within the atom becomes excited enough to exit the atom, leaving a hole in its place. A study on a-Se systems has demonstrated the dynamic electronic charge neutralization of defects in the network by electrons and holes generated during photon illumination [46]. Initially, the positively charged, over-coordinated Se atoms will trap electrons, while the holes will be trapped around the singly bonded, under-coordinated, and negatively charged Se atoms, effectively neutralizing the electric charge of these atoms [46]. Eventually, the neutralized defects will reach an equilibrium, which allows the charge carriers to move

freely within the network without being trapped [46]. This study also observed that the decreasing amount of defects led to a shift in the Fermi level towards the valence band, which increased the conductivity of the p-type semiconductor [46]. It is believed that the observed effects are due to charge trapping rather than electron-hole pair recombination, because the charged defects revert to their original state after the termination of photon illumination [46].

Radiation-Induced Static Effects

The majority of the changes in the structural network of the glass are primarily related to the radiation-induced static changes. A broken bond resulting from the absorption of a photon forces the surrounding network to rearrange in order to fulfill the 8-N rule for each atom. The details of which particular bond is formed are dependent upon the atoms involved in the broken bond as well as the possible defects situated adjacent to the broken bond. The amorphous nature of the network provides a wide range of possibilities in bond transformations, as illustrated in Figure 17 for the binary As-S system. One possibility, known as destruction-polymerization, is the destruction of a homopolar bond in favor of a heteropolar bond, as illustrated in No. 1-4 in Figure 19, or the destruction of a heteropolar bond in favor of a homopolar bond, No. 9-12. [47].

Additionally, the rearrangement of the network may occur with a broken bond being replaced by the same type of bond. That is, the breaking of one heteropolar bond may result in the formation of a new heteropolar bond involving a different atom, No. 13-16. Analogously, a new homopolar bond may form from a broken homopolar bond, No. 5-8.

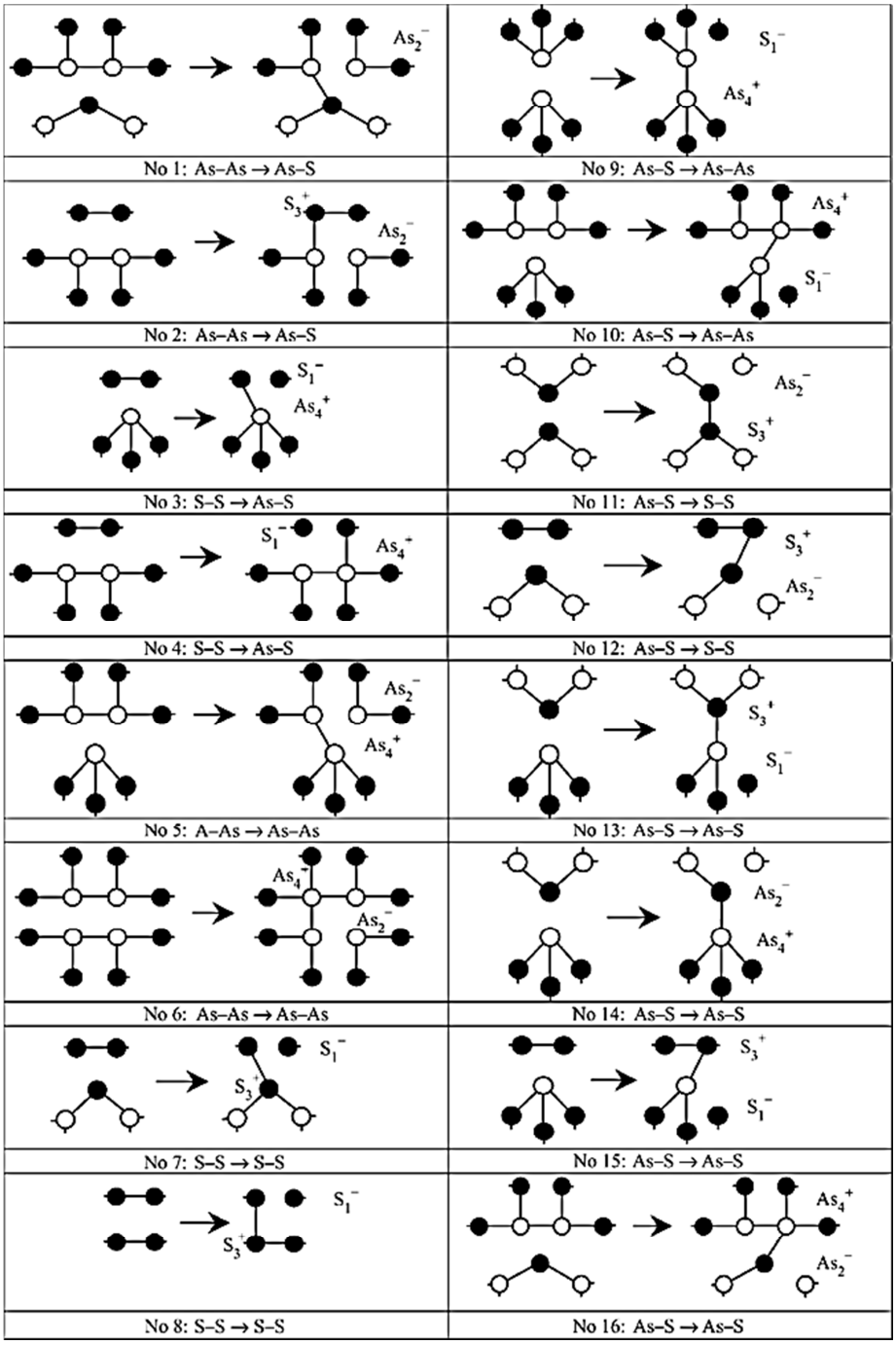

Figure 19. Possible structural changes in a-As_2S_3 with As-○ and S-● Reprinted with permission from [47] © 2004 Elsevier and Elsevier Books

The static structural changes described in Figure 19 are governed by a set of principles that have been defined by Shpotyuk et al. for the interaction of γ-rays with amorphous chalcogenide glasses [47]. These principles will apply to interactions between

amorphous chalcogenide glasses and γ-rays as well as x-rays, due to the similar photon energies relative to the bonding energies within the glasses. Photon radiation-induced static effects must comply with the following principles [47]:

1. All statistically possible transformations must be considered, which can be described by a single generalized equation: broken bond → created bond Additionally, a single broken bond can only result in the formation of another single bond.
2. The interaction of high energy radiation with the amorphous network may result in the formation of weaker 'wrong' bonds over the stronger bonds. This transformation of a previously strong bond into a bond consisting of a lower bonding energy causes a low-energetic shift of the absorption edge leading to the decrease in the bandgap of the system.
3. High energy radiation with the amorphous network may result in the formation of strong bonds over wrong bonds. The formation of strong bonds will lead to a high-energetic shift in the absorption edge and an increase in the bandgap of the system.
4. In a close packed glass network with high atomic density, only transformations with high energy differences may occur. This rule does not apply to amorphous chalcogenide glasses with low density due to the abundance of voids within the network.

Electron Beam Radiation

The effects of electron beam radiation interacting with chalcogenide glass are primarily dependent upon the energy of the electrons. The energy of an electron beam is

typically greater than 1 keV, which is in the same energy range as x-rays and γ-rays. Therefore, some similarities are expected between the interactions of electron beam radiation with chalcogenide glass and the interactions of x-rays and γ-rays with chalcogenide glass.

The similarities between the effects on chalcogenide glass due to high energy electrons and high energy photons include electron-hole pair generation and static structural changes in the glass network. The primary difference between these two types of radiations is the type of particle that delivers the radiation. Photon particles may be completely absorbed by particles within the glass after interactions. On the other hand, electrons will remain within the glass after interactions with the material unless there is a conductive path that allows them to escape. The buildup of negative charges within the glass is called charging [48]. For this reason, specimens in scanning electron microscopes are grounded through the sample holder.

In electron beam radiation, high energy electrons travel into the chalcogenide glass and interact with the structure of the material. These incident electrons collect at localized sites within the glass [49]. The collection of newly introduced electrons creates a localized and negatively charged electric field [49, 50]. The different sites where electrons are collected interact with each other through electrostatic forces [49, 50]. One study models the network as a layered network to demonstrate the interaction of negatively charged sites [50]. The negatively charged sites will experience repulsion and force the surrounding amorphous network to accommodate the electric fields, as illustrated in Figure 20 [50].

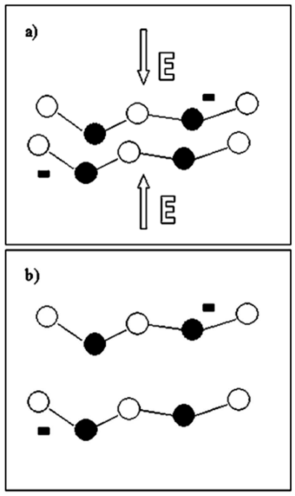

Figure 20. Interaction of negatively charged sites through a double layered model of the glass network (a) electrons accumulate at sites in the network (b) negatively charged sites repel each other creating voids within the network Reprinted with permission from [50] © 2002 AIP Publishing LLC.

The layers of structural units are connected by van der Waal's forces, but the electrostatic forces from charging at different localized sites overwhelm these van der Waal's forces. These repulsive electrostatic forces cause a localized expansion of the amorphous network, which leads to the formation of low pressure regions [51]. Within the low pressure regions, voids and new pathways are formed that allow the diffusion of ions within the glass. The network also experiences compressions in the opposing regions that cause the formation of high pressure and high density regions in the network [51]. The diffusion of mobile ions will be restricted in the regions of high pressure, which may lead to slower saturation of the ions in the glass.

CHAPTER 4: Ag-CONTAINING CHALCOGENIDE GLASSES AND MEMORY APPLICATIONS

Up to this point, chalcogenide glasses as well as the effects of radiation on these glasses have been described in detail. The incorporation of silver (Ag) into the chalcogenide glass enhances the optical, electrical, and mechanical properties of these glasses for their application in sensors, batteries, optical recordings, and memory devices [52-58]. The mechanisms of ion diffusion into the glass and some of the applications of these materials will be described further.

Mechanisms of Ag Diffusion into Chalcogenide Glass

Structural defects are inherently present within the network, such as dangling bonds, due to the amorphous nature of the glass. Other structural defects result from radiation exposure, such as charged defects, electric fields, voids, and structural and molecular changes [47-51]. Structural defects inherently present in the glass network along with defects created as a result of radiation exposure will increase the diffusion of ions, e.g. Ag^{+}, into the glassy network.

Ag Diffusion

The diffusion of Ag into chalcogenide glass will first be described with the absence of an external energy source (i.e., radiation). Although the dynamics of Ag diffusion from a concentrated silver source into the chalcogenide glass are not fully understood, it is believed to be a multiple step process, which is primarily motivated by

the principles of Fick's first and second laws [58]. At the interface between the Ag source and the chalcogenide glass, Ag atoms readily bond with chalcogen atoms from the glass, producing non-crystalline compounds [58-61]. The solid state chemical reaction between Ag and Se, and its corresponding Gibbs free energy (ΔG^0_{298}), that occurs at this interface for the As-Se system is provided in Table 1 [58]. The ΔG^0_{298} of each of these reactions are negative, allowing the reaction to occur in the absence of external energy [58]. Following this chemical reaction, a thin region of Ag-doped chalcogenide glass resides between the Ag source and the undoped chalcogenide glass.

Table 1. Chemical reactions occurring at the interface of Ag and As-Se glass [58]

Chemical Reaction	$\boldsymbol{\Delta G^0_{298}}$ **(kj/mol)**
$2Ag + Se \rightarrow Ag_2Se$	-25.13

The interface between the Ag-doped chalcogenide glass and the undoped chalcogenide glass stimulates the formation of holes, in addition to the holes present in the p-type chalcogenide glass [58, 59]. The holes migrate towards the Ag source and the Ag atom captures the charge carrier, as described in the following equation.

$$Ag + h^+ \rightarrow Ag^+ \tag{9}$$

Finally, the Ag^+ ions diffuse into the chalcogenide glass according to Fick's laws from the silver doped to the undoped region. Furthermore, the diffusion of silver in chalcogenide glasses resembles a step-like concentration profile [58].

Ag Diffusion with External Forces

Silver diffusion into chalcogenide glass may be expedited with the presence of a catalyst, which can be in the form of thermal energy, electromagnetic energy, electron beam radiation, or electric field gradient. Exposure to heat provides thermal energy to the system and promotes the generation of electron-hole pairs in the glass [62]. In the presence of thermal energy, Ag diffusion is expedited by the accelerated formation of holes, surpassing the chemical reaction in Table 1. Following the generation of holes, Ag ionizes and diffuses into the glassy medium, according to the process previously described.

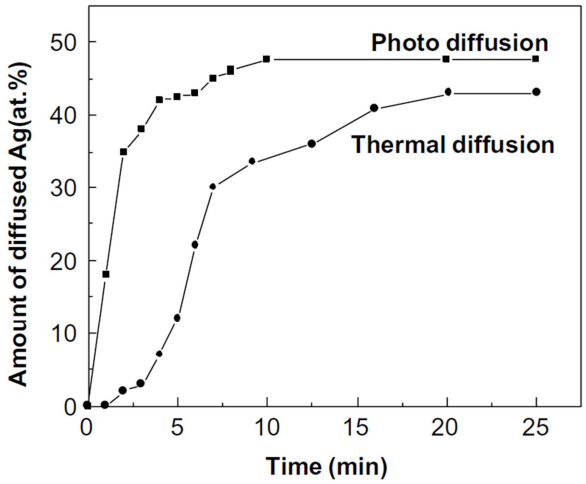

Figure 21. Comparison of photodiffusion and thermal diffusion of Ag in $Ge_{20}Se_{80}$ glass; saturation of Ag occurs faster with photo diffusion and also introduces more Ag into the glass than thermal diffusion
Reprinted with permission from [63] © 2004 Elsevier

Electromagnetic energy (i.e., photons) induced diffusion of Ag is called photodiffusion. It has been demonstrated that photodiffusion of Ag into Ge-Se glass occurs faster and introduces more Ag than thermal diffusion of the same system, as shown in Figure 21 [63]. The difference in the diffusion rates can be explained by the

influence of photons on the Ag atoms and the glass network. Similar to the circumstances with thermal energy, photons incident upon the glass network will cause electron-hole pair generation. The photons may also interact with the Ag, generating Ag^+ ions, which will then diffuse into the glass. Additionally, photons may cause defects within the glassy network in the form of broken bonds. The electric charge associated with these broken bonds will attract the Ag^+ ions.

The influence of electron beam radiation over Ag diffusion into chalcogenide glass is similar to that of electromagnetic radiation. The primary difference is due to charging of the glass. The collection of electrons at defect sites within the glass creates an electric field that attracts Ag^+ ions. Therefore, Ag diffusion in chalcogenide glass under the influence of electron beam radiation is the aggregate of all diffusion mechanisms that have been described: electron-hole pair generation in the glass; interactions with Ag leading to Ag^+ ions; interactions with the glass leading to broken bonds; and negatively charged sites within the glass that attract Ag^+ ions. The interplay of these diffusion mechanisms due to electron beam radiation may contribute to enhanced Ag diffusion compared to thermal Ag diffusion.

The final method for influencing the diffusion rate of Ag is through the application of an electric field gradient. This mechanism is the basis for the functionality of redox conductive bridge memory devices, which will be discussed later in this chapter.

Structures of Ag-Doped Chalcogenide Glass

After the diffusion of Ag into the Ge-Se glass network, Ag can either remain as a Ag atom or react with atoms within the glass network. Studies of Ag diffusion in the a-Se system have demonstrated the formation of two different crystallized phases of the binary

compound. The first phase is β-Ag_2Se, which is stable at room temperature. The β-phase has an orthorhombic crystal lattice and a conductivity of 9.8 x 10^{-6} (Ω^{-1} cm^{-1}) [53]. The second phase formed in the Ag-Se system is α-Ag_2Se, which is only stable at temperatures greater than 133 °C. The α-phase has a body centered cubic crystal lattice and a conductivity of 3.1 (Ω^{-1} cm^{-1}) [64]. In addition to the binary phase, a secondary diffusion product can be formed, also referred to as the ternary phase, which consists of Ag-Chalcogen-Ge structures (e.g., Ag_8GeSe_6). The conductivity of this phase is purely that of a semiconductor.

The presence of these various phases alters the conductivity of the film. Additionally, by controlling the movement of Ag within the glass, the conductivity can be set between distinct conductivity states. Mechanisms for introducing and removing Ag from the glass can be exploited through the application of an external electric field. This idea is the basis for one type of resistance change memory.

Basics of Resistance Change Memory

Resistance change memory (RCM) is an emerging solution as a replacement of the current leading technology in nonvolatile memory. Nonvolatile memory is a category of memory storage that maintains the stored data after the power supply has been removed. The basic qualification for RCM requires the device to store binary data in the form of two different resistive states. The binary states of ‘0’ and ‘1’ are defined by the high resistance state (HRS) and low resistance state (LRS), respectively. The HRS and LRS are also known as the off-state resistance and on-state resistance, respectively.

There are various types of materials and devices that are classified as RCMs. Current emerging forms of RCM devices include ferroelectric capacitors, phase-change

devices, and redox conductive bridge devices. These devices can be placed into a matrix of word lines and bit lines, which form the circuit design for Resistive Random Access Memory (RRAM). RRAM can be more specifically identified by the storage device within the matrix: ferroelectric random access memory, phase-change random access memory, and redox conductive bridge random access memory.

Ferroelectric Memory

The concept of ferroelectric memory is based upon the permanent presence of dipoles within ferroelectric materials. The polarization of the dipoles, which can be controlled through the application of an electric field, affects the resistivity to the films [65]. Ferroelectric memory devices have the structural form of a ferroelectric layer sandwiched between two metal electrodes, which control the electric field. Therefore, two distinctly different resistive states (HRS and LRS) can be created in the device. When the electric field is removed, the dipoles maintain their orientation. These devices are commonly called ferroelectric capacitors. The most common material used in these ferroelectric capacitors is lead-zirconium-titanate (PZT).

A single ferroelectric random access memory (FeRAM) cell is composed of a select transistor and a ferroelectric capacitor of the design illustrated in Figure 22. In the cell, the gate terminal of the transistor is connected to the word line and the drain terminal to the bit line. The state of the capacitor is measured by applying a small read voltage either to the bit or word line. Unfortunately, reading the device erases the memory state as well, so the cell must be re-programmed after every read cycle.

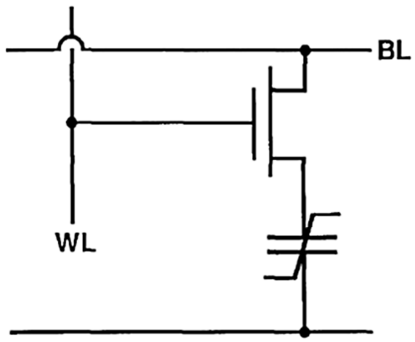

Figure 22. FeRAM cell design includes 1 access CMOS transistor and 1 ferroelectric capacitor
Reprinted with permission from [66] © 1988 IEEE

Phase-Change Memory

Phase-change memory (PCM) is based on the differences in reflectivity and resistance between the amorphous and crystalline phases of chalcogenide materials. The amorphous phase demonstrates high resistance and low reflectivity, while the crystalline phase demonstrates the opposite. A PCM device contains a top electrode, a chalcogenide layer, and a heating element. The amorphous phase is formed by applying a high current in a short period (~10 ns), which heats the chalcogenide past the melting temperature and rapidly cools it. The crystalline phase is formed by applying a smaller current, which maintains the temperature of the chalcogenide close to the melting point for a longer period (~1 µs) [67]. The phase-change mechanism has been widely used in re-writable CD and DVD technology. The HRS for PCM is typically on the order of 100x greater than the LRS. The cell design of phase-change random access memory is similar to that of FeRAM. The cell consists of a PCM device and a select transistor connected in the same manner as a FeRAM cell. A major disadvantage of PCM is the high current required to form the amorphous phase, which leads to a high power consumption.

The last form of RCM will be characterized in greater detail, since it is the subject of this study.

Redox Conductive Bridge Memory

Redox conductive bridge memory (RCBM) devices are based on the design of a metal-insulator-metal (MIM) structure, similar to the storage devices in ferroelectric memory and phase-change memory. The structural design of these devices includes one electrochemically inert electrode, which functions as the cathode, and one electrochemically active electrode, which functions as both the anode and the ion source in forward bias mode. Between these two electrodes resides the solid electrolyte insulating layer, which is the medium for ion conduction and bridge formation. This general structural design is illustrated in Figure 23, which shows the bridge formation.

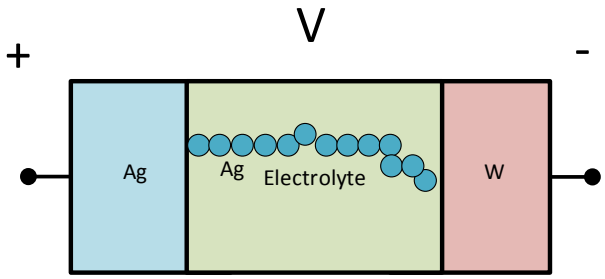

Figure 23. Basic design of RCBM device with conductive bridge in place; the device shown is in the ON-state or LRS; a forward bias is being applied

Switching Mechanisms in RCBM

The RCBM devices demonstrate bipolar resistive switching, which means the switching occurs asymmetrically. The polarity of the voltage required to write to the device is the reverse of that which is required to erase the device. The current-voltage characteristics of bipolar switching RCBM are presented in Figure 24. The stages where the device is in the off-state/HRS are highlighted in red. After a certain threshold during

forward bias, the device switches, indicating the set/write voltage. The current through the device is limited by the compliance current (cc). Application of the compliance current prevents excess current flow through the RCBM device, which can burn out the device. As the voltage approaches 0 on the reverse sweep, an ohmic relationship is observed between current and voltage. The inverse of this slope indicates the on-state resistance of the device. At some point during the reverse bias, the device switches off, indicating the reset/erase voltage. The off-state resistance of the device is given by the inverse slope of the red graph.

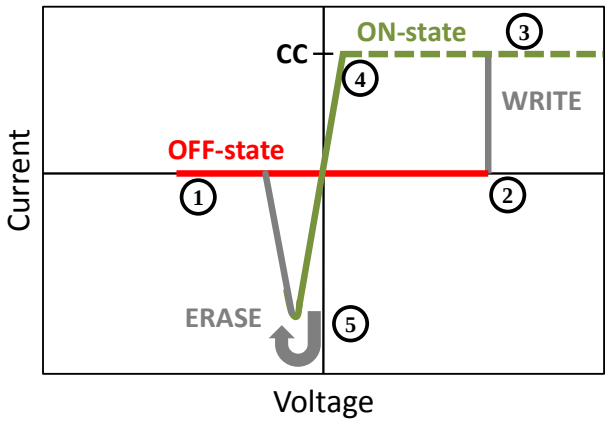

Figure 24. Bipolar resistive switching in RCBM: (1) a negative bias is applied and the device remains in the OFF-state; (2) as the bias increases positively, it eventually reaches V_{Th}; (3) device switches to ON-state and the current is limited by CC; (4) as the bias approaches 0, an ohmic relationship occurs; (5) when the negative bias reaches V_{Er}, the device switches off [68]

Reduction-Oxidation Mechanisms in RCBM

The present devices are called redox conductive bridge memory because the bridge formation occurs through the oxidation and reduction of the metallic ions. The evolution of the bridge growth in a RCBM device based on a Ag-chalcogenide glass-W stack is illustrated in Figure 25. During the initial forward bias, shown in Figure 25 (i), the anodic atoms (Ag) experience oxidation (i.e., Ag loses electrons and forms positively

charged ions). The positively charged ions migrate towards the negatively charged cathode (Figure 25 (ii)). With increasing forward bias, the ions saturate the electrolyte region nearest to the cathode. Nucleation of the ions occurs at the cathode (Figure 25 (iii)) and the ions experience reductions in their oxidation states (i.e., gain electrons) due to the negative charge of the cathode. The filament growth continues in this manner with increasing forward bias, until the conductive bridge is complete (Figure 25 (iv)).

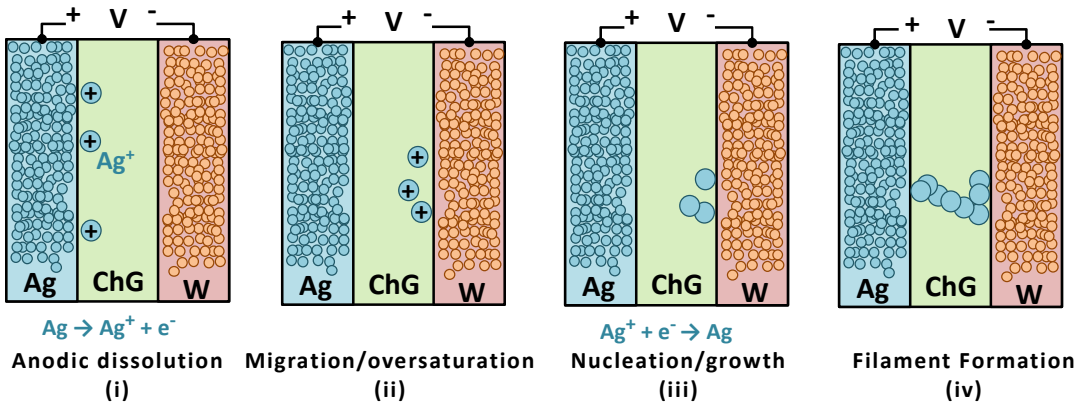

Figure 25. Oxidation-reduction bridge forming process during forward bias [69]

The device can be reset through the reverse of the bridge formation process. In the reverse bias mode, a negative voltage bias is applied to the electrochemically active (Ag) electrode while a positive voltage bias is applied to the electrochemically inert electrode. The reverse bias causes the oxidation of atoms that comprise the conductive bridge, resulting in the formation of ions. These newly formed ions drift towards the electrochemically active electrode, dissolving the bridge, where they become reduced at the electrode interface. Disruption of the conductive bridge returns the memory device to its original high resistive state.

The bridge formation and bridge dissolution processes enable the selection between a low or high resistive state. The state of the device is maintained after the withdrawal of the voltage bias. This qualifies RCBM devices as a form of nonvolatile memory.

The storage state of the device is determined by applying a small bias (read voltage) and simultaneously measuring the current. The amount of resistance, and therefore the resistive state, is easily calculated using the current-voltage relationship of Ohm's Law, shown in the following equation.

$$R = V/I \tag{10}$$

Since the read bias is significantly smaller than the write bias and erase bias, the device can maintain its storage state even after being read, making RCBM advantageous over ferroelectric memory. The major advantage of RCBM over PCM is the considerably lower power consumption, which is always a concern in our increasingly energy-conscious society. Other advantages of RCBM include faster write and erase times (~50 ns) and a high potential in scalability [67].

CHAPTER 5: EXPERIMENTAL PROCEDURE

So far, different forms of radiation have been discussed, as well as their effects on chalcogenide glasses. Electromagnetic radiation, which is indirectly ionizing, can cause photodarkening/photobleaching, structural modification, and electron-hole pair generation. Electron beam radiation, which is directly ionizing, can also cause these effects in addition to charging and structural rearrangements. Electromagnetic radiation influences the conductivity of Ag-containing chalcogenide glasses through photodiffusion. These photodiffused films are highly applicable as an active medium in redox conductive bridge memory (RCBM). Since radiation promotes the diffusion of Ag in chalcogenide glasses, the exposure of a-Ge_xSe_{100-x} based RCBM devices to radiation is expected to change the device performance parameters.

In this work, various studies on Ge_xSe_{100-x} films were conducted in order to fully characterize their behavior in the presence of radiation. Following material characterization studies, RCBM devices were fabricated using Ge_xSe_{100-x} films as the active medium through which the conductive bridge forms. The performances of the RCBM devices were characterized before and after radiation exposure. The following chapter describes the film and device fabrication methods as well as the characterization methods, and experimental conditions used throughout the experimental studies.

Film Fabrication

Amorphous Ge_xSe_{100-x} Films

Structural characterization studies due to the effects of x-rays and electron beam were conducted on thermally deposited bare films onto a p-type Si wafer substrates with a 200 nm thick thermally grown wet-SiO_2 insulator. The low partial pressure of Ge relative to Se caused a faster deposition rate in Se. Therefore, bulk glasses of the desired film compositions were placed into a tungsten (W) crucible with a semi-Knudsen cell design, illustrated in Figure 26. The semi-Knudsen cell equalized the pressure so that the deposition rates of Ge and Se atoms were equal and the deposited film compositions were close to that of the bulk glass.

The films were deposited using a Cressington 308R evaporation system at pressure of $1x10^{-6}$ mbar. The deposition rates of the films were monitored using a 6 MHz quartz crystal resonator. The substrate was placed directly above the crucible and slowly rotated to ensure uniform distribution of the film thickness across the substrate. The films were deposited at a rate of ~3 nm/min. The thicknesses of the films used for the material characterization studies were 75 nm for these two radiation studies.

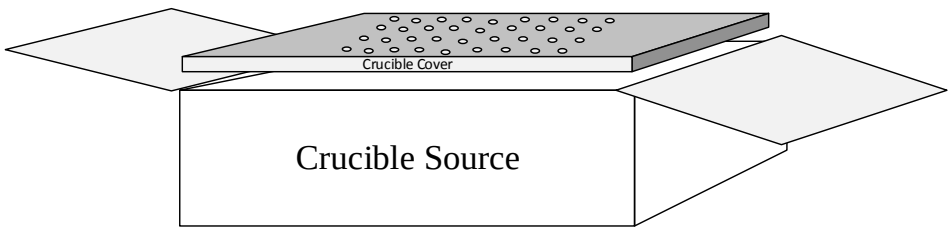

Figure 26. Design of semi-Knudsen cell crucible used for thermal evaporation of amorphous Ge_xSe_{100-x} films; the mesh pattern of the cover equalizes the partial pressures of Ge and Se in order to achieve ideal film compositions

Material characterization studies on the visible light induced effects were conducted on films thermally deposited onto Indium-Tin-Oxide (ITO) coated microscope

slides. These studies required the use of a transparent substrate in order to monitor the transparency of the films. Deposition of films for these studies was conducted in the same manner with the same equipment; however, these films were 1.0 µm in thickness.

Ag Source Formation

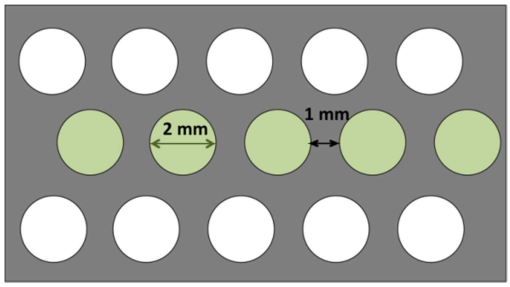

Figure 27. Shadow mask utilized in formation of thermally deposited Ag sources; white dots were sealed so only a single row of Ag dots were deposited (shown in green)

Studies characterizing Ag diffusion and the subsequent diffusion products were conducted on a-Ge_xSe_{100-x} films with a circular Ag source. The a-Ge_xSe_{100-x} film was deposited using thermal evaporation per the process described previously. Ag was deposited using the same method; however, Ag pebbles were placed into an open tantalum (Ta) crucible, rather than the W semi-Knudsen cell used for chalcogenides. The formation of the Ag source was achieved through the use of a shadow mask, which is illustrated in Figure 27. After deposition of the 75 nm thick chalcogenide film, the shadow mask was placed atop the thermally deposited film. Subsequently, 100 nm of Ag was thermally deposited onto the chalcogenide film. The resulting Ag source dots were 2 mm in diameter with 1 mm spacing between. A single row of Ag source dots were deposited, as indicated by the green dots. The white dots represent locations where the silver was prevented from depositing onto the chalcogenide film. This mask was used in order to provide a large distance of Ag diffusion in one direction (towards the white

circles), allowing the freedom to study a range of radiation doses and different types of radiation.

RCBM Device Fabrication

The fabricated RCBM devices were based on a W/a-Ge_xSe_{100-x}/Ag vertical stack, in which W was the electrochemically inert electrode, a-Ge_xSe_{100-x} was the medium in which the conductive bridge could form, and Ag was the electrochemically active electrode, which provided the ions for the formation of the conductive bridge. The fabrication of these devices involved nine processing steps, including three photolithography steps, all of which are outlined below and illustrated in Figure 28, with specific details to follow.

1. Sputtering of W electrode and SiO_2 device isolation layers
2. 1st photolithography step (via formation)
3. Wet etch of SiO_2 forming the via
4. Thermal evaporation of Ge_xSe_{100-x} and Ag
5. Ag photo diffusion
6. 2nd photolithography step (Ag electrode)
7. Thermal evaporation of Ag for the electrode
8. 3rd photolithography step (W electrode)
9. Wet etch SiO_2 forming the W electrode

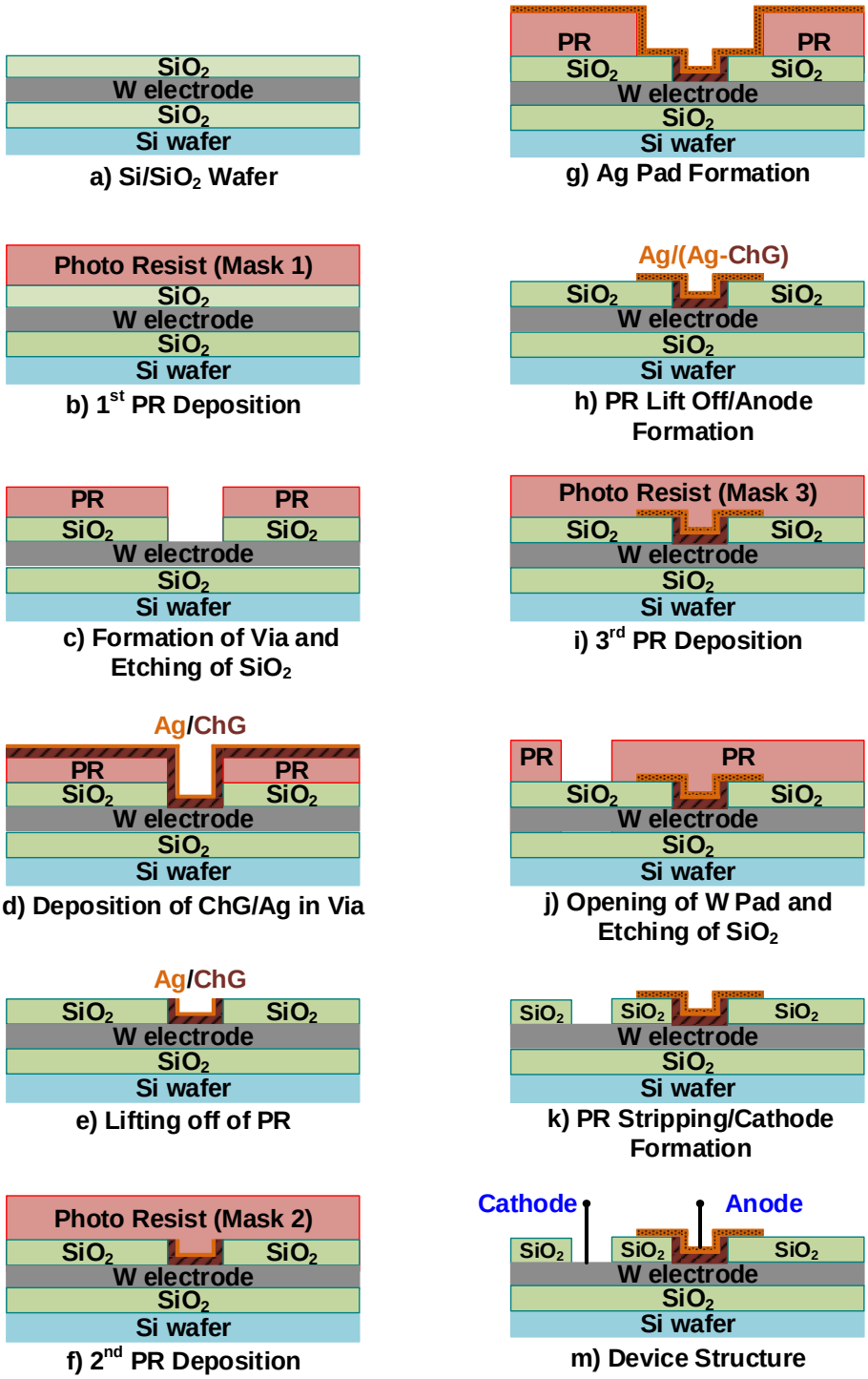

Figure 28. Process flow for W/a-Ge_xSe_{100-x}/Ag RCBM devices

Substrate Preparation

The RCBM devices were fabricated on a 4-inch, 380 µm thick, boron doped (p-type), single-side polished Si wafer with <100> orientation. Initially, a 200 nm insulating layer between the device and substrate was formed through the wet-oxidation process. This and all subsequent photolithography and wet etching processes were performed in a Class 1000 cleanroom.

Sputtering of W and Field Isolation SiO_2

The electrochemically inert W electrode is located at the bottom of the device stack. In the fabricated RCBM devices, all W electrodes are electrically shorted together through a continuous W film. The W film was deposited using an AJA Orion 5 Sputter Machine (Model No. ATC ORION 5 Sputtering System). All sputtered materials were deposited at a vacuum pressure of $6x10^{-6}$ mbar. Deposition of the W layer was achieved using a DC input power of 200 W at a deposition rate of 1.20 Å/second. Immediately following W deposition, a 100 nm layer of insulating SiO_2 was sputtered onto the substrate. The SiO_2 was deposited using an RF power source, in order to avoid charge build up on the target, at a rate of 0.66 Å/second. Multiple guns within the sputter tool allow for consecutive film deposition without breaking the chamber vacuum, eliminating interlayer contaminants.

Photolithography

All three photolithography steps follow the same recipe. The 1^{st} photolithography step, in the device formation, exposes small areas in the SiO_2 layer, which will later be etched to form the device vias. This procedure has been optimized specifically for the fabrication of these RCBM devices, and is summarized in the flowchart of Figure 29.

Step (a), which is not applicable to the 1st photolithography step, requires heating the 1165 Microposit Remover to 65 °C, in order to remove the photoresist from the previous photolithography step. The wafer was placed into the solution for 2 minutes, with continuous agitation in order to avoid photoresist re-deposition. In Step (b), about 5 ml Hexamethyldisilazane (HMDS), which improves photoresist adhesion and aids the liftoff process, was applied to the wafer. Following this, the wafer was spun using a Headway Spin Coater (Model: PWM 32-PS-R 790) at 5000 rpm for 35 seconds to evenly distribute the HMDS. In Step (c), 15 ml of SPR 220 3.0 photoresist was applied to the wafer and spun at 6000 rpm for 35 seconds. Step (d) was a pre-exposure bake of the photoresist at 115 °C for 90 seconds, which removes excess moisture from the photoresist. The photoresist was exposed to high intensity UV light (22mW/cm^2) for 9 seconds using a Quintel Contact Aligner (Model: Q-4000). Finally, the wafer was submerged in the MF26A developer for 90 seconds, completing the photolithography process and producing a patterned wafer.

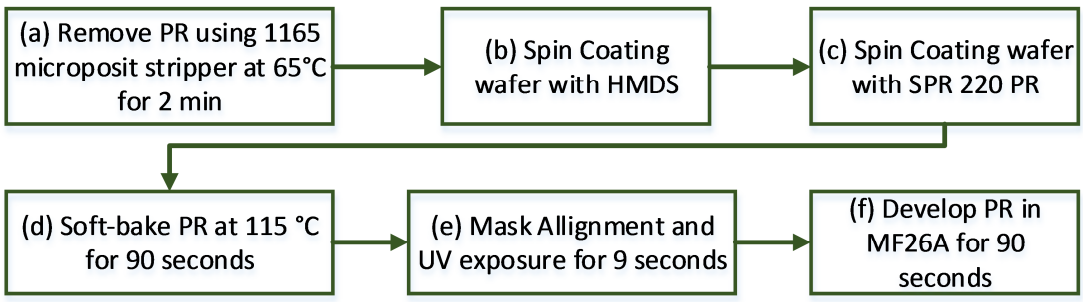

Figure 29. Photolithography process developed for RCBM devices using SPR 220 photoresist

Wet Etching of SiO_2

Wet etching of SiO_2 was performed twice, with the same procedure, in this device fabrication process: first to form the via and second to expose the W pad. Etching of SiO_2 was achieved using 20:1 Buffered Oxide Etch (BOE), which was a solution of 20 parts Ammonium Fluoride to 1 part Hydrofluoric acid. The etch rate of SiO_2 was 8 Å/second. Correspondingly, the wafer was submerged in the etchant for 2 minutes to remove 100 nm of SiO_2. After the first etching step, a cross-sectional view of the device will be similar to the illustration in Figure 28c.

Thermal Evaporation of Ge-Se Active Layer

After the via was formed, it was filled with 75 nm of a-Ge_xSe_{100-x} thin film, as illustrated in Figure 28d, using thermal evaporation. Without breaking vacuum, a small 15 nm layer of Ag was deposited over the chalcogenide film. The process of thermal evaporation was described in a previous section (page 47). The deposition of Ag at this stage is an important detail critical to the device formation. Chalcogenide glass will dissolve in a basic solution (i.e., the MF26A developer). Consequently, a thin protective Ag layer over the chalcogenide film prevents its dissolution during the subsequent photolithography steps.

Following the deposition of the thin Ag layer, the Ag was photodiffused into the chalcogenide filled via using a UV light source with an intensity of 1.5 W/cm^2. The reasoning for this is two-fold. First, the photodiffused Ag increases the strength of the chalcogenide against dissolution in the developer. Second, photodiffusion of Ag greatly increases the reliability and endurance of the devices [70].

Ag Pad and W Pad Formation

The remaining process steps are a combination of processes that have already been described in detail. After the via was filled with the chalcogenide and Ag thin films, the formation of the Ag pad, which will act as the electrochemically active anode was the next process step. Formation of the Ag pad was initiated by the 2nd photolithography step using the second mask for Ag pad formation. Silver was thermally deposited over the patterned photoresist with thickness of 100 nm (Figure 28g). Next, the final photolithography step begins with lift-off, revealing the fully formed Ag anode (Figure 28h). After the 3rd photolithographic process, openings in the photoresist layer (Figure 28j) provided access to the SiO_2 layer. The SiO_2 was etched, revealing the underlying W film that forms the electrochemically inert cathode. The final fabrication step was to remove the remaining photoresist. The resulting cross-sectional view of the device structure is illustrated in Figure 28m.

Film Characterization Methods

Thermally deposited bare and silver source containing films were characterized using various methods including Raman spectroscopy, Energy Dispersive Spectroscopy (EDS), and X-ray Diffraction (XRD). The scientific value and settings of these methods are described in this section.

Raman Spectroscopy

The amorphous nature of the Ge-Se films creates some uncertainty in the structural organization the network. Raman spectroscopy studies provide valuable information regarding the presence of various structures within the film as well as the manner in which these structures react in the presence of an external force (i.e.,

radiation). Raman spectroscopy studies were conducted using a Horiba Jobin Yvon T6400 triple monochromator with liquid-nitrogen-cooled multichannel coupled-charge-device (CCD) detector. Films were excited with a 514.5 nm green laser with power of 90 mW. Measurements were conducted at a temperature of 100 K and pressure of 10^{-3} Torr to avoid photoinduced changes in the studied film by the laser light. Each Raman spectrum was acquired over a period of 120 seconds with multiplicity of 3 in order to eliminate noise observed in the spectrum. Additionally, since the distribution of structural units may vary throughout a single sample, multiple spectroscopy measurements were taken at various locations on the sample in order to obtain an accurate representation of each film.

The experimental Raman spectra were fitted with the sum of multiple Gaussian distributions centered at specific wavenumbers, which correspond to the vibrational modes of the various structures. The Gaussian peak positions of each structure within chalcogenide glasses have been previously determined through modeling studies [71, 72]. Further descriptions of these vibrational modes are provided with the presentation of the Raman data. Prior to fitting the Gaussian curves, each spectrum was fitted to a baseline and normalized to an intensity of 1.0 ascribed to the corner-shared peak height, which isolates the characteristic vibrational modes and permits comparison between spectra. The relative quantities of the structures observed are ascertained through comparison of the integrated areas of the Gaussian distributions.

Energy Dispersive Spectroscopy (EDS)

The exact compositions of the Ge-Se films have been determined through Energy Dispersive Spectroscopy. Due to errors inherent in the thermal evaporation process, the

composition of a deposited film is not equivalent to that of the source bulk glass. The exact composition of a film is valuable information when characterizing any of its properties. Therefore, EDS studies are necessary for every film that is characterized. Energy Dispersive Spectroscopy was conducted using a Hitachi S-3400N II Scanning Electron Microscope with an Oxford Instruments Energy + EDS system. These measurements were conducted at working distance of 10 mm and 2000x magnification with a 90 second collection time. Each sample was measured at five different locations to obtain an accurate average and standard deviation.

Additionally, mapping profiles of Ag diffusion in the Ge-Se films were obtained using the same equipment. The mapping of Ag diffusion was performed on a-Ge_xSe_{100-x} films with a thermally deposited circular Ag source, which was previously described (see page 48). The mapping profile is a compilation of 20-25 frames. Each frame was measured with an accumulation time of 90 seconds at a working distance of 10 mm, achieving an appropriate contrast level (0-10 arbitrary counts). The resulting diffusion profile provides an insight into the diffusion rate of Ag with radiation exposure.

X-ray Diffraction (XRD)

Silver bonding with chalcogen elements results in the formation of crystalline structures, which can be measured through x-ray diffraction (XRD). The XRD patterns of the diffused Ag were measured using a Bruker AXS D8 Discover X-ray Diffractometer equipped with a NaI(Tl) scintillation detector and Cu-K_α x-ray source (λ =0.1506 nm). The XRD Commander software was utilized in locked-coupled scan mode with 2θ ranging from 15° to 90° (0.05° step size and 1.2 seconds/step). The resulting XRD patterns contained spikes in the intensity at specific 2θ values, which correspond to the

particular molecular compounds and phases present within the film. Accordingly, a perfectly amorphous film will provide an XRD pattern with an overall low intensity and no spikes.

Device Characterization Method

A major factor in the competition for the next generation memory solution is the endurance of the device. The current leader in memory technology (i.e., Flash) is required to withstand at least 10^3-10^7 switching cycles. Therefore, determining the effects of radiation on the endurance of the proposed devices will indicate if they are a viable candidate for the next generation memory solution in radiation-prone environments.

The fabricated a-Ge_xSe_{100-x} based RCBM devices were characterized using an HP 4146 parameter analyzer. The probe station used for device characterization was equipped with gold probes and a Faraday cage, which isolated it from external sources of noise and diminished charge buildup within the measuring cables. The devices were characterized with a DC voltage bias sweep, ranging from -0.75 to 2.0 V across the W and Ag electrodes, while simultaneously recording the current. In order to achieve 10^5 switching cycles within a reasonable amount of time, a signal generator was utilized in addition to the parameter analyzer. The signal generator was programmed to supply a square waveform with a minimum of -0.75V, a maximum of 2.0V, and a period of 5 ms. The signal generator was interrupted at several times during the testing, in order to record the current-voltage characteristics at various cycles. The current-voltage characteristics obtained during the endurance testing were analyzed and performance indicators, such as write voltage, erase voltage, on-state resistance, and off-state resistance, were extracted to characterize the devices.

CHAPTER 6: INFLUENCE OF SUB-BANDGAP LIGHT ON CHALCOGENIDE GLASS

Before studying the effects of ionizing radiation over the Ge-Se glasses, experiments were conducted using low energy photons (visible light). The nature of the effects under such radiation is, to a great extent, well defined and understood. The motivation for this experiment was to bear knowledge from these types of effects and apply it to the unexplored subject of ionizing radiation.

The effects of low energy photons on a-Ge_xSe_{100-x} films were studied for the compositions of $Ge_{29.2}Se_{70.8}$, $Ge_{32.1}Se_{67.9}$, and $Ge_{39.5}Se_{60.5}$. Insight into the origin of transient and metastable sub-bandgap light-induced effects in a-Ge_xSe_{100-x} systems across the glass forming region are presented further in this chapter. The crossover from transient photobleaching (PB) in compositions close to $GeSe_2$ to the mixture of both transient photodarkening (PD) and metastable PB in the Ge-rich composition was experimentally observed with the two-laser beam technique.

Radiation Exposure Conditions

The photo-induced changes in the films were observed by the two-laser beam transmittance method [38]. In this method, a low intensity 0.29 mW/cm^2 'probing' laser diode with a wavelength of 655 nm (above the absorption edge) was continuously used to monitor changes in the transmittance (T) and a high-intensity 200 mW/cm^2 'pumping' laser, emitting light with a wavelength of 405 nm, was employed to produce PD/PB

effects. The pumping laser operated in an on/off switching cycle, in which the on-period is also called the pumping period and the off-period is called the rest period. The total time of one pumping and rest cycle was 800 seconds, and the total accumulation time was 4,800 seconds. Both beams were focused on the same area of the sample, with the pump completely overlapping probe light. The samples were measured under atmospheric pressure and room temperature conditions. As a result, relative changes in the transmittance T/T_o as a function of time were calculated.

Results

Transparency and Raman spectroscopy measurements were performed to characterize the photoinduced effects. The transparency measurements for $Ge_{29.2}Se_{70.8}$ are shown in Figure 30. Additionally, the measurements in transparency for the $Ge_{32.1}Se_{67.9}$ and $Ge_{39.5}Se_{60.5}$ compositions are presented in Figure 31.

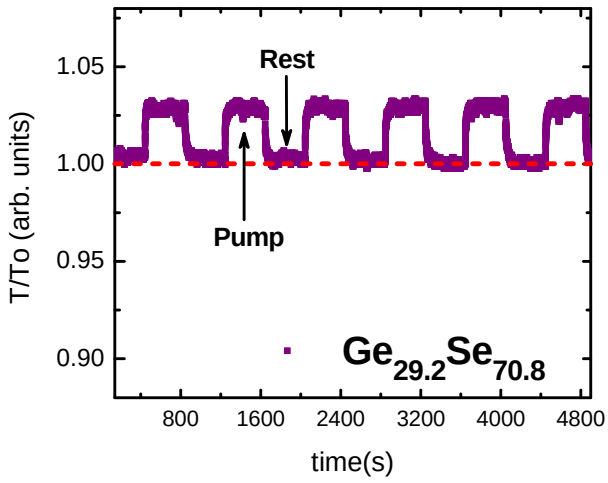

Figure 30. Time evolution of $Ge_{29.2}Se_{70.8}$ film transparency showing transient photobleaching (increased T/To during pumping cycles and returning to original state during rest cycles)

The transparency measurements demonstrate a difference in the photo-induced effects that are observed for a-Ge_xSe_{100-x} glasses depending on the compositional

variation. There is a critical Ge concentration, which is essential for the regarded processes. It was determined to be around 30%. Below this content, for x=29.2% only, the transient effect was present, above it, for x = 32.1% and x = 39.5%, metastable effects emerged. Therefore, when $Ge_{29.2}$ $Se_{70.8}$ was illuminated with the pumping beam, its relative transmittance rapidly increased by 3% and saturated, as seen in Figure 30. During the following rest period, transmittance reverted back to 1.0 and the effect dissipated. After continued on/off cycling, this behavior remained unchanged.

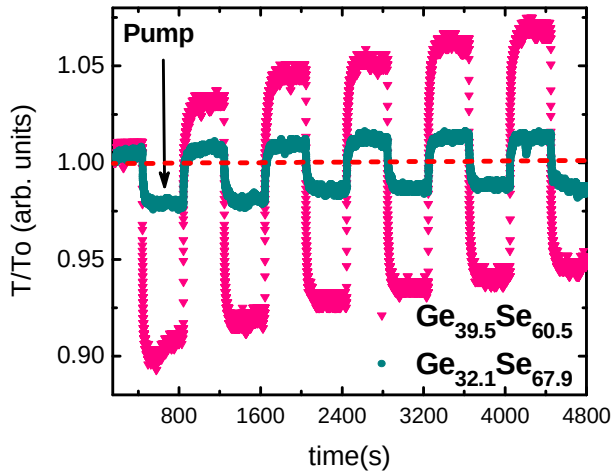

Figure 31. Time evolution of $Ge_{32.1}Se_{67.9}$, and $Ge_{39.5}Se_{60.5}$ film transparency showing transient photodarkening (decreased transparency) and metastable photobleaching (permanently increased transparency)

Films exceeding the critical Ge concentration demonstrated a combination of transient photodarkening (during the pump period) and metastable photobleaching (during the rest period) effects, as illustrated in Figure 31. Furthermore, increasing the Ge content in the films increased the magnitude of both transient and metastable changes. In the case of $Ge_{32.1}Se_{67.9}$, a decrease in the transmittance by 2.5% was observed upon light irradiation. During the resting period, a rapid increase in the transparency was observed. In fact, a 0.9% increase in transmittance was observed, implying the effects of PB.

Gradual increases in the PB were observed with every switching cycle, resulting in an increase in the transmittance by 1.5% after five total cycles. A similar trend of crossover from transient PD to metastable PB was seen in the $Ge_{39.5}Se_{60.5}$ composition, with a more pronounced magnitude of the effect. Thus, overall metastable PB attained a 7% increase in the transmittance above the initial level.

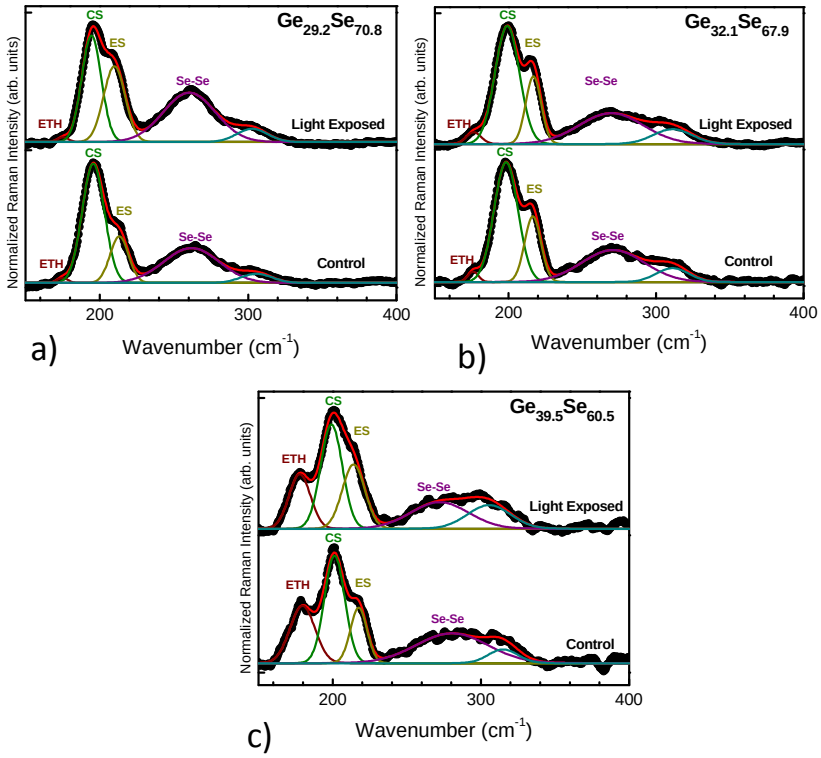

Figure 32. Raman spectra of films before and after light exposure: a) $Ge_{29.2}Se_{70.8}$, b) $Ge_{32.1}Se_{67.9}$, c) $Ge_{39.5}Se_{60.5}$

Structural changes in a-Ge_xSe_{100-x} films exposed to sub-bandgap light were characterized using Raman Spectroscopy. The Raman spectra of films before and after light exposure are displayed for all compositions in Figure 32a, b, and c. The Raman spectra verify the presence of four different structural units: ethane-like bonding (ETH) structures (Se_3-Ge-Ge-Se_3) average vibrational mode at 175 cm^{-1}, corner-sharing (CS)

tetrahedral structures (Ge-Se-Ge) average vibrational mode at 195 cm^{-1}, edge-sharing (ES) tetrahedral structures at 213 cm^{-1} [73-76], Se-Se chains and rings are present at 265 cm^{-1} [77, 78], and the final band that is observed in the Raman spectra at 307 cm^{-1} is attributed to the asymmetric vibration of the same edge-shared tetrahedral previously mentioned [78-80].

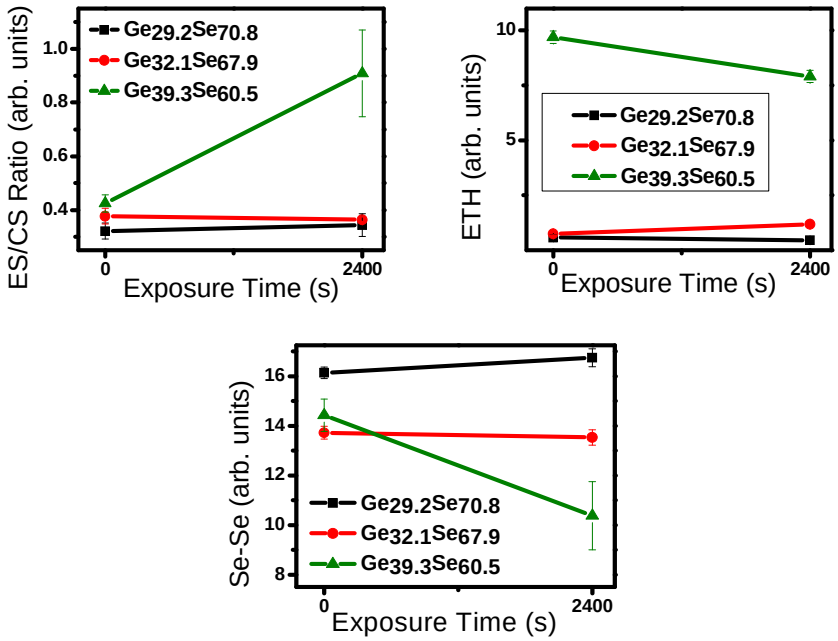

Figure 33. Structural changes observed from Raman spectra: a) ratio of ES areal intensity to CS areal intensity, b) areal intensity of Se-Se chains, and c) areal intensity of ETH structures

Deconvolution of the Raman spectra reveals changes in the relative quantities of the ES, CS, Se-Se, and ETH structural units. This information, presented in Figure 33a, b, and c, is obtained by integrating each of the fitted Gaussian curves to calculate to total area of each curve. According to Raman analysis of the $Ge_{39.5}Se_{60.5}$ films, the ES/CS ratio increased from 0.42 to 0.91. The concentration of ETH and Se-Se structures decreased from 9.8 to 7.9 and from 14.6 to 10.2, respectively. Negligible changes in the structural

units were detected in the films with lower Ge content. Any of the observed changes are within the error of the Raman measuring system.

Discussion

First, the changes observed in the films of compositions $Ge_{29.2}Se_{70.8}$ and $Ge_{32.1}Se_{67.9}$ are considered. The variety of these effects are attributed to the high flexibility of the glassy matrix due to the high Se concentration, which becomes more and more restricted with increasing Ge content. The flexibility of the glasses in this concentration region and the dominance of Se in their composition suggest that the photo-excitation clearly follows the pathway well-known in a-Se, namely it involves the lone pair electrons of Se atoms [81]. Because of the floppiness of the system in this composition, one could also expect some structural changes like flipping of the Se chains or intermolecular reactions like changes to the van der Waals distances due to Coulomb interactions of created defects at light illumination. However, their experimental identification is difficult. On the other hand, the changes in the transmittance of the $Ge_{32.1}Se_{67.9}$ suggests that due to the slightly higher Ge content in these films, in materials with Ge content greater than 30%, the early stages of material modifications emerge, leading to the rise of the PB with increasing light illumination.

For the $Ge_{39.5}Se_{60.5}$ film composition, the experimental data demonstrate a mixture of the transient PD and metastable PB effects that was also reported by other research groups [38]. The Raman analysis provides some insight into the metastable changes: the homo-polar bonds, i.e. ETH and Se-Se, are converted into the tetrahedral Ge-Se bonding. The photo-excitation in the $Ge_{39.5}Se_{60.5}$ system is found to induce breakage of the Ge-Ge chains and as a result many dangling bonds at the Ge atoms are

generated. Because of deficiency of the lone pair states at the Se atoms, the dangling bonds cannot be saturated. Therefore, the defect states appear in the band gap causing the band gap shrinkage by ~0.2 eV, which manifests in the transient PD effect during the light exposure. The increase in PD amplitude with growing Ge content is related to further suppression of the concentration of the Se lone pair states.

In the post-excitation regime, we observe an appearance of the newly formed heteropolar CS and ES bonds and a subsequent reduction in the homopolar ETH and Se-Se bonds. The heteropolar bonds are more energetically favored compared to the homopolar ones [82]. The increase in ES/CS ratio with a simultaneous decrease in ETH and Se-Se structures suggest that large quantities of Ge-Ge bonds and corresponding Se-Se bonds are broken and converted predominantly to ES tetrahedral units as a result of relaxation in the post-light-exposed period. The reversibility of the PB effect also supports the hypothesis that its nature is mainly a function of structural reorganization and not of oxidation.

Conclusion

Photo-induced changes in Ge_xSe_{100-x} films were experimentally studied by the two-laser beam technique, where a high powered laser was used to produce photodarkening (PD)/photobleaching (PB) and operated in an on/off regime with a period of 800 sec. A weak-power laser with a higher wavelength light was continuously used to monitor the changes in the sample transmittance. Photodarkening (red shift of the absorption edge) and photobleaching (blue shift of the absorption edge) were observed in the different film compositions: reversible PB on $Ge_{29.2}$ $Se_{70.8}$; reversible PD on $Ge_{32.1}$ $Se_{67.9}$, which diminished after the optical excitation was removed. Additionally, a

combination of the reversible PD and irreversible PB effects was observed in $Ge_{39.5}Se_{60.5}$. It can be stated that the selenium atom influences the PD effects with corresponding mechanisms, similar to the results reported in [83, 84]. Raman spectroscopy was performed to collect data about the structural changes accompanying the optical effects. The photobleaching is a result of light-induced bond transformation from homo-Ge-Ge, Se-Se to hetero-Ge-Se bonds. On the contrary, the reversible effects are related to the formation of defects, corresponding to the occurrence of lone-pair electrons on the chalcogen atoms. This experiment proved that in films with a high Se concentration, the PD effect is governed by the presence of lone-pair electrons associated with Se. In films with a higher Ge concentration, related effects occur. That is to say, the concentration of the chalcogen element and the presence of the lone-pair electrons govern the effects that appear, and the rigidity of the structure is of a secondary importance.

CHAPTER 7: X-RAY INDUCED EFFECTS IN THIN Ge-Se FILMS AND RCBM DEVICES

Similar to visible light, x-rays are electromagnetic waves that affect the chalcogenide glass films and the RCBM devices containing such films in an analogous way. The effects of x-rays on a-Ge_xSe_{100-x} thin films and a-Ge_xSe_{100-x} films in contact with an Ag source were studied. Results from these studies were then related to the performances of RCBM devices after x-ray exposure.

Radiation Exposure Conditions

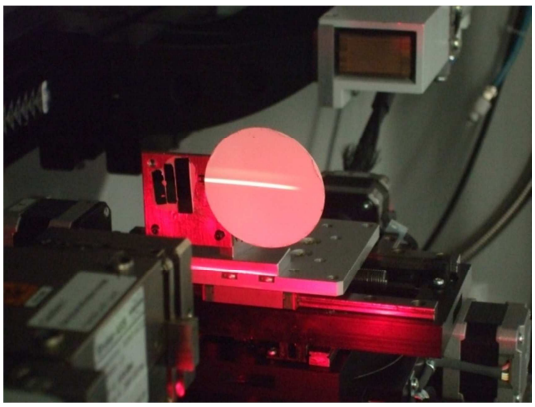

Figure 34. Experimental setup of x-ray irradiation

X-ray irradiation experiments were conducted on a Bruker AXS D8 Discover X-Ray Diffractometer with Cu $K\alpha_1$ radiation (λ=1.5406 Å) functioning as a source of x-rays. The x-ray beam was configured in parallel beam geometry after passing through a Göbel mirror. The beam intensity was 8.7×10^8 counts per second using an accelerating voltage of 40 kV and electron beam current of 40 mA. The dimensions of the beam were

6 mm in height and ~4 in wide. The sample holder was aligned to the edge of the motorized stage. The motorized stage itself was moved to the closest position to the beam exit (x at position 40). The setup is shown in Figure 34. The precise location of the irradiated area was observed by using a florescent paper. The dose rate in this set-up was determined experimentally to be 6.0 krad/hour using a RADFET device. The samples that were studied included 100 nm a-Ge_xSe_{100-x} films (see page 47), 100 nm a-Ge_xSe_{100-x} films in contact with a Ag source (see page 48), and RCBM devices (see page 49).

Film Characterization

Structural changes in a-Ge_xSe_{100-x} films were characterized using Raman Spectroscopy. The Raman spectra of three different films (x=22.6, 32.4, 44.4) were measured after being exposed to five different doses of x-rays (0, 12, 24, 36, and 60 krad). The Raman spectra of films exposed to 0 krad and 60 krad for $Ge_{22.6}Se_{77.4}$, $Ge_{32.4}Se_{67.6}$, and $Ge_{44.4}Se_{55.6}$ are displayed in Figure 35a, b, and c, respectively. The Raman spectra verify the presence of four different structural units: ethane-like bonding (ETH) structures (Se_3-Ge-Ge-Se_3) average vibrational mode at 178 cm^{-1}, corner-sharing (CS) tetrahedral structures (Ge-Se-Ge) average vibrational mode at 200 cm^{-1}, edge-sharing (ES) tetrahedral structures at 216 cm^{-1} [73-76], and Se-Se chains and rings are present at 270 cm^{-1} [77, 78]. The final band that is observed in the Raman spectra is attributed to the asymmetric average vibration of the edge-shared tetrahedral at 308 cm^{-1} [78-80].

Deconvolution of the Raman spectra provides information on the relative quantities of each of the structures within the films. This data, as a function of the radiation dose, is presented in Figure 36. The changes in the ratio of edge-sharing

tetrahedra to corner-sharing tetrahedra are graphed in Figure 36a. In the range from 0 to 24 krad, the ES/CS ratio of the $Ge_{22.6}Se_{77.4}$ and $Ge_{44.4}Se_{55.6}$ films follow a similar trend with x-ray exposure. In the same dose range, relatively no changes were observed in the $Ge_{32.4}Se_{67.6}$ ES/CS ratio.

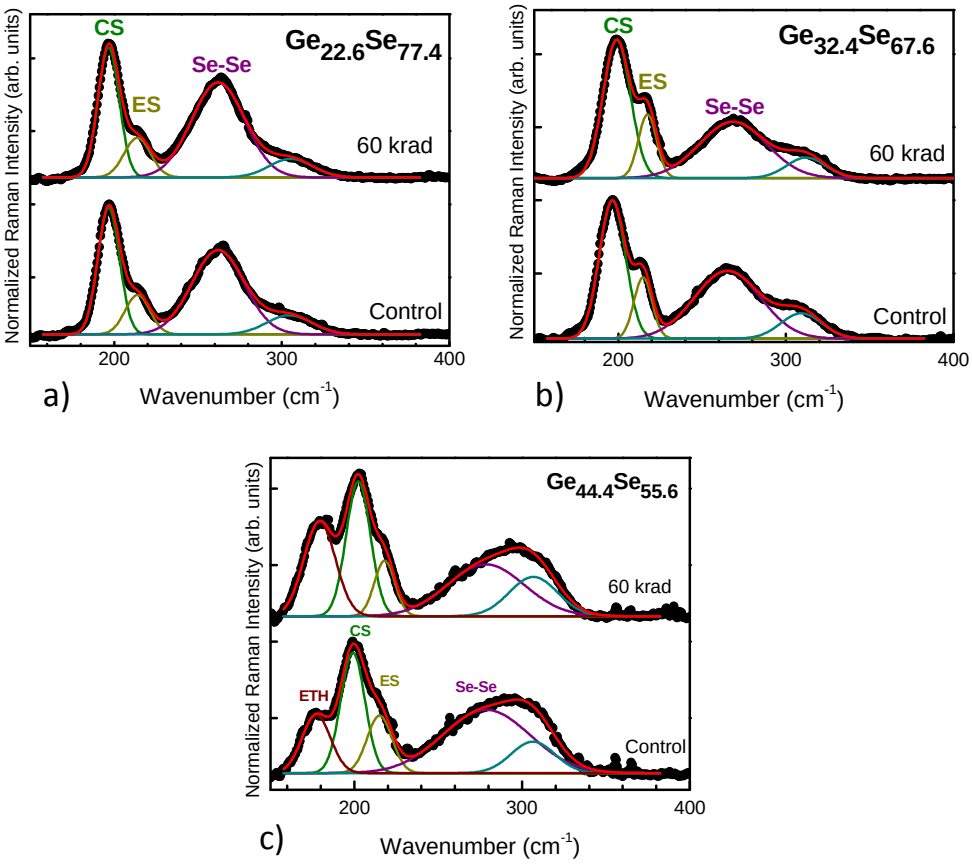

Figure 35. Raman spectra of x-ray control and highest dose (60 krad) exposed films for a) $Ge_{22.6}Se_{77.4}$, b) $Ge_{32.4}Se_{67.6}$, and c) $Ge_{44.4}Se_{55.6}$

For the $Ge_{22.6}Se_{77.4}$ and $Ge_{44.4}Se_{55.6}$ films, the radiation effects are characterized with both a decrease in the ES/CS ratio and, accordingly, a decrease in the Se-Se chains. Between 24 and 36 krad, both $Ge_{22.6}Se_{77.4}$ and $Ge_{44.4}Se_{55.6}$ experienced an increase in the ES/CS ratios and Se-Se chains. At radiation over 36 krad, both of the films demonstrated

decreasing ES/CS ratios again and the $Ge_{44.4}Se_{55.6}$ film exhibited a corresponding decrease in the Se-Se chains. Only the $Ge_{44.4}Se_{55.6}$ films illustrated the presence of enough ETH structures to be registered in the curve fitting. In the $Ge_{44.4}Se_{55.6}$ films, increasing the radiation dose from 0 to 36 krad resulted in the increase in ETH structures, and their amount remained constant at radiation above 36 krad.

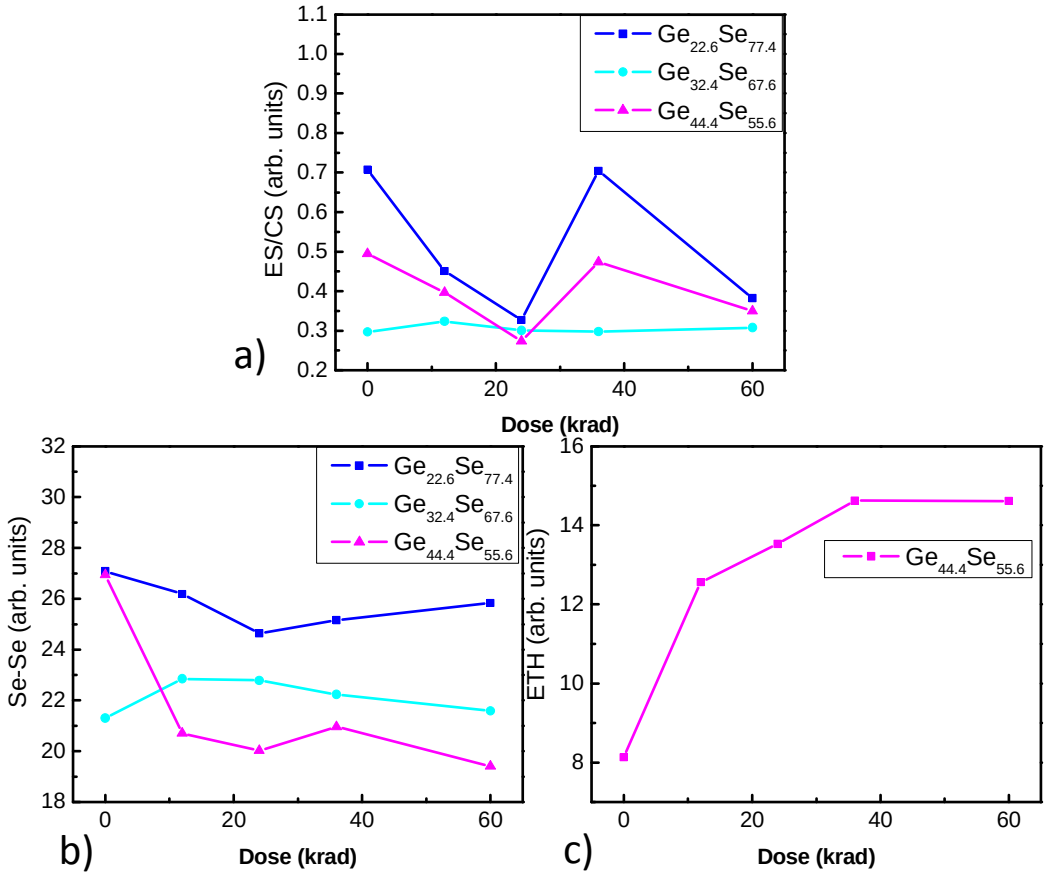

Figure 36. Areas of Gaussian curves fitted to Raman spectra: a) ratio of areas of ES curves to areas of CS curves, b) Areas of Se-Se band curves, and c) Areas of ETH band curves

The products of Ag diffusion in Ge_xSe_{100-x} (Ag_2Se and Ag_8GeSe_6) cannot be observed through Raman spectroscopy. Therefore, the presence of these compounds was detected by X-ray diffraction (XRD). XRD measurements provided information on the molecular compounds formed after Ag introduction. The XRD patterns of $Ge_{25.6}Se_{74.4}$, $Ge_{36.2}Se_{63.8}$, and $Ge_{44.3}Se_{55.7}$ films with a silver source are shown in Figure 37a, b, c, respectively. In the $Ge_{25.6}Se_{74.4}$ film, β-phase Ag_2Se was observed at 2θ=33° in the control sample as well as after 12 krad and 24 krad of x-ray exposure [85]. No changes were observed in the XRD pattern of $Ge_{36.2}Se_{63.8}$ film; however, in the $Ge_{44.3}Se_{55.7}$ film, formation of β-Ag_2Se was observed after 24 krad of x-ray exposure.

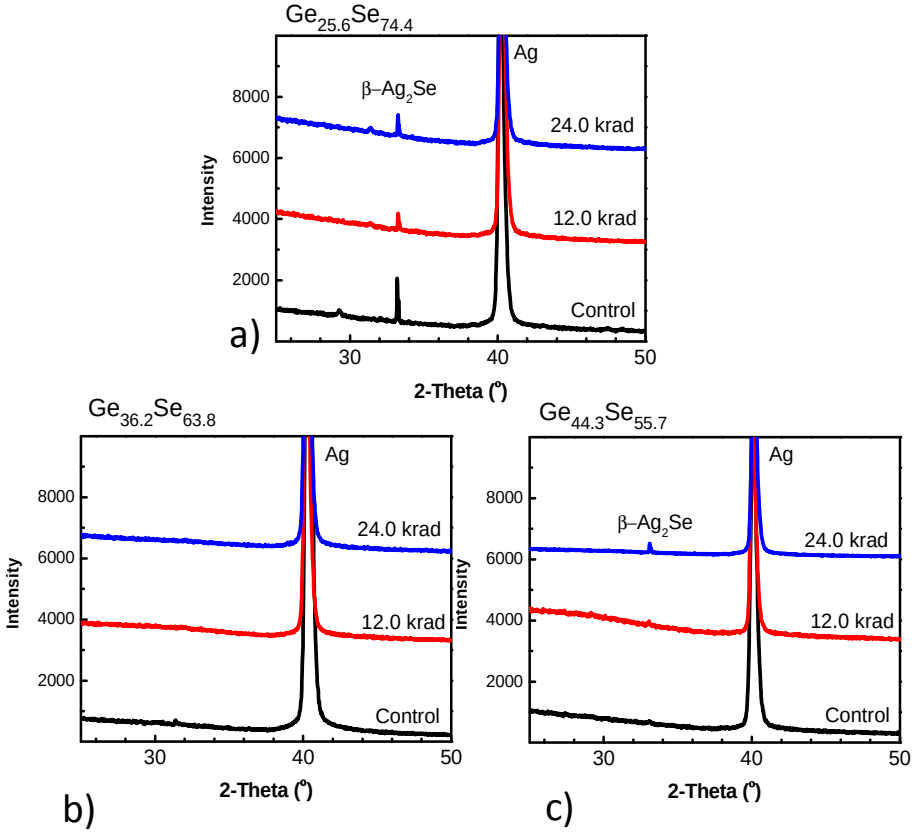

Figure 37. XRD patterns of films with Ag source exposed to x-rays show development of β-Ag_2Se a) $Ge_{25.6}Se_{74.4}$, b) $Ge_{36.2}Se_{63.8}$, and c) $Ge_{44.3}Se_{55.7}$

RCBM Device Performance

Redox Conductive Bridge Memory (RCBM) devices based on three different compositions of Ge_xSe_{100-x} (x=24.8, 36.2, and 44.3) were tested for their IV characteristics and endurance before and after x-ray exposure. Each device endured a minimum of 10^5 switching cycles. Figure 38 illustrates the cumulative distributions of the write voltage (V_{Th}), erase voltage (V_{Er}), On-State Resistance (LRS), and Off-State Resistance (HRS) for the three different composition devices before and after irradiation.

The general trend of the HRS values across all compositions appears to be decreasing with increasing Ge content. Across all dose exposures, the HRS values of the $Ge_{24.8}Se_{75.2}$ devices appeared to be the highest. Correspondingly, the $Ge_{24.8}Se_{75.2}$ devices also had the largest standard deviation in HRS, which can be seen by the wide distribution in Figure 38b. The V_{Th} across all compositions appear to be relatively close in values, with the exception of one outlier in $Ge_{36.2}Se_{63.8}$.

The median value of a cumulative distribution is the value at which the cumulative probability is 50%. Mostly non-linear changes were observed in the median V_{Th} of the devices with x-ray exposure. In the $Ge_{24.8}Se_{75.2}$ devices, V_{Th} changed from 0.75 V to 1.02 to 0.72 for the control, 12.0 krad, and 24.0 krad doses, respectively. Median V_{Th} in the $Ge_{36.2}Se_{63.8}$ devices originally increased from 0.24 V to 1.3 V after 12.0 krad exposure, then decreased back to 0.24 V after 24.0 krad of exposure.

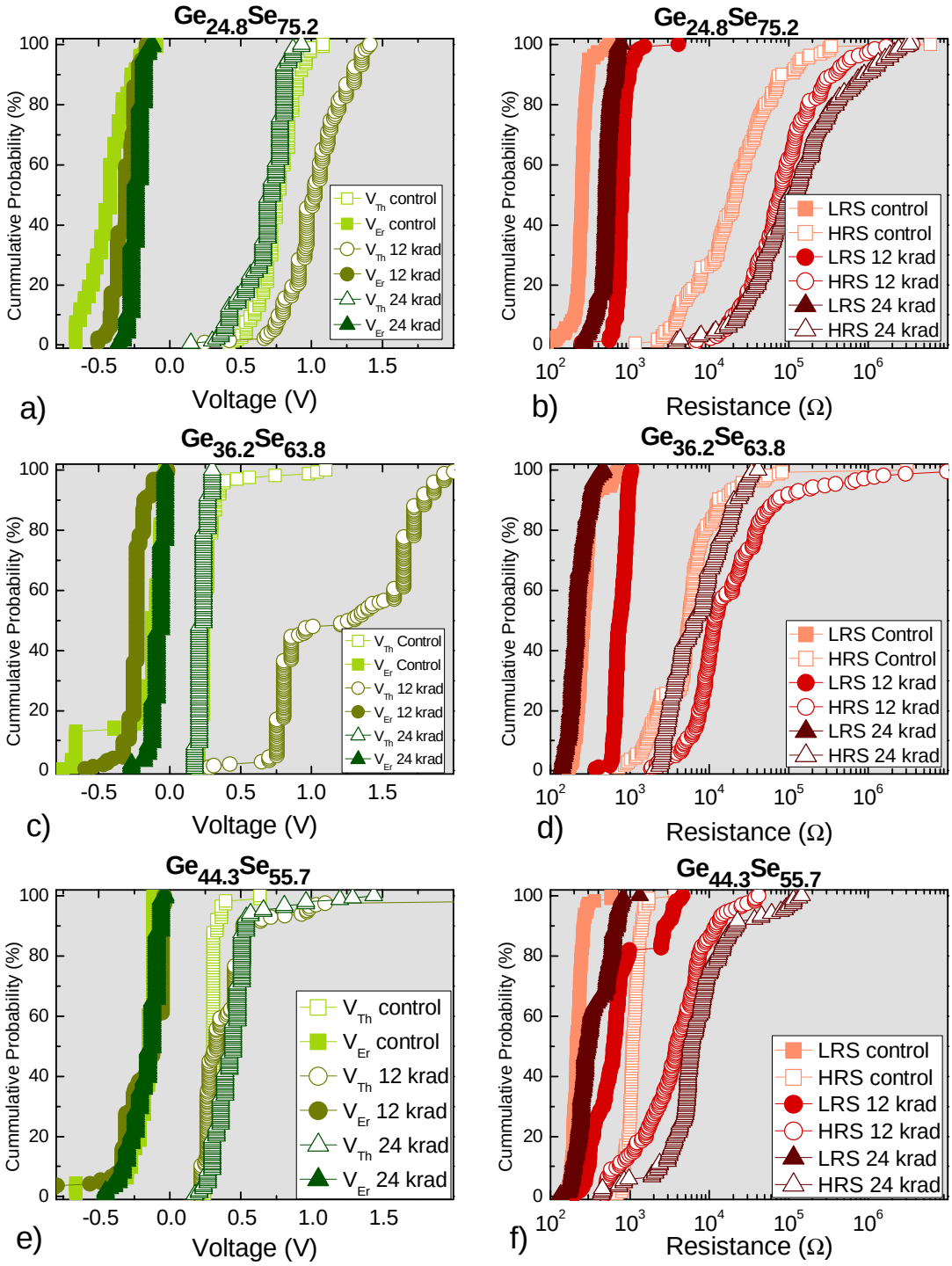

Figure 38. Distribution of write/erase voltages (green) and on/off-state resistances (red) for Ge_xSe_{100-x} (x=24.8, 36.2, and 44.3) RCBM devices exposed to 0, 12.0 krad, and 24.0 krad of x-rays

Since the changes in the V_{Th} from the control devices to both 12 krad and 24 krad exposed devices are less than 0.5 V and nonlinear with dose, variations in V_{Th} are also considered to result from differences inherent in the devices, rather than resulting from radiation exposure. One device with composition of $Ge_{36.2}Se_{63.8}$ (12 krad) demonstrated a much larger V_{Th} relative to all other devices in the same composition as well as in the other compositions. This large difference in V_{Th} is considered to be an artifact of variations in the device fabrication process.

Looking more closely at changes observed in each composition with x-ray exposure, the performances of $Ge_{24.8}Se_{75.2}$ and $Ge_{44.3}Se_{55.7}$ based RCBM devices both demonstrated an increase in the median HRS from the control dose, 0 krad, to 12.0 krad. The median HRS of $Ge_{24.8}Se_{75.2}$ devices increased from $2.13x10^4$ Ω to $7.78x10^4$ Ω (Figure 38b), and that of the $Ge_{44.3}Se_{55.7}$ devices increased from $1.08x10^3$ Ω to $3.84x10^3$ Ω (Figure 38f), after 12.0 krad of irradiation. The $Ge_{24.8}Se_{75.2}$ and $Ge_{44.3}Se_{55.7}$ devices also demonstrated a further, albeit small, increase in the median HRS values to $1.13x10^5$ Ω and $5.91x10^3$ Ω, respectively.

The memory window of a RCBM device is the difference in resistance between HRS and LRS. The median memory windows for each device, corresponding to the exposure dose, are presented in Figure 39. The $Ge_{24.8}Se_{75.2}$ devices demonstrated the largest memory before irradiation, as well as the largest increase after irradiation. The memory windows of $Ge_{44.3}Se_{55.7}$ devices also demonstrated a linear increase with irradiation, while that of the $Ge_{36.2}Se_{63.8}$ devices appeared to remain relatively constant.

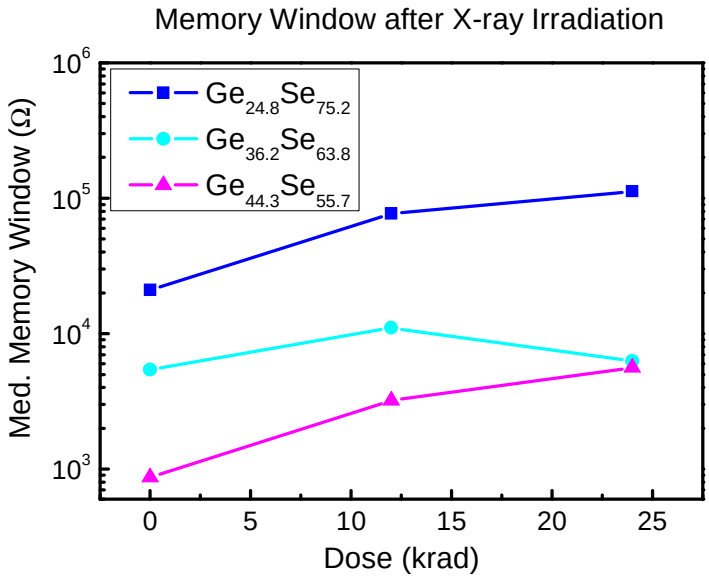

Figure 39. Median memory windows for RCBM devices exposed to x-rays

The endurance performance data (i.e., V_{Th}, V_{Er}, LRS, and HRS) after various switching cycles, ranging from 10^0-10^5, of the $Ge_{24.8}Se_{75.2}$ devices after 0, 12, and 24 krad x-ray exposure are shown in Figure 40. The same data for $Ge_{36.2}Se_{63.8}$ devices and $Ge_{44.3}Se_{55.7}$ devices are shown in

Figure 41 and

Figure 42, respectively. The inset of each graph provides the same data (i.e., V_{th} and V_{Er} or LRS and HRS) after 10^5 switching cycles. These graphs demonstrate that all compositions of devices were able to function at least 10^5 switching cycles. After 12 krad and 24 krad of x-ray exposure, all compositions of the RCBM devices maintained an endurance of 10^5 switching cycles.

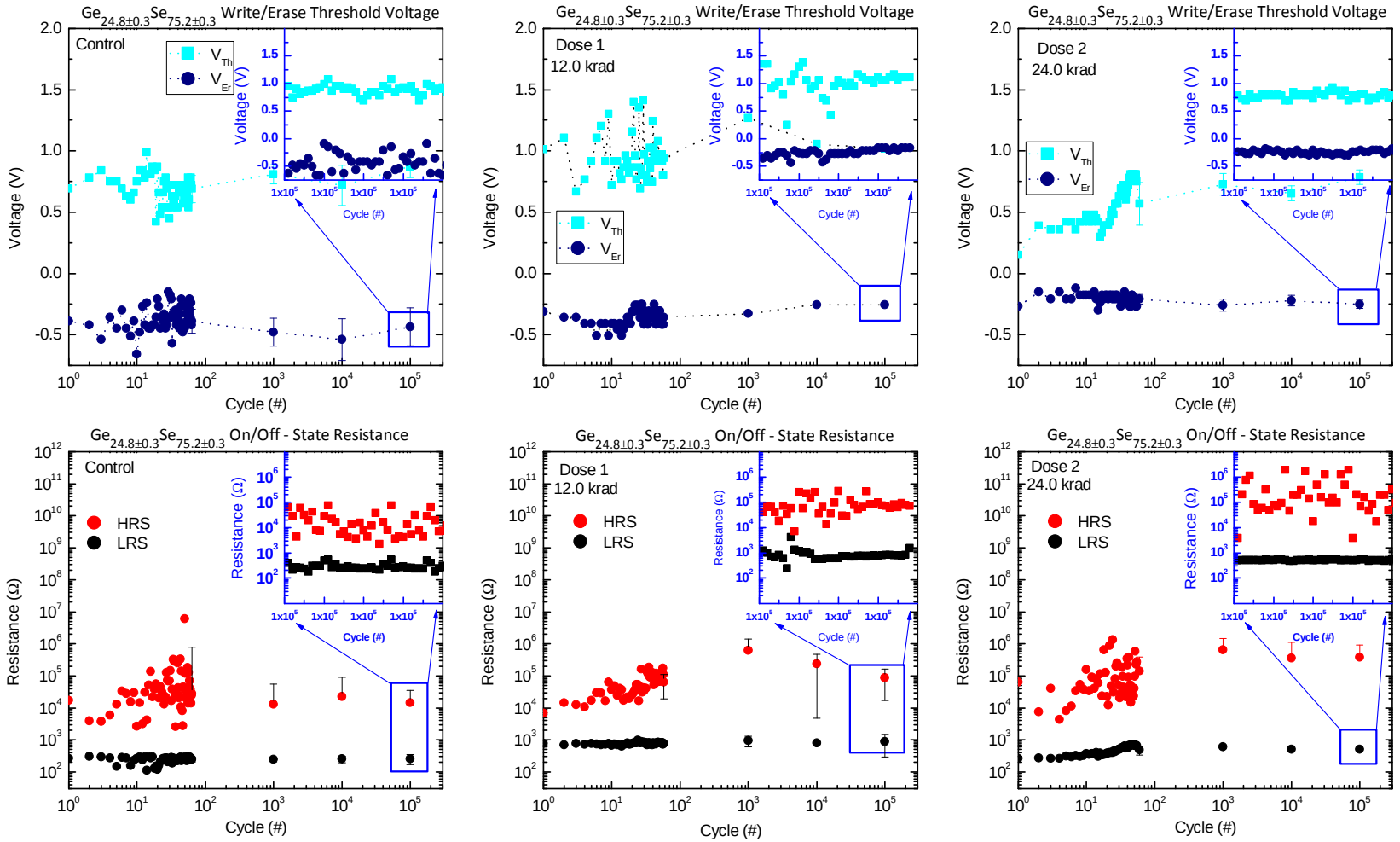

Figure 40. Endurance testing data for 10^5 cycles on $Ge_{24.8}Se_{75.2}$ RCBM devices exposed to 0, 12 krad, and 24 krad of x-rays

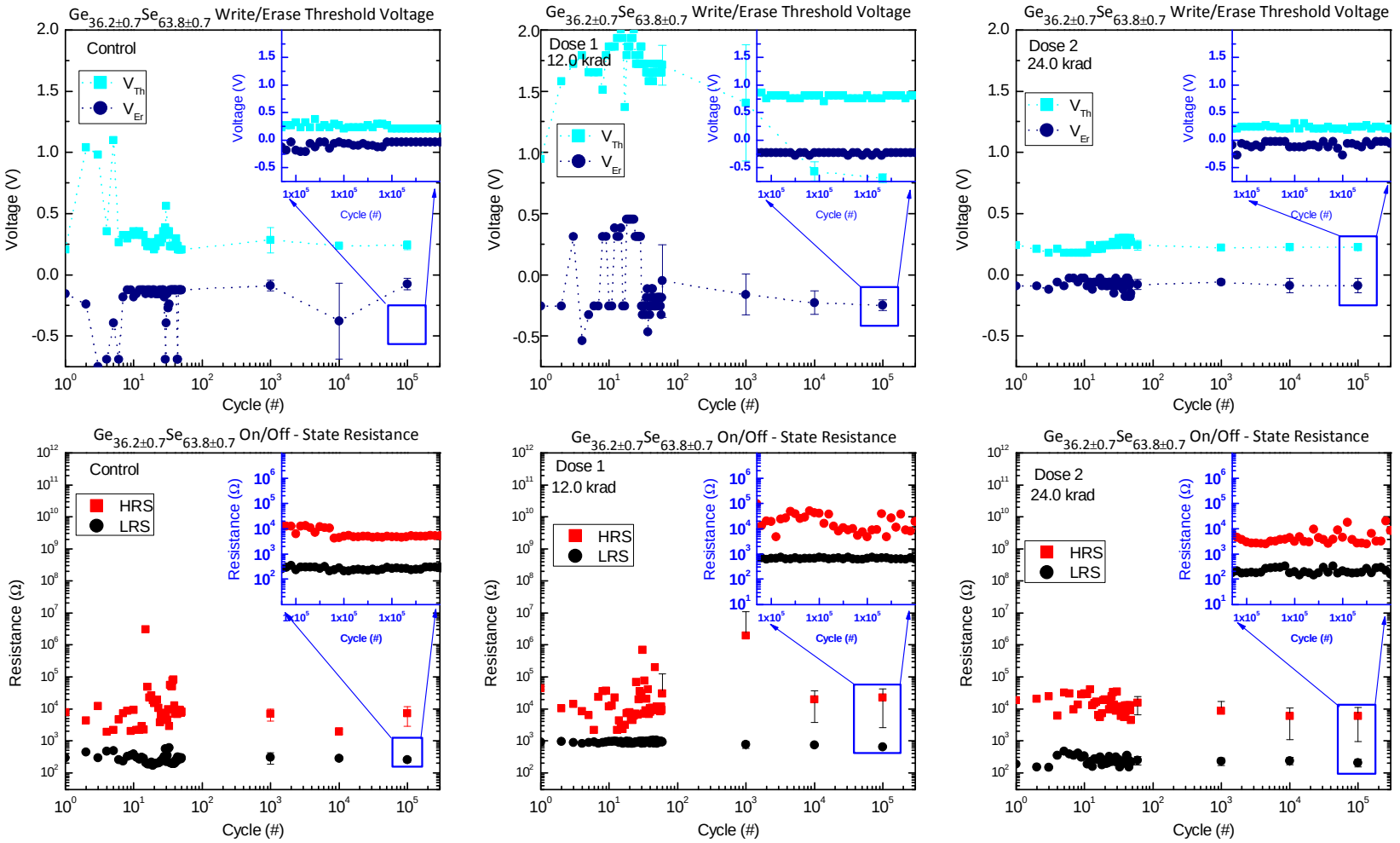

Figure 41. Endurance testing data for 10^5 cycles on $Ge_{36.2}Se_{63.8}$ RCBM devices exposed to 0, 12 krad, and 24 krad of x-rays

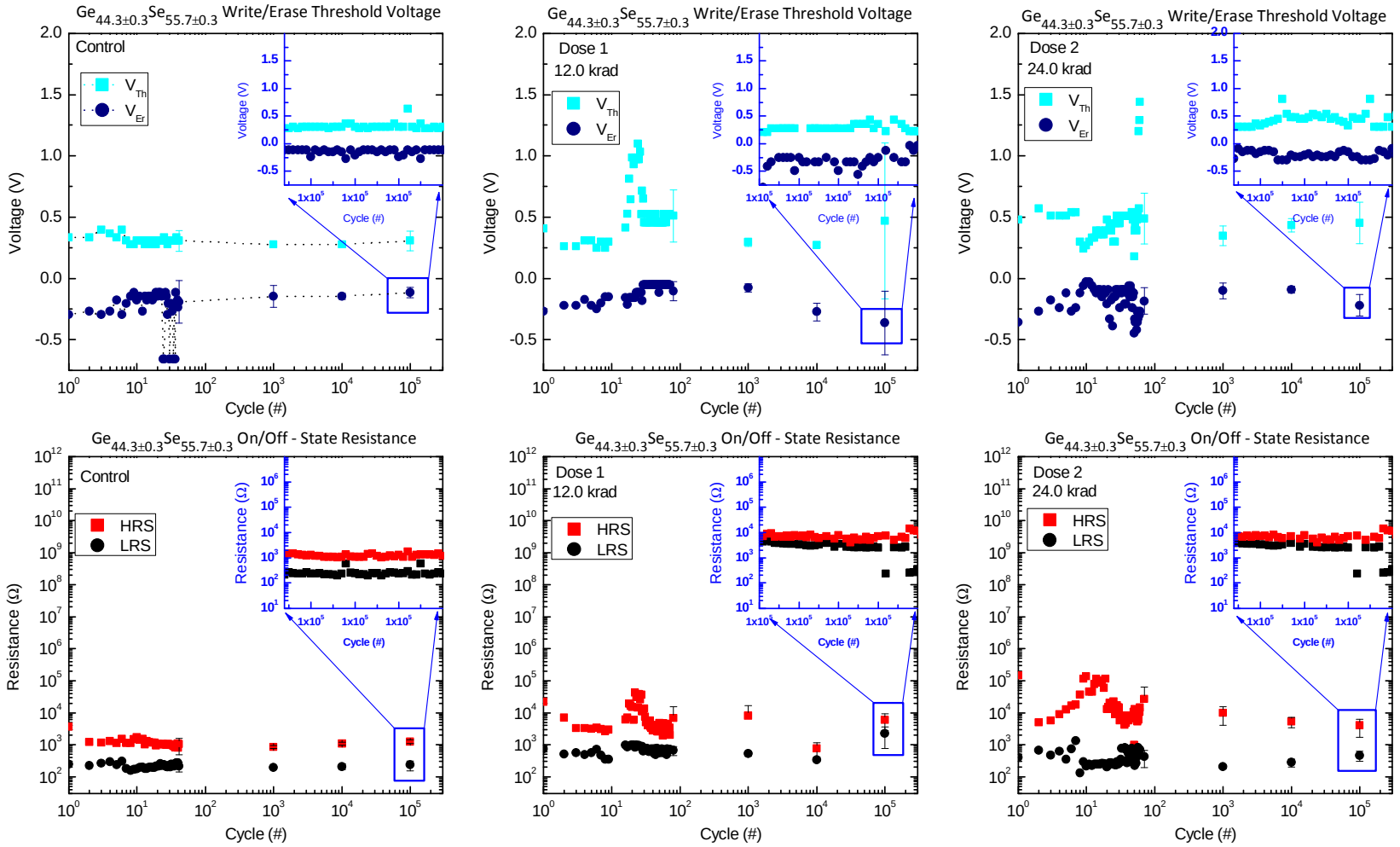

Figure 42. Endurance testing data for 105 cycles on Ge44.3Se55.7 RCBM devices exposed to 0, 12 krad, and 24 krad of x-rays

Discussion

Raman spectroscopy studies on $Ge_{22.6}Se_{77.4}$ bare films reveal substantial structural rearrangements in the form of decreased ES/CS area ratios, between 0 to 24.0 krad (Figure 36a). A decreased ES/CS ratio indicates the conversion from ES to CS structures, ergo the collapse of voids within the structural network, as seen in Figure 43. Density of the amorphous material increases with the reduction of these voids, thereby enhancing the material's ability to resist leakage current. This in turn, will increase the HRS of the device, since the off-state resistance and the leakage current are inversely proportional. The formation of CS structures, which requires one more Se atom than ES structures, within the network is supported by the decreasing amount of Se-Se chains observed between 0 and 24.0 krad.

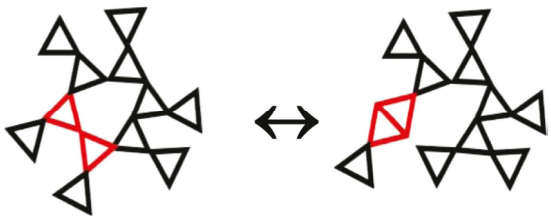

Figure 43. Conversion of ES to CS structures within the Ge-Se network Reprinted with permission from[86] © 2011 American Chemical Society

XRD measurements on films of composition $Ge_{25.6}Se_{74.4}$ adjacent to a Ag source reveal the presence of β-Ag_2Se in the control and x-ray exposed samples. The presence of β-Ag_2Se in the control sample is due to the low packing fraction of the structural network, in addition to the affinity of Ag atoms to the Se chains. A previous study found the packing fraction $Ge_{25.6}Se_{74.4}$ to be relatively low compared to that of $Ge_{35.6}Se_{63.8}$, as can be seen in Figure 44. Therefore, during the deposition process, the energetic Ag

atoms can easily diffuse through the $Ge_{25.6}Se_{74.4}$ matrix and bond with the abundantly available Se atoms forming β-Ag_2Se.

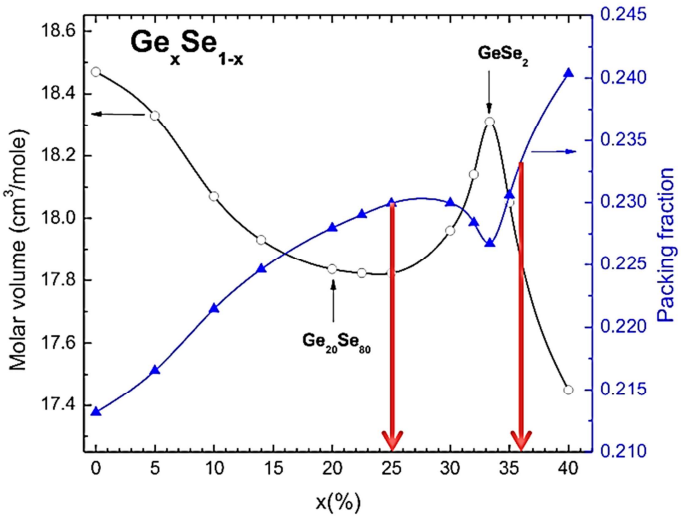

Figure 44. Packing fraction of Ge_xSe_{100-x}

The structural changes observed from the Raman data indicate a destruction of voids and an increase in the density of the network. These structural changes limit the growth of β-Ag_2Se crystals, which is supported by the decreasing intensity of the peak in the XRD data of Figure 37a. Decreased β-Ag_2Se crystal sizes, in combination with the destruction of voids within the network, led to increased HRS values in the RCBM devices, which is seen in Figure 38b.

In the $Ge_{32.4}Se_{67.6}$ films, no significant structural changes were observed from the Raman spectra. The ES/CS ratio remained relatively constant, averaging at 0.3 (arbitrary units). The lack of structural changes observed is attributed to the film composition, $Ge_{32.4}Se_{67.6}$, which is in close proximity to the stoichiometric composition (i.e., $GeSe_{4/2}$). In these films, the heteropolar bonds, which are stronger than homopolar bonds, are abundant and nearly saturated. Furthermore, XRD patterns (Figure 37b) of the

$Ge_{36.2}Se_{63.8}$ films with an Ag source showed no development in Ag containing compounds, which is justified by the limited amount of free Se chains. In addition, the packing fraction of $Ge_{36.2}Se_{63.8}$ is relatively high (Figure 44), which also limited the amount of Ag diffusion in the films.

Considering the results obtained through Raman spectroscopy and XRD, the radiation-induced changes in $Ge_{36.2}Se_{63.8}$ devices are expected to be minimal. Indeed, minimal changes were observed in the $Ge_{36.2}Se_{63.8}$ devices. The HRS increased initially, from $5.70x10^3$ Ω in the control device, to $1.17x10^4$ Ω in the 12.0 krad exposed device. The $Ge_{36.2}Se_{63.8}$ device exposed to 24.0 krad of x-rays demonstrated an HRS value of $6.47x10^3$ Ω, which is closer to the control than the 12.0 krad device. Therefore, the observed changes are attributed to variations in the fabrication process rather than the radiation.

Similar to the bare films studies on $Ge_{22.6}Se_{77.4}$, films of $Ge_{44.4}Se_{55.6}$ composition demonstrated a decreased ES/CS ratio, in the dose range from 0 to 24.0 krad. As described previously, decreases in the ES/CS ratio implies conversions from ES structures to CS structures and collapse of voids in the network. XRD patterns on $Ge_{44.3}Se_{55.7}$ films illustrate the emergence of the β-Ag_2Se phase after 24.0 krad. Analogous to the XRD results on $Ge_{25.6}Se_{74.4}$ films, the development of the β-Ag_2Se phase was hindered by the structural rearrangements. Similar to the $Ge_{24.8}Se_{75.2}$ devices, $Ge_{44.3}Se_{55.7}$ devices demonstrated increased HRS after 12.0 and 24.0 krad radiation. The increased HRS is attributed to the structural changes that caused the film to be more resistant to leakage current.

Conclusion

High energy x-ray photons affect the a-Ge_xSe_{100-x} films and therefore a-Ge_xSe_{100-x} based RCBM devices in different manners depending on the film compositions. Films and devices based on the stoichiometric composition of $GeSe_{4/2}$ exhibited minimal changes. Devices and films largely deviating from the stoichiometric composition, either Se rich or Se deficient, exhibited changes due to irradiation. The films revealed decreases in the voids of the network, which suppressed diffusion in the chalcogenide matrix. Therefore, the devices deviating from the stoichiometric composition demonstrated increased resistance, and as a result of this increased memory window, with x-ray exposure.

CHAPTER 8: ELECTRON BEAM INDUCED EFFECTS IN THIN Ge-Se FILMS AND RCBM DEVICES

The effect of directly ionizing radiation was studied by observing the influence of electron beam radiation on a-Ge_xSe_{100-x} thin films. The results of these studies were used to interpret the changes in performance of RCBM devices.

Radiation Exposure Conditions

Irradiation experiments were conducted using a LEO 1430VP Scanning Electron Microscope as an electron beam source. A voltage bias was applied across a tungsten filament, which generated a large number of electrons that passed through an electric field with an accelerating voltage of 30 kV. This stream of electrons was adjusted using beam aligners and apertures creating a beam current of 1 nA directed at the films and devices. These thin films and devices were placed 20 mm from the base of the stage where the electron beam diameter was 1.3 mm. Application of these various settings generated an electron flux of 2.496 x 10^{14} electrons per second. An image of the electron irradiator is shown in Figure 45.

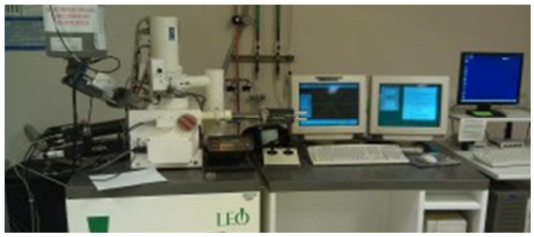

Figure 45. Electron beam radiation system

Film Characterization

Structural changes due to electron beam (e-beam) irradiation on a-Ge_xSe_{100-x} films (x= 22.6, 26.1, 32.4, 42.2, as determined by EDS) were studied using Raman spectroscopy. Raman spectra are presented in Figure 46. From the Raman spectra, four characteristic structural units are observed: ethane-like bonding (ETH) structures average vibrational mode at 176 cm^{-1}, corner-sharing (CS) tetrahedral structures average vibrational mode at 198 cm^{-1}, edge-sharing (ES) tetrahedral structures at 215 cm^{-1} [73-76], and Se-Se chains and rings are present at 280 cm^{-1} [77, 78], and the final band that is observed in the Raman spectra is attributed to the asymmetric average vibration of the edge-shared tetrahedral at 308 cm^{-1} [78-80].

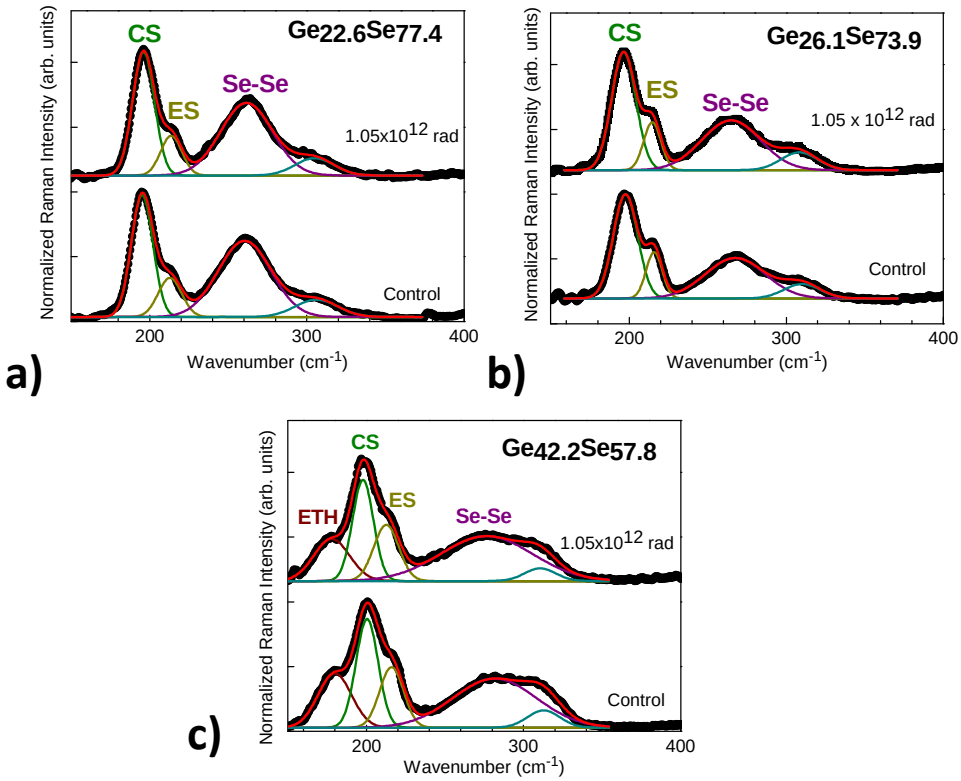

Figure 46. Deconvoluted Raman spectra of a) $Ge_{22.6}Se_{77.4}$, b) $Ge_{26.1}Se_{73.9}$, and c) $Ge_{42.2}Se_{57.8}$ exposed to 0 and 1.05x10^{12} rad of e-beam radiation

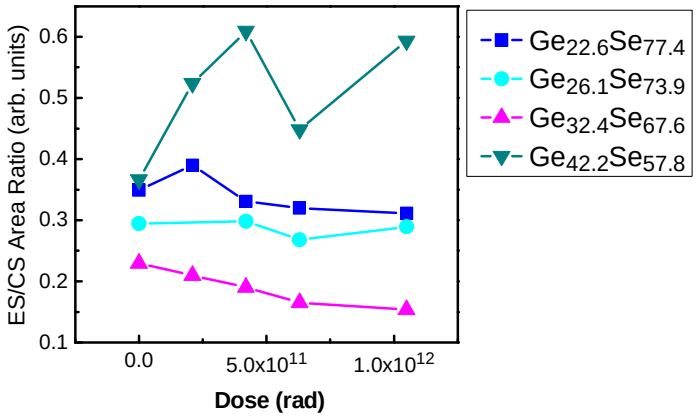

Figure 47. Area ratio of ES/CS from deconvoluted Raman spectra

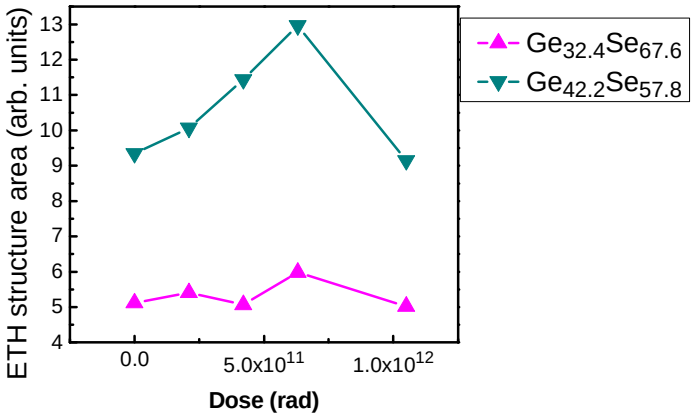

Figure 48. Area of ETH from deconvoluted Raman spectra

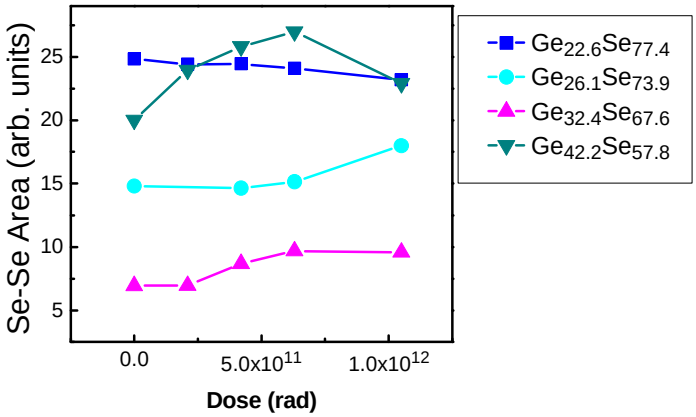

Figure 49. Area of Se-Se curve from deconvoluted Raman spectra

Analysis of the areal intensity of the various peaks corresponding to the different structural units reveals a unique trend as a function of e-beam exposure. The graph of the

ratio ES to CS structures (ES/CS), shown in Figure 47, reveals a local minimum for each composition film. This local minimum is most pronounced in the $Ge_{42.2}Se_{57.8}$ film. Ethane-like structures were only detected in the higher Ge-content films $Ge_{32.4}Se_{67.6}$ and $Ge_{42.2}Se_{57.8}$ [73, 87, 88]. In both of these compositions, a general increase in the amount of ETH structures, as illustrated in Figure 48, was observed with increasing e-beam dose until a critical dose of $6.3x10^{11}$ rad, where a decrease in the amount of ETH structures was observed. From Figure 49, the amount of Se-Se chains increases, reaching a maximum at $6.3x10^{11}$ rad, followed by a decrease. Similar trends in the vibrational bands of Se-Se chains were observed in the other films. However, in these films, the maximum of these chains shifts to higher radiation doses with decreasing Ge-content.

Lateral Ag diffusion in a-Ge_xSe_{100-x} films containing silver sources exposed to different e-beam radiation doses were measured by EDS mapping. The total diffusion distance of Ag, as determined through EDS mapping data, for each composition is summarized in Figure 50. The largest Ag diffusion was observed in $Ge_{25.6}Se_{74.4.}$ In the range of the studied exposure doses, $Ge_{25.6}Se_{74.4}$ and $Ge_{36.2}Se_{63.8}$ demonstrate a nearly linear relationship between the diffusion distance and the radiation dose. In the $Ge_{44.3}Se_{55.7}$ sample, Ag diffusion was observed for the entire radiation dose range studied; however, the rate of Ag diffusion decreases at the critical dose of $6.3x10^{11}$ rad, indicating Ag saturation.

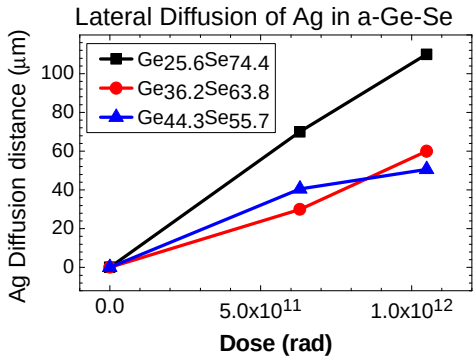

Figure 50. Lateral diffusion of Ag as determined through EDS mapping

Results of the EDS mapping of $Ge_{25.6}Se_{74.4}$ are shown in Figure 51 a, b, and c. Similarly, the results for $Ge_{36.2}Se_{63.8}$ and $Ge_{44.3}Se_{55.7}$ are summarized in Figure 52a, b, and c, and Figure 53 a, b, and c, respectively. The color scale below the map describes the counts received by detector. The yellow and orange colors indicate the highest counts of silver, suggesting a large quantity of silver atoms at the specific location while black indicates the lowest amount of counts, which signifies the inexistence of silver atoms.

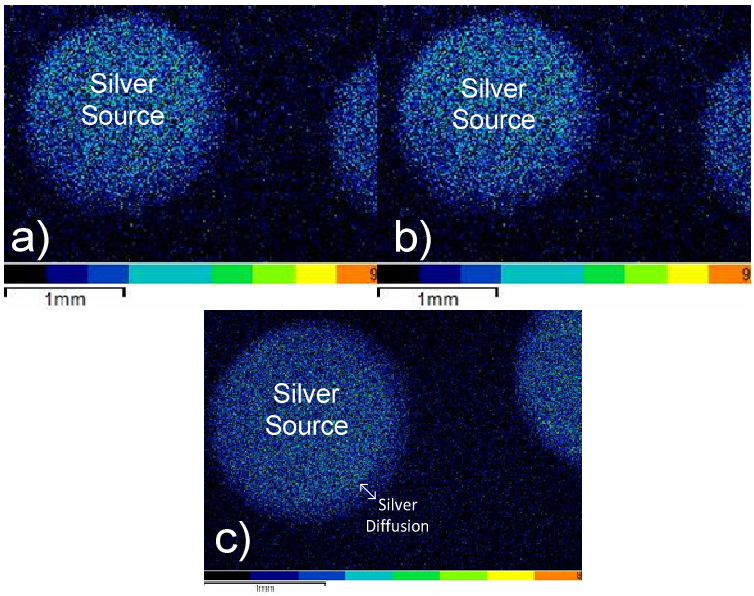

Figure 51. EDS mapping of Ag diffusion in a-$Ge_{25.6}Se_{74.4}$ a) Control, b) 6.3x10^{11} rad, and c) 10.5x10^{11} rad

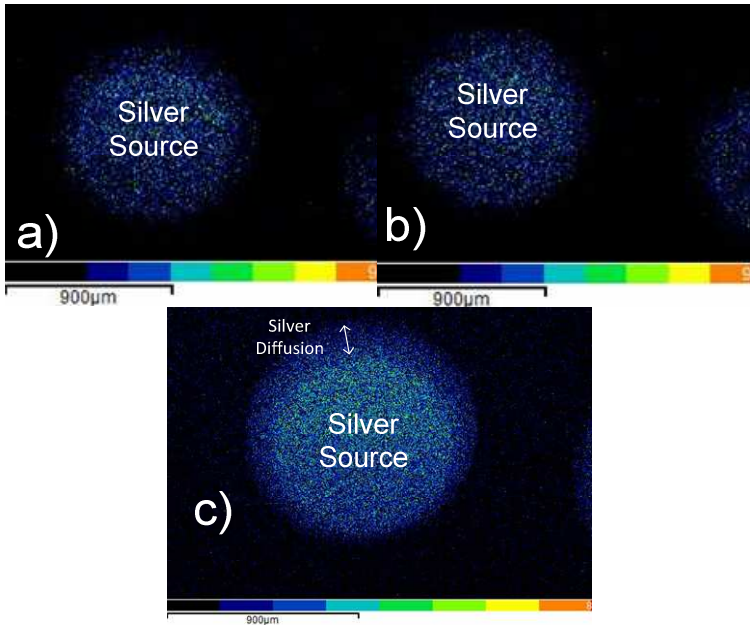

Figure 52. EDS mapping of Ag diffusion in a-$Ge_{36.2}Se_{63.8}$ a) Control, b) 6.3x10^{11} rad, and c) 10.5x10^{11} rad

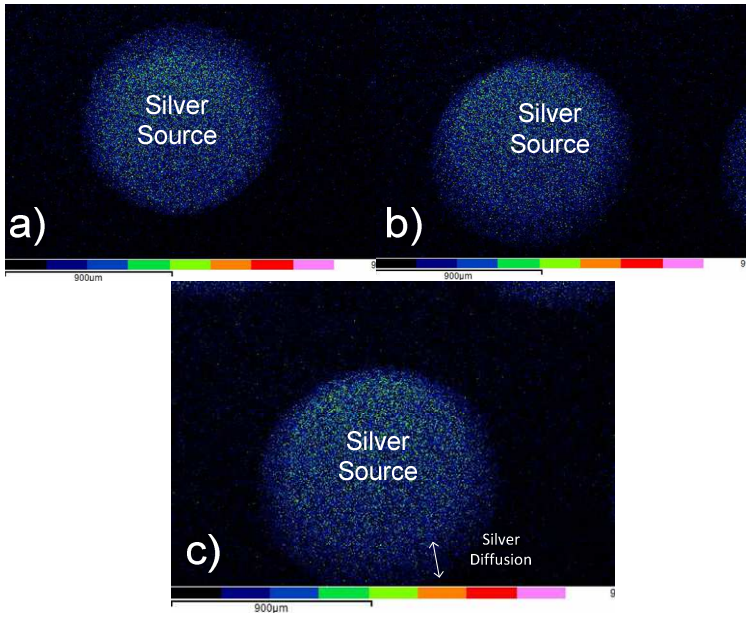

Figure 53. EDS mapping of Ag diffusion in a-$Ge_{44.3}Se_{55.7}$ a) Control, b) 6.3x10^{11} rad, and c) 10.5x10^{11} rad

The XRD patterns are presented in Figure 54, Figure 55, and Figure 56 for $Ge_{25.6}Se_{74.4}$, $Ge_{36.2}Se_{63.8}$, and $Ge_{44.3}Se_{55.7}$, respectively. In each of the three compositions,

the phase growth of both the α-Ag_2Se and Ag_8GeSe_6 phases was observed, as illustrated in Figure 57 and Figure 58, respectively. The α-Ag_2Se phase was observed at 2θ = 38° angle [85] and the Ag_8GeSe_6 phase was observed at 2θ = 44°, which is identified by JCPDS card 71-190.

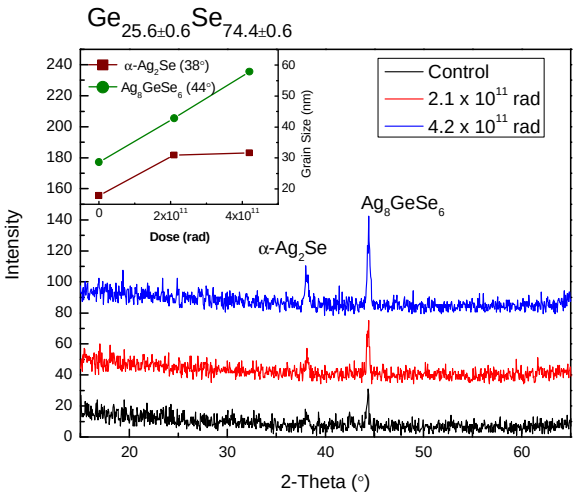

Figure 54. XRD pattern of e-beam radiated $Ge_{25.6}Se_{74.4}$ with Ag source

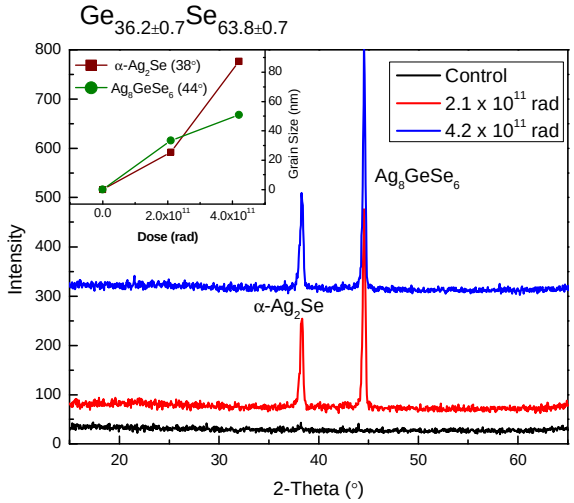

Figure 55. XRD pattern of e-beam radiated $Ge_{36.2}Se_{63.8}$ with Ag Source

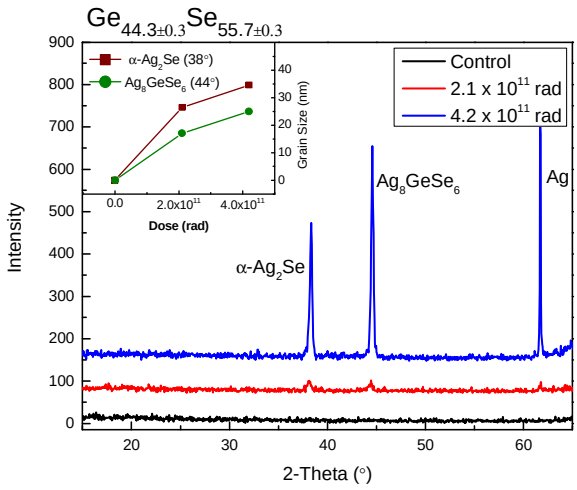

Figure 56. XRD pattern of e-beam radiated $Ge_{44.3}Se_{55.7}$ with Ag source

From the XRD pattern, the grain size of each phase was determined using the Debye Scherrer equation (11) [89].

$$L = \frac{K\lambda}{B\cos(\theta)} \qquad (11)$$

where L is the crystal size in nm, K is a shape factor that depends on the crystal structure, for cubic K=0.94), λ is the wavelength of the x-rays (for Cu-K_α λ=0.1506 nm), B is the full width at half the maximum of the peak in radians, and θ is the intensity of the peak. In addition to these two phases, a third phase of pure phase separated Ag is observed in $Ge_{44.3}Se_{55.7}$ at 2θ=61°, identified by JCPDS card 87-0598. Significant growth in the phase separated Ag was observed with increasing radiation dose.

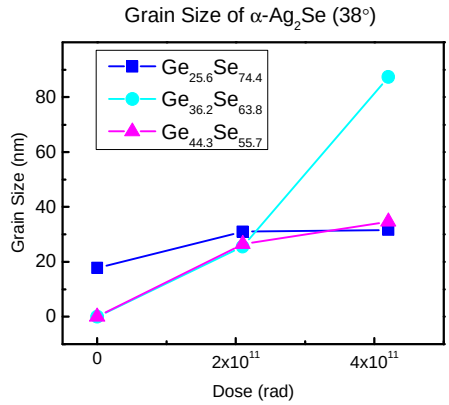

Figure 57. Phase growth of superionic conducting α-Ag_2Se phase in three different compositions

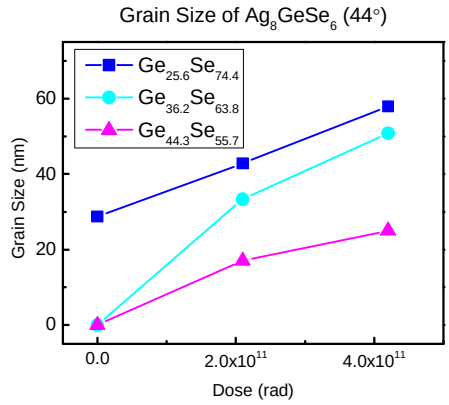

Figure 58. Grain growth of ternary Ag_8GeSe_6 phase in three different compositions

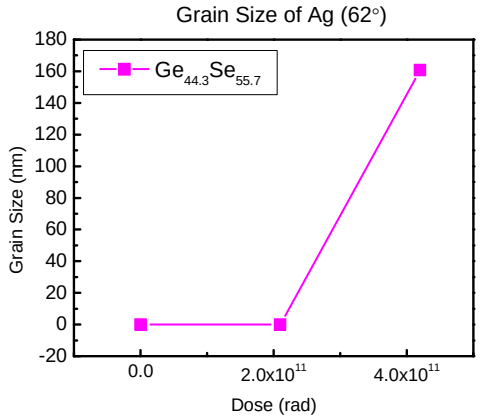

Figure 59. Grain growth in phase separated Ag in $Ge_{44.3}Se_{56.7}$

RCBM Device Performance

RCBM devices based of three different compositions of Ge_xSe_{100-x} (x=24.8, 36.2, and 44.3) were tested for their IV characteristics and endurance before and after e-beam exposure. Each device endured a minimum of 10^5 switching cycles. The cumulative distributions of V_{Th}, V_{Er}, LRS, and HRS for all compositions of devices are summarized in Figure 60.

The endurance performance data (i.e., V_{Th}, V_{Er}, LRS, and HRS) after various switching cycles, ranging from 10^0-10^5, of the $Ge_{24.8}Se_{75.2}$ devices after 0, $2.1x10^{11}$ rad (Dose 1), and $4.2x10^{11}$ rad (Dose 2) e-beam exposure are presented in Figure 61. The same data for $Ge_{36.2}Se_{63.8}$ devices and $Ge_{44.3}Se_{55.7}$ devices are shown in Figure 62 and Figure 63, respectively. The inset of each graph provides the same data (i.e., V_{th} and V_{Er} or LRS and HRS) after 10^5 switching cycles.

The median HRS values of $Ge_{24.8}Se_{75.2}$ originally show a miniscule decrease from the control device ($28.3x10^3$ Ω) to the Dose 1 device ($15.5x10^3$ Ω), followed by a substantial increase ($82.7x10^3$ Ω) in the Dose 2 device. Similarly, the $Ge_{36.2}Se_{63.8}$ device also reveals an initial decrease in HRS from the control device ($31.8x10^3$ Ω) to the Dose 1 device ($2.05x10^3$ Ω), followed by a small increase in the Dose 2 device ($4.50x10^3$). On the other hand, the HRS values for the $Ge_{44.3}Se_{55.7}$ devices increase consistently. The HRS values of $Ge_{44.3}Se_{55.7}$ devices are $1.07x10^3$ Ω, $1.96 x10^3$ Ω, and $23.1 x10^3$ Ω for the control, Dose 1, and Dose 2 devices, respectively.

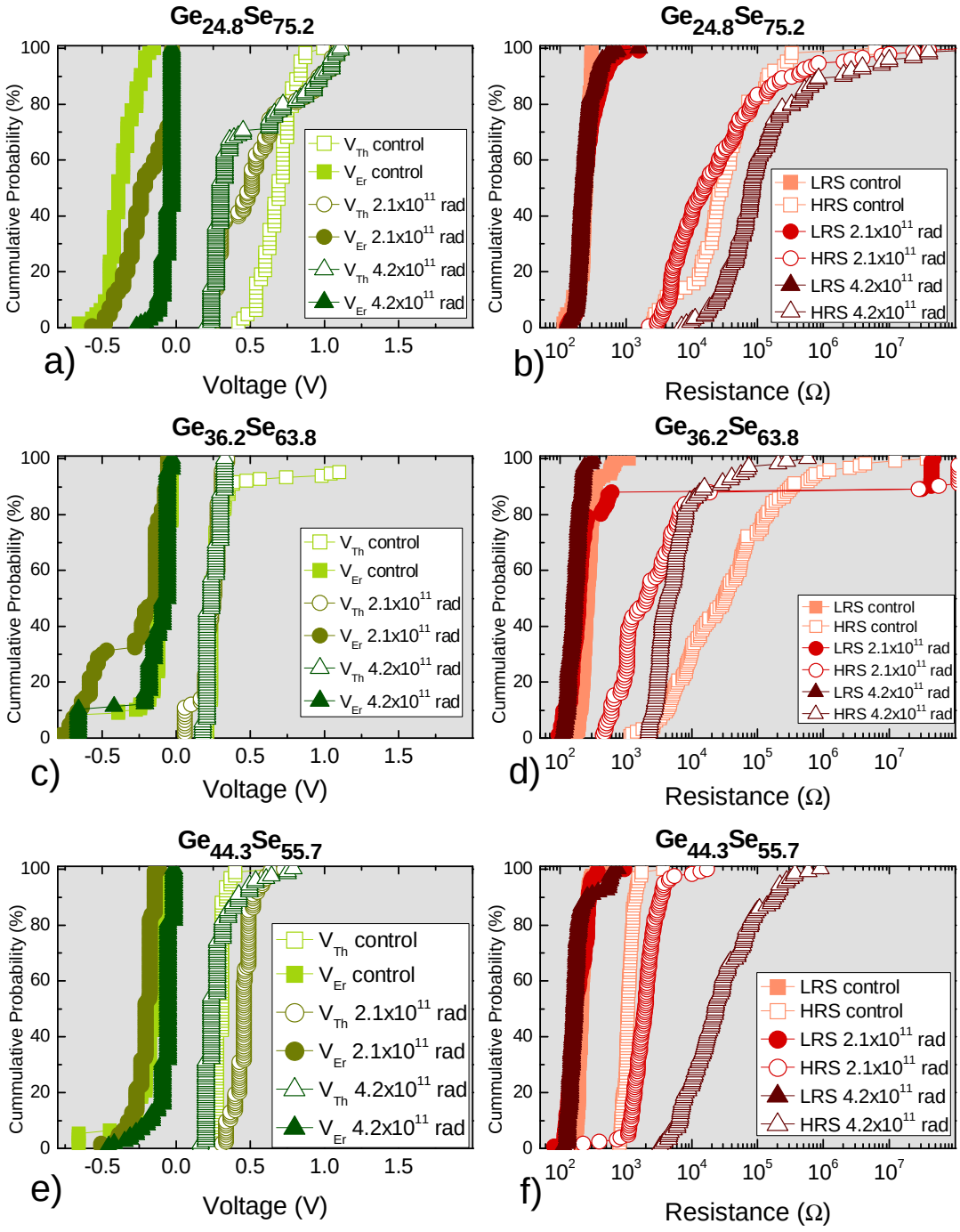

Figure 60. Distribution of write/erase voltages (green) and on/off-state resistances (red) for Ge_xSe_{100-x} (x=24.8, 36.2, and 44.3) RCBM devices exposed to 0, $2.1x10^{11}$, and $4.2x10^{11}$ rad of electron beam radiation

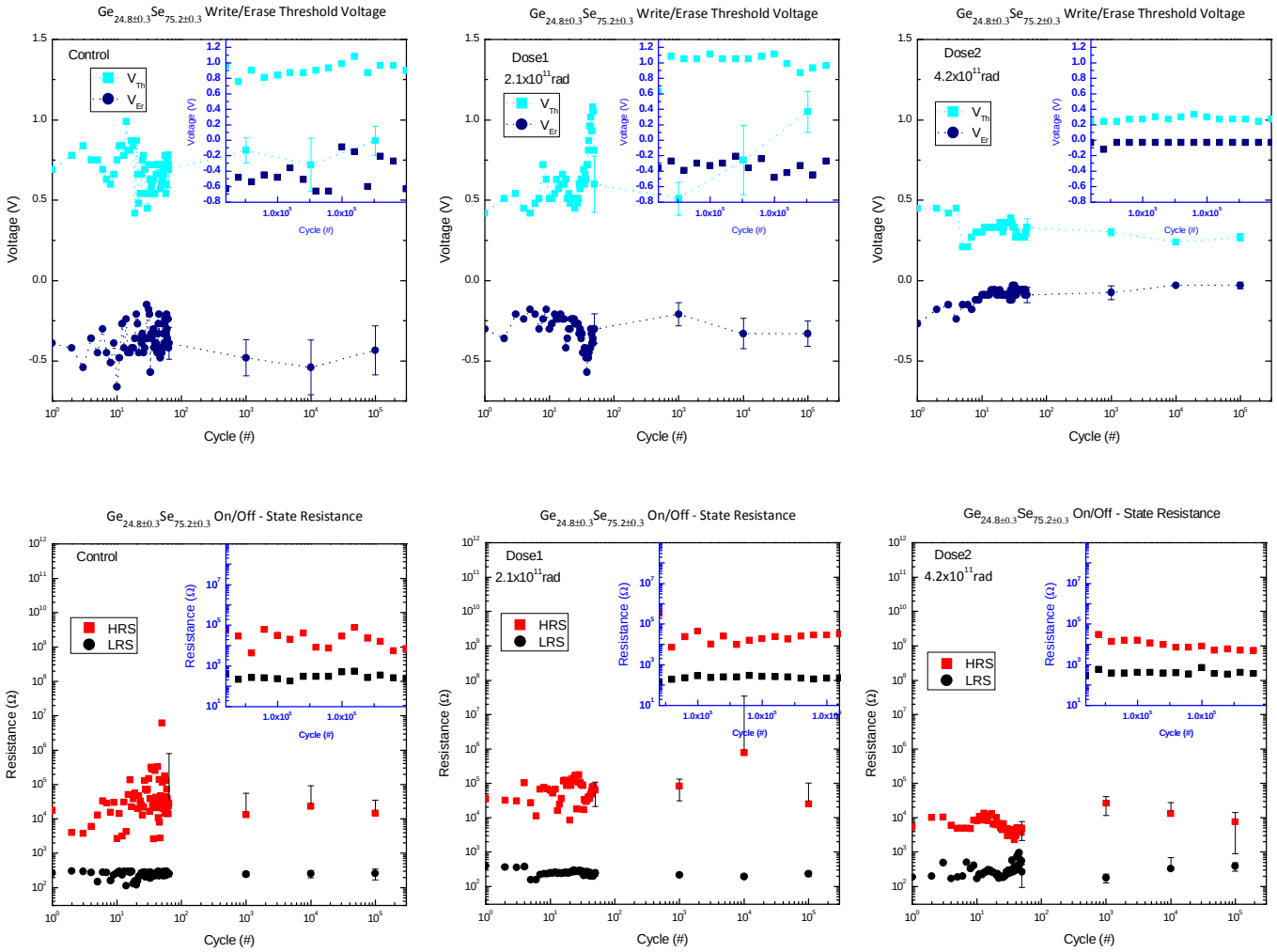

Figure 61. Endurance testing on $Ge_{24.8}Se_{75.2}$ RCBM devices exposed to 0 rad, $2.1x10^{11}$ rad, and $4.2x10^{11}$ rad of e-beam radiation

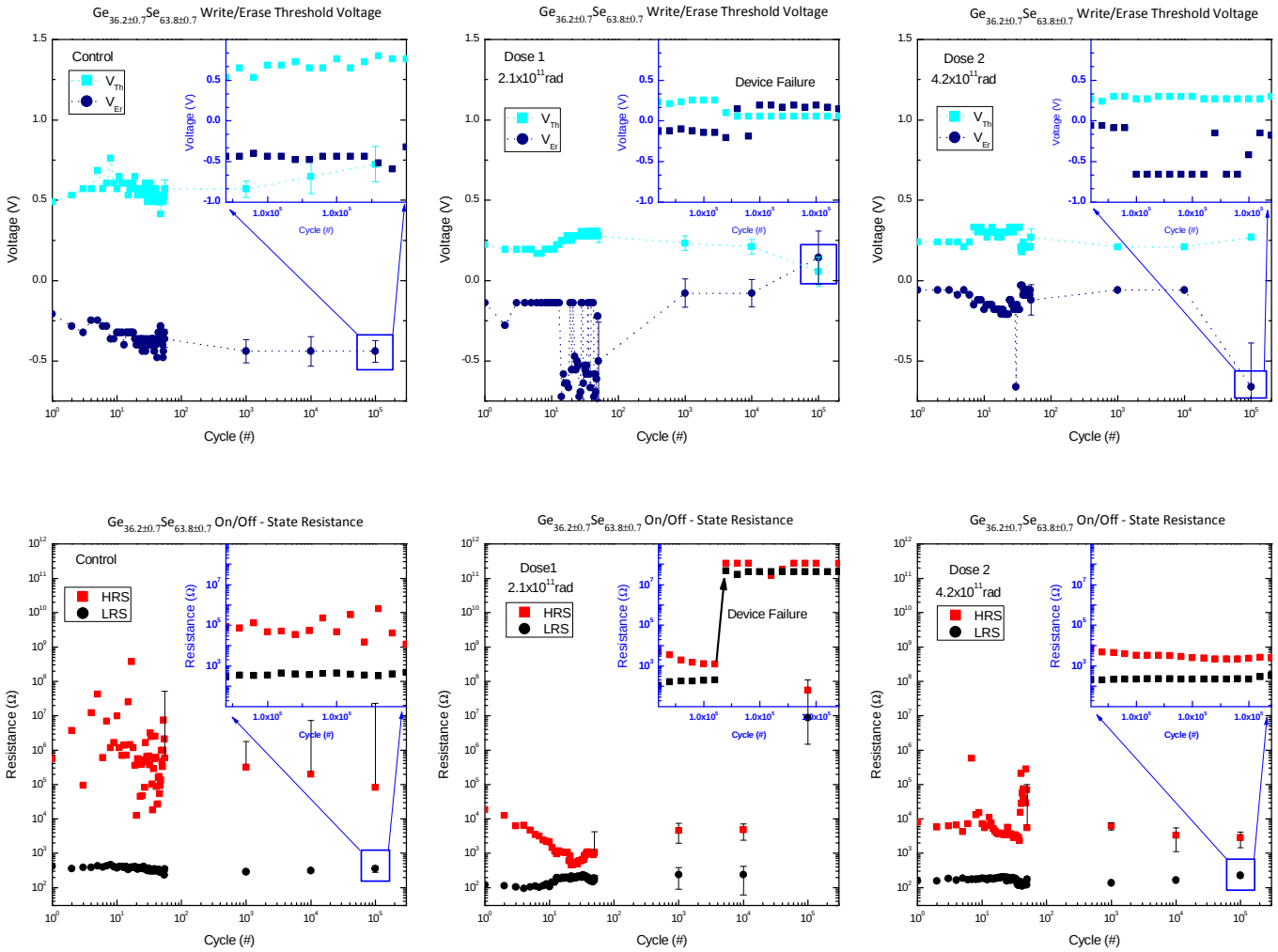

Figure 62. Endurance testing on $Ge_{36.2}Se_{63.8}$ RCBM devices exposed to 0 rad, $2.1x10^{11}$ rad, and $4.2x10^{11}$ rad of e-beam radiation

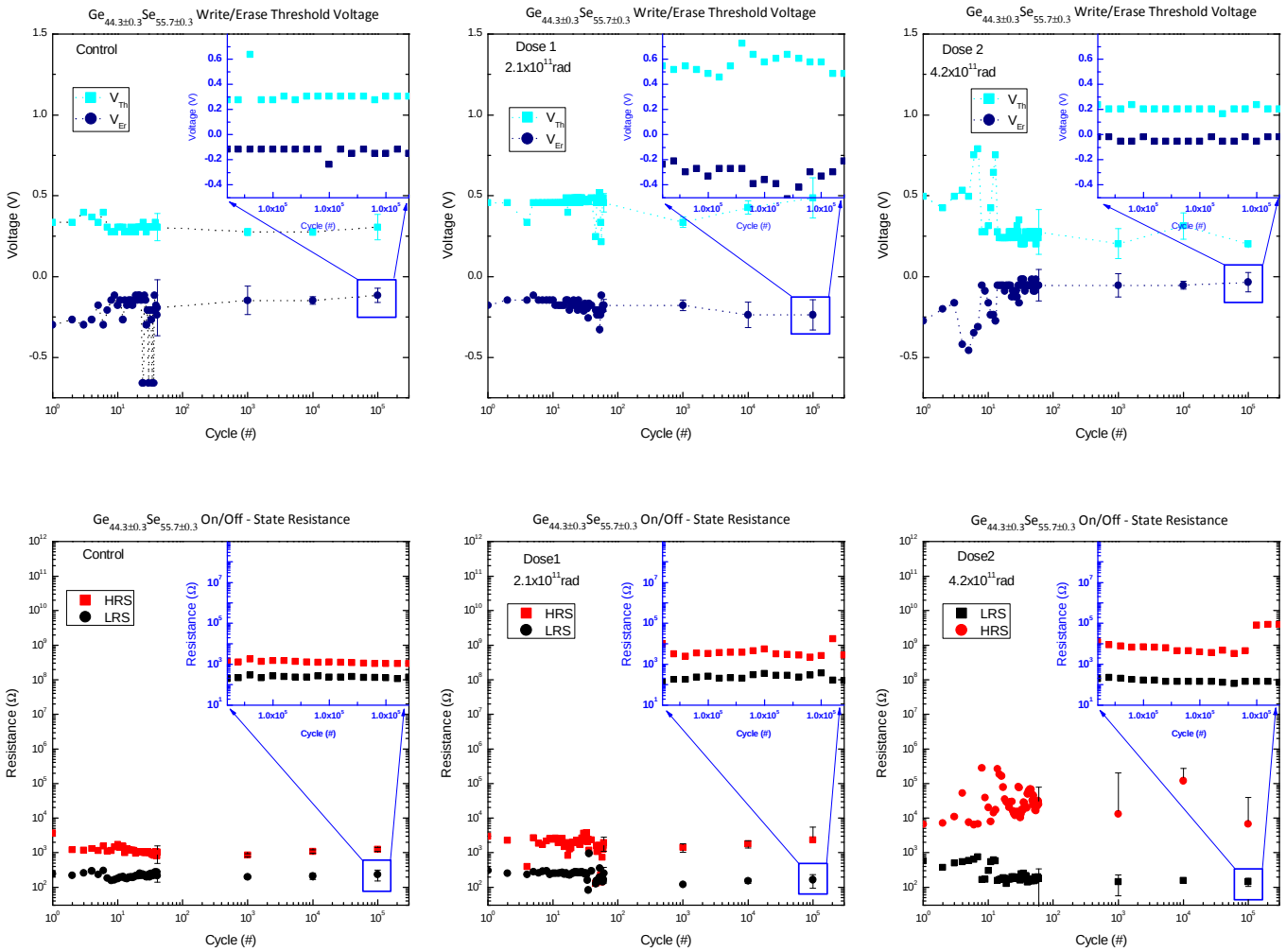

Figure 63. Endurance testing on $Ge_{36.2}Se_{63.8}$ RCBM devices exposed to 0 rad, $2.1x10^{11}$ rad, and $4.2x10^{11}$ rad of e-beam radiation

Discussion

The RCBM devices exposed to e-beam radiation show various reactions depending on the interplay of growth in the α-Ag_2Se phase, growth in the Ag_8GeSe_6 phase, and changes in the structural units. All of the Ag containing a-Ge_xSe_{100-x} films revealed growth in both the binary α-Ag_2Se and ternary Ag_8GeSe_6 phases when exposed to e-beam radiation.

However, the growth rate of the specific phases depends on the composition of the film as well as the exposure dose. It is important to note the preferential formation of the α-Ag_2Se, which is only stable at temperatures above 133 ^oC, instead of β-Ag_2Se, which is stable at room temperature. The formation of α-Ag_2Se in e-beam exposed films, regardless of the composition, is attributed to the presence of high and low pressure regions resulting from radiation (see Chapter 3, Electron Beam Radiation). The binary phase develops in these high pressure regions, which forces the compound to form in its closest packed structure, face-centered cubic (FCC), rather than the orthorhombic structure (β-Ag_2Se).

In the $Ge_{24.8}Se_{75.2}$ devices, the median HRS decreases by a small amount in the first dose. The small presence of the α-Ag_2Se phase, which is a superionic conductor, in the control device explains low resistance in the pre-irradiated device. Even at room temperature, the solid electrolyte α-Ag_2Se significantly increases the ionic conductivity of Ge-Se glasses [64, 90]. After the first dose of radiation, proportional growth in both the α-Ag_2Se and Ag_8GeSe_6 phases are observed in the XRD patterns. The superionic-conducting properties of the α-Ag_2Se dominate the HRS value of the device after this first dose. The XRD patterns show that additional radiation causes further growth in the

ternary phase; however, the binary phase is unchanged. Due to the further development in the ternary phase and lack thereof in the binary phase, the semiconducting properties of the ternary phase govern the resistance of the device, resulting in a large increase of the HRS.

The $Ge_{36.2}Se_{63.8}$ devices reveal a large decrease in the HRS after the first dose of radiation. This is attributed to the growth in both the α-Ag_2Se and Ag_8GeSe_6 phases as determined by the XRD patterns. After 10^5 switching cycles, this device shows serious degradation in the device performance and device failure soon thereafter. Further e-beam radiation results in agglomeration of α-Ag_2Se phase crystal to form larger crystals spaced farther apart. The phase agglomeration in addition to the spacing between these crystals results in a higher HRS and decreasing variation in HRS due to fewer conductive paths for electrons.

The HRS values of the $Ge_{44.3}Se_{55.7}$ devices demonstrate a large increase due to radiation exposure. Additionally, large changes in the structural units were also observed. Virtually no change was observed in the HRS after the first dose of radiation. There appears to be a threshold at the second dose where the growth rates of the binary and ternary phases decrease. Additionally, the emergence of a phase-separated Ag was observed from the XRD pattern. Furthermore, the ES/CS ratio increases dramatically. These observations are related to one another. The increase observed in the ES/CS ratio results in the formation of voids and the opening of the structural network. Consequently, incident electrons have a more direct path towards the previously diffused Ag. Interaction between incident electrons and Ag ionizes the Ag atoms, making them more mobile. Additionally, charging at the interface between the Ag electrode and the a-$Ge_{44.3}Se_{55.7}$

film creates an electric field. After $4.2x10^{11}$ rad of e-beam radiation, the electric field becomes strong enough to withdraw Ag ions from within the film. At the interface, Ag agglomeration occurs, proved by the XRD pattern. This effect has been studied and observed for chalcogenide glasses containing silver by Kawaguchi and Maruno [91]. The changes culminate in the significant increase of the HRS after Dose 2.

Conclusion

Interaction of electron beam radiation with Ge_xSe_{100-x} based RCBM devices and films were studied using Raman spectroscopy, XRD, and EDS mapping. It was discovered that $Ge_{24.8}Se_{76.2}$ based RCBM device performances were directly dependent on the formation of the α-Ag_2Se phase or lack thereof. The dependencies of the device performances on the crystal phase growth were further established by the $Ge_{36.2}Se_{63.8}$ devices. The $Ge_{44.3}Se_{55.7}$ devices were largely affected by the combination of dramatic structural changes and phase separation of Ag.

FINAL REMARKS AND FUTURE WORK

Final Remarks

As a result of this work, the following contributions have been made:

1. A detailed study of the influence of visible light on pure Ge-Se glasses was conducted. The outcomes of this study include the following:
    a. This study was the first to provide evidence that the effect of sub-bandgap light on glasses near the stoichiometric composition is predominantly related to the presence of lone-pair electrons. The excitation of these electrons leads to dynamic changes in the optical properties without affecting the structural properties of the film.
    b. For the interactions of sub-bandgap light with Ge-rich films, it was found that both the optical and structural properties of the films are affected.
2. Irradiation of films with x-rays produces effects similar to that of sub-bandgap light. The new findings of this study, which contribute to the knowledge of the influence of x-rays of Ge-Se films, include the following:

a. Films with compositions near that of the stoichiometric demonstrate a lack of structural changes due to the availability of lone-pair electrons and the abundance of stable heteropolar bonds.
b. Films deviating from the stoichiometric composition, either Ge-rich or Ge-deficient, undergo conversion of ES structures to CS structures, which relax the structure.
c. Ag diffusion readily occurs in the Se-rich films due to the relatively low packing fraction and the high affinity between Ag and Se. Comparatively, Ag diffusion is not evident in compositions near that of the stoichiometric.
d. Devices based on films that exhibited structural changes revealed an increased HRS after x-ray exposure.
e. Endurance of control and irradiated devices were commensurable. Therefore, it is concluded that these devices can operate successfully in an x-ray environment in the dose range studied in this work.

3. E-beam radiation on films and devices produced unique changes, which are related to the negative charge of the electrons and their small size.
    a. Only Ge-rich films exhibited structural changes under e-beam radiation.
    b. E-beam induced Ag diffusion products include α-Ag_2Se, resulting from charged sites, and Ag_8GeSe_6.

c. Devices based on Se-rich compositions demonstrated a push-pull relationship between the binary and ternary phases. The ratio of these species determined the device conductivity.
d. Devices based on films of the stoichiometric composition developed agglomerated crystals, which improved the endurance and reduced variations.
e. Drastic structural changes and interface charging reversed the benefits of Ag photodiffusion, increasing the variation in device performance.

Future Work

Further studies on RCBM devices are planned for both electron beam radiation and x-ray radiation. The influence of high energy electron beam (10 MeV) radiation on chalcogenide films and RCBM devices will be explored. Additionally, studies determining the influence of high energy x-rays (124 keV) on films and RCBM devices will be conducted. Moreover, progress on the present study will continue through investigating the influence of the low energy x-rays and electron beam at higher doses on RCBM devices in order to affirm the trends observed in this work.

REFERENCES

[1] F. H. Attix, *Introduction to radiological physics and radiation dosimetry*. New York: Wiley, 1986.

[2] D. A. Neamen, *Semiconductor physics and devices : basic principles*. Chicago: Irwin, 1997.

[3] S. T. Thornton and A. F. Rex, *Modern physics for scientists and engineers*: Cengage Learning, 2011.

[4] B. I. Kharisov, *Radiation synthesis of materials and compounds*. Boca Raton, Fla.: CRC, 2013.

[5] M. F. L'Annunziata, *Radioactivity : Introduction and History*. Amsterdam, the Netherlands; Boston [Mass.]; Oxford, UK: Elsevier, 2007.

[6] P. R. Willmott, *An introduction to synchrotron radiation : techniques and applications*. Chichester: Wiley, 2011.

[7] M. Iqbal, "Theory And Design Of Thermionic Electron Beam Guns," in *MODERN TRENDS IN PHYSICS RESEARCH: First International Conference on Modern Trends in Physics Research; MTPR-04*, 2005, pp. 376-386.

[8] Y. Sun, "Watching nanoparticle kinetics in liquid," *Materials Today*, vol. 15, pp. 140-147, 4// 2012.

[9] F. Krumeick, "Properties of electrons, their interactions with matter and applications in electron microscopy," *Laboratory of Inorganic Chemistry, disponível em http://www.microscopy.ethz.ch/downloads/Interactions.pdf, consultado em*, pp. 3-08, 2011.

[10] K. Rao, *Structural chemistry of glasses*: Elsevier, 2002.

[11] K. Tanaka and K. Shimakawa, *Amorphous chalcogenide semiconductors and related materials*: Springer, 2011.

[12] P. Chen, M. Mitkova, D. A. Tenne, K. Wolf, V. Georgieva, and L. Vergov, "Study of the Sorption Properties of $Ge_{20}Se_{80}$ Thin Films for NO_2 Gas Sensing," *Thin Solid Films*, vol. 525, pp. 141-147, 2012.

[13] V. Georgieva, M. Mitkova, P. Chen, D. Tenne, K. Wolf, and V. Gadjanova, "NO_2 gas sorption studies of $Ge_{33}Se_{67}$ films using quartz crystal microbalance," *Materials Chemistry and Physics*, vol. 137, pp. 552-557, 2012.

[14] J. Maimon, E. Spall, R. Quinn, and S. Schnur, "Chalcogenide-based non-volatile memory technology," in *Aerospace Conference, 2001, IEEE Proceedings.*, 2001, pp. 2289-2294.

[15] M. Tanaka, T. Minami, and M. Hattori, "Thermal Expansion and Its Related Properties of Arsenic-Sulfur Glasses," *Japanese Journal of Applied Physics*, vol. 5, pp. 185-186, 1966.

[16] X. Feng, W. J. Bresser, and P. Boolchand, "Direct Evidence for Stiffness Threshold in Chalcogenide Glasses," *Physical Review Letters,* vol. 78, pp. 4422-4425, 1997.
[17] R. Fairman and B. Ushkov, *Semiconducting chalcogenide glass*. Amsterdam; London: Elsevier Academic Press, 2004.
[18] K. Gupta and S. Das, "X-ray study of selenium in the liquid and colloidal state," *Indian J. Phys,* vol. 15, pp. 401-409, 1941.
[19] "CRC Handbook of Chemistry and Physics. 81st Edition," *JOURNAL-AMERICAN CHEMICAL SOCIETY,* vol. 122, p. 12614, 2000.
[20] A. V. Kolobov, P. Fons, and J. Tominaga, "p-Type conductivity of GeTe: The role of lone-pair electrons," *Phys. Status Solidi B,* vol. 249, pp. 1902-1906, 2012.
[21] J. R. Reitz, "Electronic Band Structure of Selenium and Tellurium," *Physical Review,* vol. 105, p. 1233, 1957.
[22] G. Yang, Y. Gueguen, J.-C. Sangleboeuf, T. Rouxel, C. Boussard-Plédel, J. Troles, *et al.*, "Physical properties of the Ge_xSe_{1-x} glasses in the $0< x< 0.42$ range in correlation with their structure," *Journal of Non-Crystalline Solids,* vol. 377, pp. 54-59, 2013.
[23] D. J. Sarrach, J. De Neufville, and W. Haworth, "Studies of amorphous Ge・Se・Te alloys (I): Preparation and calorimetric observations," *Journal of Non-Crystalline Solids,* vol. 22, pp. 245-267, 1976.
[24] L. Battezzati and A. Greer, "Thermodynamics of $Te_{80}Ge_{20-x}Pb_x$ glass-forming alloys," *Journal of Materials Research,* vol. 3, pp. 570-575, 1988.
[25] Y. Sakaguchi, D. Tenne, and M. Mitkova, "Structural development in Ge-rich Ge–S glasses," *Journal of Non-Crystalline Solids,* vol. 355, pp. 1792-1796, 2009.
[26] T. Kohoutek, T. Wagner, J. Orava, M. Krbal, J. Ilavsky, M. Vlcek, *et al.*, "Multilayer planar structures prepared from chalcogenide thin films of As–Se and Ge–Se systems and polymer thin films using thermal evaporation and spin-coating techniques," *Journal of Non-Crystalline Solids,* vol. 354, pp. 529-532, 1/15/ 2008.
[27] A. Zakery and S. Elliott, "Optical properties and applications of chalcogenide glasses: a review," *Journal of Non-Crystalline Solids,* vol. 330, pp. 1-12, 2003.
[28] A. Zakery and S. R. Elliott, *Optical nonlinearities in chalcogenide glasses and their applications* vol. 135: Springer, 2007.
[29] M. N. Kozicki and M. Mitkova, "Memory devices based on mass transport in solid electrolytes," *Nanotechnology,* 2010.
[30] K. Asatryan, S. Frédérick, T. Galstian, and R. Vallée, "Recording of polarization holograms in photodarkened amorphous chalcogenide films," *Applied physics letters,* vol. 84, pp. 1626-1628, 2004.
[31] M. Trunov, P. Lytvyn, S. Yannopoulos, I. Szabo, and S. Kökényesi, "Photoinduced mass-transport based holographic recording of surface relief gratings in amorphous selenium films," *Applied Physics Letters,* vol. 99, p. 051906, 2011.
[32] P. Krecmer, A. Moulin, R. Stephenson, T. Rayment, M. Welland, and S. Elliott, "Reversible nanocontraction and dilatation in a solid induced by polarized light," *Science,* vol. 277, pp. 1799-1802, 1997.

[33] A. Ganjoo, N. Yoshida, and K. Shimakawa, "Recent Research Developments in Applied Physics, ed," *M. Kawasaki, N. Ashgritz, R. Anthony (Research Signpost, Trivandrum 2, 129,* 1999.

[34] Q. Yan, H. Jain, G. Yang, J. Ren, and G. Chen, "Millisecond kinetics of photo-darkening/bleaching in xGe45Se55-(1− x) As45Se55 chalcogenide amorphous films," *Journal of Applied Physics,* vol. 112, p. 053105, 2012.

[35] D. Arsova and E. Vateva, "Dual action of light in photodarkened Ge‐As–S films," *Phys. Status Solidi B,* vol. 249, pp. 153-157, 2012.

[36] P. Khan, A. Barik, E. Vinod, K. Sangunni, H. Jain, and K. Adarsh, "Coexistence of fast photodarkening and slow photobleaching in $Ge_{19}As_{21}Se_{60}$ thin films," *Optics express,* vol. 20, pp. 12416-12421, 2012.

[37] Q. Yan, H. Jain, J. Ren, D. Zhao, and G. Chen, "Effect of photo-oxidation on photobleaching of $GeSe_2$ and Ge_2Se_3 films," *The Journal of Physical Chemistry C,* vol. 115, pp. 21390-21395, 2011.

[38] V. Lyubin, M. Klebanov, A. Bruner, N. Shitrit, and B. Sfez, "Transient photodarkening and photobleaching in glassy GeSe2 films," *Optical Materials,* vol. 33, pp. 949-952, 4// 2011.

[39] F. Yakuphanoglu, D. Arsova, and E. Vateva, "Photoinduced changes of the optical parameters of thin films from Ge30. 8As5. 7S63. 5 glass," *Journal of optoelectronics and adavnced materials,* vol. 9, pp. 334-336, 2007.

[40] V. Kornelyuk, I. Savitskii, L. Khirunenko, O. Shpotyuk, and I. Yaskovets, "Photoinduced defect formation in chalcogenide vitreous semiconductors," *Journal of Applied Spectroscopy,* vol. 50, pp. 310-313, 1989.

[41] K. Shimakawa, A. Kolobov, and S. Elliott, "Photoinduced effects and metastability in amorphous semiconductors and insulators," *Adv. in Phys.,* vol. 44, pp. 475-588, 1995.

[42] N. Terakado and K. Tanaka, "Photoinduced Phenomena in GeO_2-GeS_2 Glasses," *Japanese Journal of Applied Physics,* vol. 46, p. L265, 2007.

[43] S. Rajagopalan, K. S. Harshavardhan, L. K. Malhotra, and K. L. Chopra, "Photo-optical changes in Ge-chalcogenide films," *Journal of Non-Crystalline Solids* vol. 50, pp. 29-38, 1982.

[44] Y. Utsugi and Y. Mizushima, "Photostructural change in the Urbach tail in chalcogenide glasses," *Journal of Applied Physics,* vol. 51, pp. 1773-1779, 1980.

[45] K. Tanaka, Y. Kasanuki, and A. Odajima, "Physical properties and photoinduced changes of amorphous Ge-S films," *Thin Solid Films,* vol. 117, pp. 251-260, 1984.

[46] K. Shimakawa, K. Fukami, H. Kishi, G. Belev, and S. Kasap, "X-ray induced effects on photocurrents in amorphous Se films," *Japanese journal of applied physics,* vol. 46, p. L192, 2007.

[47] O. I. Shpotyuk, "Radiation-induced effects in chalcogenide vitreous semiconductors," *Semiconductors and Semimetals,* vol. 78, pp. 215-260, 2004.

[48] A. Khursheed. (2011). *Scanning electron microscope optics and spectrometers*. Available: http://public.eblib.com/EBLPublic/PublicView.do?ptiID=731284

[49] K. Tanaka, "Electron beam induced reliefs in chalcogenide glasses," *Applied physics letters,* vol. 70, pp. 261-263, 1997.

[50] J. Romero, A. Fitzgerald, and K. Mietzsch, "Electron irradiation induced expansion in amorphous chalcogenide films," *Journal of applied physics,* vol. 91, pp. 9572-9574, 2002.
[51] R. Debnath and A. Fitzgerald, "Electron beam induced surface modification of amorphous Sb_2S_3 chalcogenide films," *Applied surface science,* vol. 243, pp. 148-150, 2005.
[52] M. N. Kozicki, M. Park, and M. Mitkova, "Nanoscale memory elements based on solid-state electrolytes," *Nanotechnology, IEEE Transactions on,* vol. 4, pp. 331-338, 2005.
[53] M. Mitkova, T. Petkova, P. Markovski, and V. Mateev, "Photoinduced changes by polarisation holographic recording in $Se_{70}Ag_{15}I_{15}$ thin films," *Journal of non-crystalline solids,* vol. 164, pp. 1203-1206, 1993.
[54] M. Mitkova, I. Iliev, V. Boev, and T. Petkova, "Influence of an electrical field on optical recording in chalco-halide glasses," *Journal of non-crystalline solids,* vol. 227, pp. 748-751, 1998.
[55] M. Mitkova, T. Petkova, P. Markovski, and V. Mateev, "Photoinduced changes in the selenium-silver-iodine system," *The Journal of Physical Chemistry,* vol. 96, pp. 8998-9001, 1992.
[56] A. Husmann, J. Betts, G. Boebinger, A. Migliori, T. Rosenbaum, and M.-L. Saboungi, "Megagauss sensors," *Nature,* vol. 417, pp. 421-424, 2002.
[57] M. Schöning, C. Schmidt, J. Schubert, W. Zander, S. Mesters, P. Kordos, *et al.*, "Thin film sensors on the basis of chalcogenide glass materials prepared by pulsed laser deposition technique," *Sensors and Actuators B: Chemical,* vol. 68, pp. 254-259, 2000.
[58] M. Frumar and T. Wagner, "Ag doped chalcogenide glasses and their applications," *Current Opinion in Solid State and Materials Science,* vol. 7, pp. 117-126, 2003.
[59] D. Tsiulyanu and I. Stratan, "On the photodissolution kinetics of silver in glassy As2S3," *Journal of Non-Crystalline Solids,* vol. 356, pp. 147-152, 2/1/ 2010.
[60] D. Goldschmidt, T. Bernstein, and P. Rudman, "The kinetics of photodissolution of silver in amorphous As_2S_3 Films," *physica status solidi (a),* vol. 41, pp. 283-287, 1977.
[61] A. Kolobov, V. Lyubin, and J. Tröltzsch, "On the mechanism of anomalous surface diffusion of silver in an amorphous chalcogenide/silver structure," *physica status solidi (a),* vol. 115, pp. K139-K141, 1989.
[62] T. Wagner, "Photo-and thermally-induced diffusion and dissolution of Ag in chalcogenide glasses thin films," *Journal of Optoelectronics and Advanced Materials,* vol. 4, pp. 717-727, 2002.
[63] M. Mitkova, M. Kozicki, H. Kim, and T. Alford, "Local structure resulting from photo and thermal diffusion of Ag in Ge–Se thin films," *Journal of Non-Crystalline Solids,* vol. 338, pp. 552-556, 2004.
[64] K. Shahi, "Transport studies on superionic conductors," *physica status solidi (a),* vol. 41, pp. 11-44, 1977.
[65] L. Geppert, "The new indelible memories," *Spectrum, IEEE,* vol. 40, pp. 48-54, 2003.

[66] S. S. Eaton, D. B. Butler, M. Parris, D. Wilson, and H. McNeillie, "A Ferroelectric Nonvolatile Memory," in *Solid-State Circuits Conference, 1988. Digest of Technical Papers. ISSCC. 1988 IEEE International*, 1988, p. 130.

[67] Y. Hosoi, Y. Tamai, T. Ohnishi, K. Ishihara, T. Shibuya, Y. Inoue, *et al.*, "High speed unipolar switching resistance RAM (RRAM) technology," in *Electron Devices Meeting, 2006. IEDM'06. International*, 2006, pp. 1-4.

[68] R. Waser, R. Dittmann, G. Staikov, and K. Szot, "Redox-Based Resistive Switching Memories–Nanoionic Mechanisms, Prospects, and Challenges," *Advanced Materials*, vol. 21, pp. 2632-2663, 2009.

[69] T. Tsuruoka, K. Terabe, T. Hasegawa, and M. Aono, "Forming and switching mechanisms of a cation-migration-based oxide resistive memory," *Nanotechnology*, vol. 21, p. 425205, 2010.

[70] M. N. Kozicki and M. Mitkova, "Mass transport in chalcogenide electrolyte films–materials and applications," *Journal of non-crystalline solids*, vol. 352, pp. 567-577, 2006.

[71] K. Jackson, A. Briley, S. Grossman, D. V. Porezag, and M. R. Pederson, "Raman-active modes of a-$GeSe_2$ and a-GeS_2: A first-principles study," *Physical Review B*, vol. 60, p. R14985, 1999.

[72] J. A. Aronovitz, J. R. Banavar, M. A. Marcus, and J. C. Phillips, "Structural models and vibrational spectra of tetrahedral chalcogenide crystals and glasses," *Physical Review B*, vol. 28, pp. 4454-4460, 10/15/ 1983.

[73] S. Sugai, "Stochastic random network model in Ge and Si chalcogenide glasses," *Physical Review B*, vol. 35, pp. 1345-1361, 1987.

[74] K. Inoue, O. Matsuda, and K. Murase, "A model calculation of the characteristic Raman modes in the tetrahedral network structures of $GeSe_2$," *Physica B: Condensed Matter*, vol. 219-220, pp. 520-522, 1996.

[75] K. Jackson, "Electric Fields in Electronic Structure Calculations: Electric Polarizabilities and IR and Raman Spectra from First Principles," *physica status solidi (b)*, vol. 217, pp. 293-310, 2000.

[76] T. G. Edwards and S. Sen, "Structure and Relaxation in Germanium Selenide Glasses and Supercooled Liquids: A Raman Spectroscopic Study," *The Journal of Physical Chemistry B*, vol. 115, pp. 4307-4314, 2011.

[77] G. Lucovsky, C. K. Wong, and W. B. Pollard, "Vibrational properties of glasses: Intermediate range order," *Journal of Non-Crystalline Solids* vol. 59-60, pp. 839-846, 1983.

[78] G. Lucovsky and F. L. Galeener, "Intermediate range order in amorphous solids," *Journal of Non-Crystalline Solids* vol. 35-36, pp. 1209-1214, 1980/2// 1980.

[79] R. R. Kumar, A. Barik, E. Vinod, M. Bapna, K. Sangunni, and K. Adarsh, "Crossover from photodarkening to photobleaching in a-Ge_xSe_{100-x} thin films," *Optics Letters*, vol. 38, pp. 1682-1684, 2013.

[80] K. Jackson, A. Briley, S. Grossman, D. Porezag, and M. Pederson, "Raman-active modes of a-$GeSe_2$ and a-GeS_2: A first-principles study," *Phys. Rev. B Physical Review B*, vol. 60, pp. R14985-R14989, 1999.

[81] J. Berashevich, A. Mishchenko, and A. Reznik, "The two-step photoexcitation mechanism in a-Se," *arXiv preprint arXiv:1402.6164*, 2014.

[82] J. C. Mauro and A. K. Varshneya, "Multiscale modeling of GeSe2 glass structure," *Journal of the American Ceramic Society,* vol. 89, pp. 2323-2326, 2006.
[83] K. Tanaka, "Mechanisms of photodarkening in amorphous chalcogenides," *Journal of Non-Crystalline Solids,* vol. 59, pp. 925-928, 1983.
[84] A. Reznik, S. Baranovskii, M. Klebanov, V. Lyubin, O. Rubel, and J. Rowlands, "Reversible vs irreversible photodarkening in a-Se: the kinetics study," *Journal of Materials Science: Materials in Electronics,* vol. 20, pp. 111-115, 2009.
[85] M. Mitkova, M. Kozicki, H. Kim, and T. Alford, "Crystallization effects in annealed thin Ge–Se films photodiffused with Ag," *Journal of non-crystalline solids,* vol. 352, pp. 1986-1990, 2006.
[86] T. Edwards and S. Sen, "Structure and relaxation in germanium selenide glasses and supercooled liquids: a Raman spectroscopic study," *The Journal of Physical Chemistry B,* vol. 115, pp. 4307-4314, 2011.
[87] P. M. Bridenbaugh, G. P. Espinosa, J. E. Griffiths, J. C. Phillips, and J. P. Remeika, "Microscopic origin of the companion A_1 Raman line in glassy $Ge(S,Se)_2$," *Physical Review B,* vol. 20, pp. 4140-4144, 1979.
[88] P. Boolchand, J. Grothaus, M. Tenhover, M. Hazle, and R. K. Grasselli, "Structure of GeS_2 glass: Spectroscopic evidence for broken chemical order," *Physical Review B,* vol. 33, p. 5421, 1986.
[89] P. Scherrer, "Göttinger Nachrichten Math," *Phys,* vol. 2, pp. 98-100, 1918.
[90] C. Angell, "Mobile ions in amorphous solids," *Annual Review of Physical Chemistry,* vol. 43, pp. 693-717, 1992.
[91] T. Kawaguchi and S. Maruno, "Photoinduced surface deposition of metallic silver in Ag-As-S glasses," *J. of Appl. Phys.,* vol. 77, pp. 628-634, 1995.